

Doctoral Dissertation

Julius-Maximilians-
**UNIVERSITÄT
WÜRZBURG**

Institut für Theoretische Physik und Astrophysik

Evolution of shocks and turbulence in major galaxy-cluster mergers

Dissertation zur Erlangung des
naturwissenschaftlichen Doktorgrades
der Julius-Maximilians-Universität Würzburg



Surajit Paul

aus **Bankura, India**

Institut für Theoretische Physik und Astrophysik
Fakultät für Physik und Astronomie
Universität Würzburg

Würzburg, Germany
November, 2009

Eingereicht am: 25.11.2009

bei der

Fakultät für Physik und Astronomie

Gutachter und Prüfer im Promotionsverfahren:

1. Gutachter Prof. Dr. Karl Mannheim
 2. Gutachter apl. Prof. Dr. Thomas Trefzger
- der Dissertation

1. Prüfer Prof. Dr. Karl Mannheim
 2. Prüfer Prof. Dr. Thomas Trefzger
 3. Prüfer Prof. Dr. Thorsten Ohl
- im Promotionskolloquium
-

Tag des Promotionskolloquiums: 29.03.2010

Doktururkunde ausgehändigt am:

Evolution of shocks and turbulence in major galaxy-cluster mergers

This thesis is mainly based upon the following publications:

S. Paul, L. Iapichino, F. Miniati, J. Bagchi and K. Mannheim : Evolution of shocks and turbulence in major cluster mergers. (Paper submitted to Astrophysical Journal (ApJ))

S. Paul, J. Bagchi, L. Iapichino, T. Ensslin, and K. Mannheim : Probing turbulence re-acceleration at the arcs of Abell 3376. (Paper in preparation)

Joydeep Bagchi, Florence Durret, Gastao B. Lima Neto, Surajit Paul : Giant Ringlike Radio Structures Around Galaxy Cluster Abell 3376. **2006, Science, Vol. 314, pp. 791 - 794.**

Iapichino, L., Niemeyer, J., Paul, S., Schmidt, W. Turbulence Modeling and the Physics of the Intra-Cluster Medium. (Accepted for publication in Proceedings of the workshop "High Performance Computing in Science and Engineering", Springer-verlag.)

Iapichino, L., Niemeyer, J.C., Adamek, J., Paul, S., Scuderi, M.: Modeling of Turbulent Flows Applied to Numerical Simulations of Galaxy Clusters. 2007, Proceedings of the workshop "High Performance Computing in Science and Engineering", Springer-verlag.

Joydeep Bagchi, Florence Durret, Gastao B. Lima Neto, Surajit Paul, Satyajit Chavan: High and ultra-high energy cosmic ray acceleration in structure-formation shocks in Abell 3376 galaxy cluster. 2005, ICRC (International Cosmic Ray Conference) proceedings.

Joydeep Bagchi, Florence Durret, Gastao B. Lima Neto and Surajit Paul : The disturbed X-ray cluster Abell 3376 and its giant ring-like radio structures. (Accepted for the conference "The X-ray Universe 2008" May 2008, Granada, Spain)

S. Paul, L. Iapichino, F. Miniati, J. Bagchi and K. Mannheim : Evolution of shocks and turbulence in major cluster mergers. (Paper in final stage of submission to Astrophysical Journal (ApJ))

The thesis work presented here is a part of the research done within the DFG-funded International Research Training Group (GRK 1147/1) entitled as Theoretical Astrophysics and Particle Physics. This graduate school is a joint project of the Department of Physics (Theoretical Astrophysics and Theoretical High Energy Physics) and the Department of Mathematics of the Julius-Maximilians-Universität Würzburg; it is funded by the Deutsche Forschungsgemeinschaft (DFG) and so was the author.



PhD thesis
Author: Surajit Paul
email: spaul@astro.uni-wuerzburg.de or surajit@iucaa.ernet.in

.

Kurze Zusammenfassung

Die Verschmelzung reicher Galaxienhaufen ist das energiereichste Ereignis im Universum. Während des Verschmelzungsvorgangs wird eine komplexe Kette von Prozessen ausgelöst, durch die die Stoßenergie der Galaxienhaufen freigesetzt wird. In dieser Phase der heftigen Relaxation entwickeln sich Turbulenz und Stoßwellen sowie nicht-thermische Teilchenpopulationen. In der vorliegenden Dissertation wird der Versuch unternommen, Multiwellenlängenbeobachtungen des kollidierenden Galaxienhaufens Abell 3376 im Rahmen eines theoretischen Modells der involvierten Effekte zu interpretieren. Es wurden Beobachtungen mit dem Very Large Array Radiointerferometer durchgeführt und analysiert, um die Morphologie der nichtthermischen Teilchenverteilung in Abell 3376 insbesondere im Bereich der Stoßwellen aufzuklären. Die Dissipation im heißen Intracluster-Gas wurde anhand von archivierten Röntgenbeobachtungen von ROSAT und XMM untersucht. Die Ergebnisse wurden mit eingeschränkten numerischen Simulationen der Entwicklung des Verschmelzungsprozesses im Rahmen der kosmologischen Strukturbildung verglichen. Dabei wurde das ENZO-Programm verwendet, das die gasdynamischen Eigenschaften sowie die Eigengravitation der kollidierenden Massenverteilung berechnet. Aussagen über die nicht-thermischen Eigenschaften des Intracluster-Gases konnten aus der lokalen Machzahl sowie der Turbulenzstärke indirekt abgeleitet werden.

Brief summary

Mergers between rich clusters of galaxies represent the most violent events in the Universe. The merger events initiate a complex chain of processes that leads to the dissipation of the collisional energy. This phase of violent relaxation is accompanied by turbulence and shock waves as well as nonthermal particle acceleration. This thesis aims at the interpretation of multi-wavelength observations of the merging cluster of galaxies Abell 3376 in the framework of a theoretical model of the involved effects. Observations with the Very Large Array radio interferometer were carried out and analyzed to clarify the morphology of the nonthermal particle distribution in Abell 3376, in particular about the shocked regions. The dissipation in the hot intracluster gas was studied using archival X-ray observations with ROSAT and XMM. Results were compared with constrained numerical simulations of the evolution of the merger process in the framework of cosmological structure formation. For this purpose, the ENZO-Code was employed for the computation of the gas dynamics and self-gravity of the colliding mass distribution. The nonthermal properties of the intracluster gas could be indirectly inferred from the local Mach number and the strength of the turbulence.

*This thesis is dedicated to my family
and
my teacher Late Dharani Dhar Bhattacharya*

Contents

1. Introduction & Motivation	2
1.1. Introduction & Motivation	2
1.2. Structure	5
2. Evolution of clusters of galaxies and major merger shocks	6
2.1. Clusters of galaxies	6
2.2. Clusters through structure formation	7
2.2.1. Role of Dark-matter in Structure formation	7
2.2.2. Pattern of structure and cluster formation	9
2.3. Theory of cluster merger and shock evolution	10
2.3.1. Cluster Merger Rates	10
2.3.1.1. Accretion, merger and major merger classification	11
2.3.2. Energy release in mergers	11
2.3.3. Effects of cluster mergers	12
2.3.3.1. Change in gas dynamics and kinematics	12
2.3.3.2. Generation of megapersec-scale shocks	15
2.3.3.3. Injection of turbulence into the ICM and amplification of magnetic field	16
2.3.3.4. Acceleration of particles by shock and turbulence	17
3. Current status of research and the objectives of the thesis project	20
3.1. Current status of the research in this field of shock evolution and its effects	20
3.1.1. Status of research on merger shock evolution	20
3.2. Objectives of the thesis work	21
3.2.1. Milestones	21
4. Observation basics and details of data analysis	24
4.1. Radio observations and data analysis	24
4.1.1. Radio astronomy basics	24
4.1.2. Radio interferometry	27
4.1.3. Technical details and specification of the Very Large Array (VLA)	28
4.1.3.1. Information about VLA	30
4.1.3.2. Technical details of VLA	31
4.1.4. VLA data analysis	36

4.2.	X-ray astronomy basics and data analysis	37
4.2.1.	Space-borne observations in X-ray astronomy	37
4.2.1.1.	Satellite-borne X-ray observatories:	37
4.2.2.	Technical details and other specifications of ROSAT	38
4.2.2.1.	Overview	38
4.2.2.2.	Instrumentation	38
4.2.2.3.	DATA analysis	39
4.2.3.	Technical details and other specifications of XMM	39
4.2.3.1.	Overview	40
4.2.3.2.	Instrumentation	40
4.2.3.3.	Data analysis	41
5.	Observations of the evolution of shocks in a major cluster merger	42
5.1.	Significance of the observations of Abell 3376	42
5.2.	Results	44
5.2.1.	Radio observations and data analysis	44
5.2.1.1.	Shock structure mapped in the 20cm and 6cm radio bands using the VLA	45
5.2.1.2.	Spectral index of the radio structures	47
5.2.1.3.	Estimation of magnetic field	48
5.2.2.	X-ray observation and data analysis	49
5.2.2.1.	ROSAT X-ray image of Abell 3376 in 0.14 to 2.0 keV X-ray band	51
5.2.2.2.	XMM X-ray image in 0.3 to 8.0 keV X-ray band	51
5.3.	Interpretation of the results	52
5.3.1.	Merger shock	53
6.	Hydrodynamical simulation	56
6.1.	Dark matter and gas dynamics	56
6.1.1.	N-body dynamics	56
6.1.2.	Gas dynamics or hydrodynamics	57
6.1.2.1.	The Euler equations	57
6.1.2.2.	Turbulence in hydrodynamic equation	58
6.1.2.3.	Shock waves	59
6.2.	Numerical implementation of N-body and gas dynamics in ENZO	59
6.2.1.	Solution for N-body dynamics	59
6.2.2.	Solution for gas dynamics	60
6.3.	Adaptive mesh refinement (AMR) in ENZO	61
7.	Simulation of the evolution of shocks and turbulence in a major cluster merger	64
7.1.	Objectives and setting up the simulation	64

7.1.1. Initial conditions	64
7.1.2. Simulation setup	65
7.1.3. Selection of refinement criteria	65
7.1.3.1. Comparison of the AMR criteria	67
7.2. Resolution study	68
7.3. Results	71
7.3.1. Different aspects of simulated clusters:	71
7.3.2. Active and relaxed clusters	73
7.3.2.1. Long lasting central turbulence	76
7.3.3. Scaling relation	76
7.3.4. Merging cluster	77
7.3.5. Emergence of shock waves and their evolution through the ICM: . .	79
7.3.6. Mach number of the shock	81
7.3.7. Structure function:	81
7.3.8. Generation and evolution of turbulence in the post shock ICM . . .	83
7.3.9. Extension of turbulent medium:	87
8. Summary & Discussion	88
8.1. Discussion of the main findings	88
8.1.1. Nature of shocks in Abell 3376	88
8.1.2. Morphological similarity	89
8.1.2.1. Extension of the shock and Fermi-II acceleration	90
Bibliography	92

Contents

.

List of Figures

1.1.	<i>A composite map of the radio and X-ray emission from the cluster Abell 3376. The VLA observed 1.4 GHz total intensity contours (yellow) are: 0.12, 0.24, 0.48 and 1 mJy/beam. (Beam: 20" FWHM). The large ellipse shows an elliptical fit to the peripheral giant radio structure. The central colour image depicts the thermal bremsstrahlung X-ray emission observed with the ROSAT PSPC instrument (~ 12 kilo seconds exposure, 0.14-2.0 keV band). The red circles mark the positions of two brightest clusters. The shock structures found at 1.4 GHz radio frequency show a downstream extension of ~ 500 kpc and their length is more than a Gigaparsec. Image is taken from Bagchi et al. (2006). Reprinted with permission from AAAS</i>	3
2.1.	<i>Projected density map of a filamentary structure in a 25.6^3 Mpc³ co-moving volume. It shows how the clusters are embedded in a weblike filamentary structure. Mass is first channeled through those filaments and all the structures and sub-structures are dragged along the filaments and finally the nearest clumps are merged to form a bigger cluster. (Image source: S. Paul Galaxy merger project(2008))</i>	8
2.2.	Panel (a) and (a1): Radial dark matter and gas density variation in a relaxed cluster at different redshifts. The gas density clearly follows the dark matter profile; Panel (b) and (b1): Radial variation of dark matter and gas density profile respectively in an active cluster of galaxies. Disturbed dark matter profile at different redshifts can be seen, the gas profile becomes flattened.	13
4.1.	<i>Line diagram of a radio interferometry system.</i>	27
4.2.	<i>Antennas on u-v plane.</i>	29
4.3.	<i>System Temperature Variations with Elevation at L, K, and Q Bands. The data have been normalized by the system temperature at the zenith - approximately 80K at 43 GHz, 170K at 23 GHz, and 35K at 1365 MHz. The observations were taken in good weather conditions.</i>	35
4.4.	<i>Working method of AIPS in a diagram</i>	36
5.1.	Panel 1: NVSS radio image of Abell 3376; Panel 2: ROSAT X-ray image of Abell 3376	42

5.2.	<i>Several pointings of VLA observation. Original image is taken from Bagchi et al. (2006). Reprinted with permission from AAAS.</i>	46
5.3.	<i>Mosaic VLA image of Abell 3376 at 20cm</i>	47
5.4.	<i>Mosaic VLA image of Abell 3376 in 6 cm</i>	48
5.5.	<i>Spectral index vs Mach number</i>	49
5.6.	<i>Spectral index of East and West radio arc of Abell 3376. 20cm and 6cm VLA data are combined to produce this spectral index map</i>	50
5.7.	<i>ROSAT X-ray image of Abell 3376</i>	52
5.8.	Panel1: <i>XMM X-ray image of Abell 3376; Panel2:</i> <i>Temperature map of Abell3376 derived from XMM X-ray data</i>	53
6.1.	<i>Adaptive Mesh Refinement (AMR) schemes in ENZO N-body simulation</i>	61
7.1.	Panel (a): <i>is simulated only with the ‘over-density’ criteria to refine the grids; Panel (b):</i> <i>is a simulation with the refinement criteria based on vorticity along with ‘over-density’; Panel (c):</i> <i>is a simulation with the refinement criteria based on compression ratio along with ‘over-density’</i>	67
7.2.	<i>Three rows in the figure are containing three panels; each represents the three time compensated slices of temperature map in Run 1, Run 2 and Run 3 with superimposed density contours respectively. The box size is about 10 Mpc h⁻¹ in each side</i>	69
7.3.	<i>Level of refinement (AMR) is plotted for 96 Grid 64 Grid and 48 Grid on consecutive panels. Delay of shock emergence has been compensated, 96 Grid is at z=0.2, 64 Grid is at z=0.15 and 48 Grid is at z=0.00. Though in every cases the level of highest possible AMR has reached but 48 Grid is clearly seen under resolved and the shock fronts thus cannot be separately seen or resolved. The morphology of 96 Grid and 64 Grid are quite similar. [colour coding: Blue = level (ℓ) 2, sky = ℓ 3, green = ℓ 4, yellow = ℓ 5 and red = ℓ 6]</i>	70
7.4.	<i>Upper 3 panel shows level of refinement of 64 Grid and the lower three panels is of 96 Grid. Delay of shock emergence has been compensated. Structure seen in both the cases are much similar and level of resolution is at same order. [colour coding is same as Fig. 7.3]</i>	70
7.5.	<i>Average RMS velocity of the post shock region is calculated using the method described in section 7.3.8 for each 96³, 64³ and 48³, respectively, and plotted together in this plot. It shows convergence for 96³ and 64³ in the later stages, although 48³ is an under resolved case.</i>	71
7.6.	Panel (a) and (a1): <i>Radial dark matter and gas density variation in a relaxed cluster at different redshifts. The gas density clearly follows the dark matter profile; Panel (b) and (b1):</i> <i>Radial variation of dark matter and gas density profile, respectively, in an active cluster of galaxies.</i>	74

7.7. Panel (a): Radial evolution of mass and rms velocity of both the relaxed (black lines) and active (coloured lines) clusters are plotted; Panel (b): Radial evolution of temperature and rms velocity are plotted with same colour code as earlier; Panel (c): Plot shows the time evolution of turbulence of relaxed (solid black line) and active clusters (dotted black line); Panel (d): The last panel shows the fractional turbulent pressure in the respective clusters with the same colour code as the above.	75
7.8. panel 1: Scaling relation between merged mass and turbulence energy at the centre of the cluster; panel 2: Scaling relation between final mass and the turbulence energy behind the shock	77
7.9. shows the merger scenario in coloured density map of the event number VI (i.e. C-VI) in the table 7.3.1. We tracked the merger event in density maps of 7.7×7.7 Mpc slices cut on the y-z plane of the simulation volume along the centre of mass of the cluster. The panel of figures show the pre and post merger morphology in density of the cluster starting from redshift 0.4 to the present epoch i.e. to redshift 0. The redshift of the each panel is indicated below the panel as $z = \#$. The contoured density map is superimposed over the coloured map. The 5 density contours are 4.5×10^8 , 4.5×10^9 , 4.5×10^{10} , 4.5×10^{11} and 4.5×10^{12} respectively. Two filamentary nodes i.e. clusters with masses $7.23 \times 10^{13} M_{\odot} h^{-1}$ and $4.23 \times 10^{13} M_{\odot} h^{-1}$ got merged at redshift 0.3.	78
7.10. shows the merger scenario in coloured temperature and contoured density map of the event number 6 in the Table 7.3.1. The panel of 9 figures show the temperature evolution of the cluster. The panels are cut in to slices of 7.7×7.7 Mpc on the y-z plane of the simulation volume along the centre of mass of the cluster. The figures show the pre and post merger temperature distribution in the ICM. Temperature is varying from 1 K (Blue) to $\geq 2.5 \times 10^7$ K (Red). The colour code in between are of values 6.25×10^6 K (sky blue), 1.25×10^7 K (green) and 1.875×10^7 K (yellow) respectively. There are 5 density contours with values 4.5×10^8 , 4.5×10^9 , 4.5×10^{10} , 4.5×10^{11} and 4.5×10^{12} respectively. The temperature evolution shows, after merging, how the two bow like shock fronts generate and takes up a hemispherical structure in its time of evolution through cosmic wave structures. Though the jump in density is considerable, a huge temperature jump can easily be seen (compare panel number 1,2,3 (before merging) and number 5 onwards (after emergence of shocks)).	80
7.11. Mach number distribution over the examined cluster is shown on the figure. Contours levels are 1,2,3,4 and 5 respectively. Average Mach number behind the shock is 2-3.	82
7.12. Longitudinal and transverse structure function at different redshifts as mentioned in the figures. The dotted line shows the theoretical Kolmogorov type velocity structure.	83

- 7.13. *shows the merger scenario in coloured normalized vorticity map of the event number 5 in the table 7.3.1. The contoured density map is superimposed over the coloured map. Five density contours are 4.5×10^8 , 4.5×10^9 , 4.5×10^{10} , 4.5×10^{11} and 4.5×10^{12} respectively. We tracked the merger event in vorticity maps of 7.7×7.7 Mpc slices cut on the y-z plane of the simulation volume along the centre of mass of the cluster. The panel of figures show the pre and post merger morphology in vorticity of the cluster starting from redshift 0.4 to present day at redshift 0. The redshift of the each panel is indicated below the panel as $z = \#$. We see how the level of turbulence (as astrophysical turbulence is defined as vorticity $\omega = \nabla \times v$)* 84
- 7.14. **Panel 1:** *shows a plot of rms velocity of the downstream region (post shock ICM). On the x axis we plotted the lookback time in Giga years from the time when the shock started emerging. The y axis shows the average rms velocity evaluated for different analysis spheres placed behind the shock. Error bars are the standard error of the results from the analysis at each redshift.* **Panel 2:** *shows a plot of ratio of turbulent to total (total of thermal and turbulent) pressure of the downstream region (post shock ICM). On the x axis, the lookback time in Giga years is plotted from the time when the shock started emerging. The y axis shows the average of the above mentioned ratios evaluated for different analysis sphere placed behind the shock. Error bars are the standard error of the results from the analysis at each redshift.* 86
- 7.15. **Panel 1:** *Vorticity i.e. $\nabla \times v$ map of the shock front. It can be clearly noticed that the vorticity is extended to few hundred kpc behind the shock front. Data taken along the indicated line is plotted to measure its exact maximum extension in Fig. 7.15.* **Panel 2:** *Data from the panel 1 Fig.7.15 along the line indicated is taken and a line plot is prepared to calculate its exact extension. The Full Width at Half Maximum could thus be measured to quantify the extended turbulent region behind the shock front. From the above figure the extension has a value of about $230 \text{ kpc } h^{-1}$ * 87
- 8.1. **Panel 1:** *A superimposed image of VLA 20cm radio and ROSAT 0.14-2keV X-ray map; Image is taken from Bagchi et al. (2006). Reprinted with permission from AAAS.* **Panel 2:** *Simulated temperature map of the merging cluster is drawn as a contour, projected X-ray surface brightness (0.14-2.0 keV) is superimposed as a colour image;* **Panel 3:** *The inset shows an enlarged map in vorticity for the western shock front of the simulated cluster.* 89

List of Figures

.

1. Introduction & Motivation

1.1. Introduction & Motivation

Clusters of galaxies are the largest virialized structures that have formed during the evolution of the Universe. Their formation proceeds via hierarchical clustering, i.e. the continuous accretion of matter onto gravitationally bound structures of increasing mass and merger events between colliding clumps of smaller masses. An immediate consequence of hierarchical clustering is the formation of large-scale shock waves. Violent shocks result from accretion of external matter as well as from collisions of galaxy sub-clusters and clusters with characteristic velocities of about 1000 km s^{-1} .

Generally the ratio of colliding masses ranging from 1:10 to 1:1 are known as mergers. Those who has the mass ratio close to 1 are called the major mergers (for details see the section 2.3.1.1). Major mergers are regarded as the most energetic events since big bang (Ritchie & Thomas 2002). They can supply a substantial amount of energy. An idealized merger of two $10^{15} M_{\odot}$ clusters colliding at $\sim 1000 \text{ km s}^{-1}$ releases an amount of energy as high as $\sim 10^{64}$ ergs, (Ricker & Sarazin 2001), which is transferred to the Intra Cluster Medium (ICM) heating it up to X-ray emitting temperatures. We therefore expect to find observational evidence of major mergers mainly from their X-ray properties.

Heating occurs through a cascade of processes involving shock waves and turbulence (Sarazin 2002a). The cluster merger and accretion shock waves, like most other astrophysical shocks, are ‘collision less’ features mediated by collective, electromagnetic interactions giving rise to an anomalous viscosity (Ryu et al. 2003). Collisionless plasma shocks can generate strong magnetohydrodynamic (MHD) waves and strongly amplify the upstream magnetic field present in the ICM (Bykov et al. 2008). Two competing processes are working here. The compression at the shock results in acceleration of particles through first-order Fermi acceleration (Fermi I) (Drury 1983, Blandford & Eichler 1987), whereas a part of the turbulence energy can be transformed to non-thermal energy by second-order Fermi acceleration (Fermi II) or stochastic acceleration (Schlickeiser 1989). Owing to the synchrotron emission of the accelerated particles in the regions with amplified magnetic fields, we can expect to find observational signatures of the cluster merger process at radio wavelengths, too. If sensitivity permits, gamma ray observations could also trace particle acceleration.

Over the past decades, a substantial amount of observational evidence for major merger events has been obtained, mainly in X-rays and the optical. Only recently, radio observations

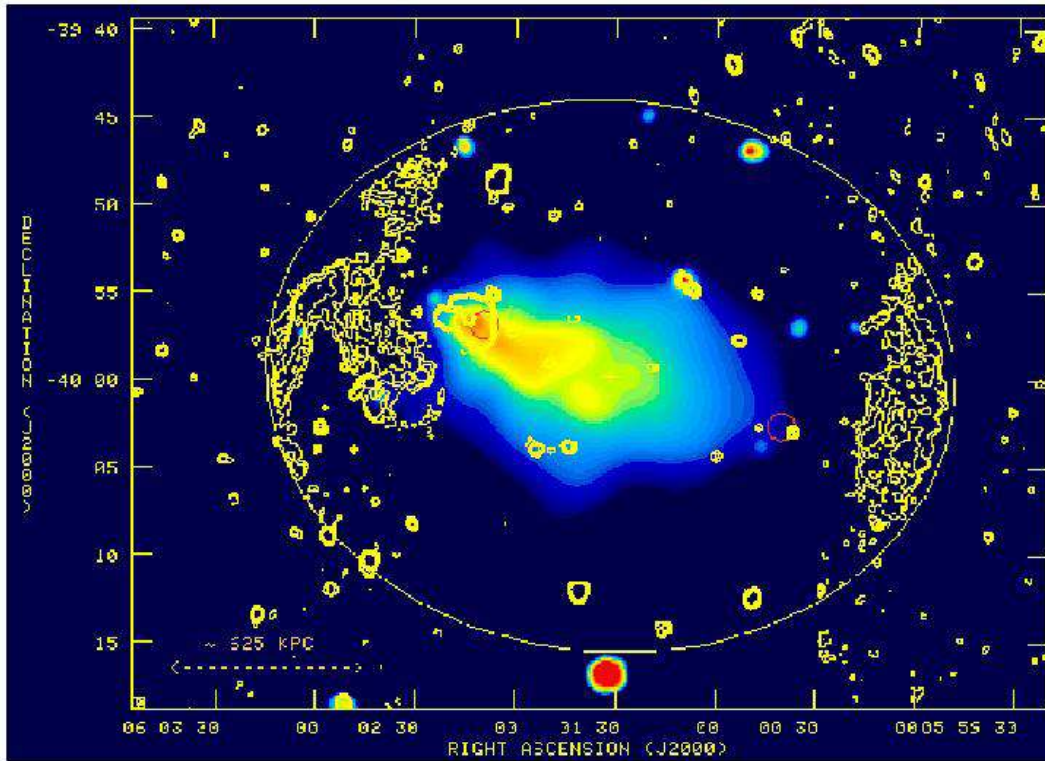


Figure 1.1.: A composite map of the radio and X-ray emission from the cluster Abell 3376. The VLA observed 1.4 GHz total intensity contours (yellow) are: 0.12, 0.24, 0.48 and 1 mJy/beam. (Beam: 20" FWHM). The large ellipse shows an elliptical fit to the peripheral giant radio structure. The central colour image depicts the thermal bremsstrahlung X-ray emission observed with the ROSAT PSPC instrument (~ 12 kilo seconds exposure, 0.14-2.0 keV band). The red circles mark the positions of two brightest clusters. The shock structures found at 1.4 GHz radio frequency show a downstream extension of ~ 500 kpc and their length is more than a Gigaparsec. Image is taken from [Bagchi et al. \(2006\)](#). Reprinted with permission from AAAS

revealed structures in galaxy clusters that should be related with merger and accretion events. They are mainly of two types, the central radio haloes and the peripheral relics ([Enßlin & Gopal-Krishna 2001](#)). Among all such peripheral radio relics, a new class of “symmetrical radio structures” has been found. As per observational findings which neither have any correlation with the central radio halo nor can be equated with radio relics or revived structures. These structures can be called as ‘Radio Gischt’ as referred by [Kempner et al. \(2004\)](#). The structures are mainly found in active clusters of galaxies, where an event of massive merger or accretion is going on. Such a structure was seen for the first time in an Abell cluster (A3667) reported by [Rottgering et al. \(1997\)](#). Discovery of a double arc in Abell 3376

which could probably be a part of an elliptical shock structure was reported by Bagchi et al. (2006). Recent deep observation by van Weeren et al. (2009) and Bonafede et al. (2009) revealed similar double arcs in a filamentary merging cluster ZwCl 2341.1+0000 and Abell 2345 and Abell 1240 respectively. The structure found in above observations can be interpreted as the result of shock propagation in the ICM, where a massive merger of two clusters of galaxies resulted in the production of a broken parts of a ring-like structure in 2D i.e. a spherical shell in 3D with holes due to tunneling of cold gas along the dark matter filaments towards the centre of the cosmological filamentary nodes, nearly symmetrically propagated out of the merging centre to the periphery of the cluster.

Ensslin et al. (1998), Roettiger et al. (1999) and Miniati et al. (2001) have proposed a model of in-situ diffusive shock acceleration (DSA) by the Fermi-I process for generating some of such peripheral radio structures in the shocked ICM. The efficiency of acceleration of this process depends mainly on the Mach number. The Mach number at the shock fronts of Abell 3667, however, is estimated to be only ~ 1 (Vikhlinin et al. 2001), which is too small to produce the observed synchrotron radiation. Although Fermi-I acceleration of ambient electrons in the above mentioned clusters may take place at the merger shocks, it cannot provide good explanation for the structures behind the shock extending hundreds of kiloparsecs (see Fig 1.1). As the lifetime of the particles in the peripheral radio structures are very short compared to shock evolution time (lifetime $\sim 10^8$, shock evolution time \sim Giga year), it is unlikely that the emission can be observed so far from the shock fronts (Fujita et al. 2003). This invokes the possibility of considering other acceleration/re-acceleration processes such as the Fermi-II process which does not require very strong shocks but needs an Alfvénic or MHD turbulence in the ambient medium. As the decaying rate of Alfvénic turbulence is much slower than the energy loss rate of the shocked electrons, it can emit longer to produce much wider or extended structures. A relatively flat and extended region with no spectral gradient is expected in such cases. Fluid turbulence found in ICM of various cluster merger scenario in numerical simulations (Roettiger et al. 1999; Ricker & Sarazin 2001) support the above statement, if coupling between the compressible and non-compressible modes is assumed.

Cosmological simulations of clusters of galaxies in recent years indicate a key role of major mergers in the formation of massive shocks (Miniati et al. 2000a; Ryu et al. 2003; Mathis et al. 2005; Kang et al. 2007). Works of Miniati et al. (2000a) and Pfrommer et al. (2006) suggest two classes of shock wave populations, named as the ‘internal’ and ‘external’ shocks, respectively, depending upon the Mach number of the shocks, where the ‘external’ shocks are indicating accretion shocks and ‘internal’ shocks are actually the merger shocks. Although a morphological similarity between both kinds of shocks is expected, the former should be more effective in particle acceleration to the highest energies due to its higher Mach number. On the other hand, Ryu et al. (2003) suggested that ‘internal’ i.e. merger shocks are the most important in ICM heating, and they have been proposed by Bykov et al. (2008) to be the likely source of non-thermal emission of clusters. Ricker & Sarazin (2001) addressed the evolution of shocks in a series of ‘off-axis’ mergers of idealized sub-clusters

which have similar morphological appearance. The observations of the cluster Abell 3376 using the VLA show structures most likely arising from a major merger of two clusters. Thus, although accretion shocks should occur, simulations and observations indicate that merger shocks seem to be more reliable in explaining the structures found in clusters like Abell 3376 and Abell 3667. A more detailed discussion on 'external' and 'internal' shocks and their role in explaining the observed structures in Abell 3376 can be found in the later sections.

So far, the focus of previous studies centered on the morphology of the shocked medium and consequent effects on particle acceleration. Less attention was drawn on the role of turbulence and the effects of shock propagation on the ICM. Little effort has gone in explaining the post shock region, especially the extension of the radio structures behind the shock. Another drawback of most of the previous works is the highly idealized simulation setup that was used. The goals of this thesis work are to account for the first time for the effect of the propagation of merger shocks, their strength and their role in injecting turbulence in the ICM. My main objective will be to explain the extension of the observed shock structures in major merger events in terms of the injected turbulence. For the simulation, I use the hydrodynamical code ENZO and simulate several major merger events in a setup constrained by realistic cluster parameters. Information on the extension of the shock regions was obtained from radio observations of Abell 3376 performed with the VLA. Comparing the radio emission of the extended shock regions, the presence of Fermi-II acceleration or similar mechanisms which can tap the turbulent energy will be probed.

1.2. Structure

The plan of this thesis is to first briefly outline the astrophysical framework needed to understand the evolution of galaxy clusters and occurrence of major merger shocks in Chapter 2. In Chapter 3, I will summarize the status of the field and describe the main objectives of this thesis work in detail. Chapter 4 will cover observational and instrumental aspects, whereas Chapter 5 describes the VLA and X-ray data analysis and results from the observations of Abell 3376. They will be interpreted in the light of the merging cluster scenario. Deeper understanding of the observations is expected to arise from comparing them with numerical, constrained simulations of the merger event. The methodology is described in Chapter 6. We used ENZO, a AMR based Eulerian simulation code for our work. Basic parameters and the model used for simulating the merging cluster is explained in Chapter 7. This chapter also contains the description of the simulation setup, the selection of refinement criteria, the resolution study and the final results for the merger event. Finally, in Chapter 8, the results will be summarized to arrive at the conclusions from this work.

2. Evolution of clusters of galaxies and major merger shocks

2.1. Clusters of galaxies

Clusters of galaxies are the largest gravitationally bound objects in the cosmic structure formation process. The clusters can be expected to have reached the state of virial equilibrium as in general the cluster crossing time i.e. $t_c = R/V$ (where, R = estimated cluster radius and V = velocity dispersion) is much less than the Hubble time. Also, this is consistent with observations of numerous clusters observed and reported by [Turner & Gott \(1976\)](#), [Faber & Gallagher \(1979\)](#), [Sarazin \(1988\)](#) etc.

However, virial equilibrium of clusters are continuously disturbed due to the ongoing structure formation process like accretion of matters from the ICM or from the filaments, groups of galaxies, or collisions with other clusters. Owing to cosmic expansion, the relevance of these perturbations is decreasing with cosmic time. This is the standard lore of the concordance model.

Although no concrete parameters and numbers can be given to define a cluster of galaxies, from several references some limits for characterizing the clusters of galaxies are put and are listed bellow.

- Galaxy clusters are gravitationally bound systems, i.e. they are decoupled from the Hubble expansion, collapsing upon themselves and eventually entering a state of virial equilibrium.
- A typical cluster of galaxies contains about 100 or more bright galaxies and has a mass of about $10^{15} M_{\odot}$.
- The diameter of a cluster is of the order of Mega persec (Mpc).
- The temperature of the Inter Cluster Medium is 10^7 K to 10^8 K
- The velocity dispersion of galaxies and ICM is about 1000 km s^{-1}

The evolution of clusters of galaxies reflects their changing dynamical state in combination with concurrent physical processes (Sect. 2.3). Observationally, this evolution can be traced with representative samples of clusters of galaxies selected from complete surveys and physically characterized with detailed multi-frequency measurements (examples are given throughout the section 1.1, chapter 2 and section 3.1.1).

2.2. Clusters through structure formation

Structure formation refers to a fundamental problem in physical cosmology. The Universe, as it is now known from observations of the cosmic microwave background radiation, actually began in a hot, dense, nearly uniform state approximately 13.7 Gyr ago (Spergel et al. 2007). However, looking in the sky today, structures can be found on all scales below 100 Mpc, from stars and planets to galaxies and, on the largest scales, galaxy clusters and superclusters. These overdense regions form filamentary membranes wrapped around huge low-density regions, the so-called voids of characteristic size 50 Mpc.

Initial density fluctuation is the main driving force behind the structure formation. Within an isotropic and homogeneous background distribution, the cosmic web structure grows via the gravitational instability from these initial density fluctuations. According to the theory of structure formation, the creation and growth of structures can be explained by the following conditions. Initially there was some density fluctuation whose origin is not contained in the standard model of structure formation. Till date an inflationary era in the very early Universe is the most accepted and promising idea which predicts a Gaussian seed fluctuation relating quantum fluctuation to the macroscopic density perturbation (Guth 1981; Albrecht & Steinhardt 1982). Time evolution of amplitude of density perturbation in an expanding universe and the nature of the particles those interacting gravitationally determines the growth of structures. Growth of structures actually enters to a non-linear regime at the late time of its evolutionary phase and numerical N-body simulation becomes very useful in describing the phenomena. An example of structures in large scale is shown in the Fig. 2.1.

2.2.1. Role of Dark-matter in Structure formation

Dark matter plays a key role in structure formation because it interacts only through the gravitational force. Complex structures are allowed to form by the gravitational Jeans instability as it is not opposed by any other force like the electromagnetic force. As a result, dark matter begins to collapse into a complex network of dark matter filaments and halos well before the ordinary, baryonic matter, which is impeded by pressure gradient forces. About 83% of the total matter in the Universe being dark matter, dark matter potential controls the motion of baryons and forces to follow the potential gradient of dark matter. Without the dark matter, the epoch of galaxy formation would therefore occur substantially later in the Universe than it is observed, or not at all, since the cosmological Hubble expansion could have torn apart the overdense regions before they become gravitationally bound.

As dark matter perturbation in different wavelengths evolve independently, complications from coupling is avoided and the physics of structure formation became much simpler. Larger perturbations are induced as the Hubble radius grows and the dark matter perturbation grows through gravitational clustering in that matter dominated era. But the shorter-wavelength perturbations that are encompassed in the early phase of evolution i.e. during radiation domination have their growth retarded until matter domination. Due to domination of dark matter in matter dominated era, luminous, baryonic matter is expected to simply

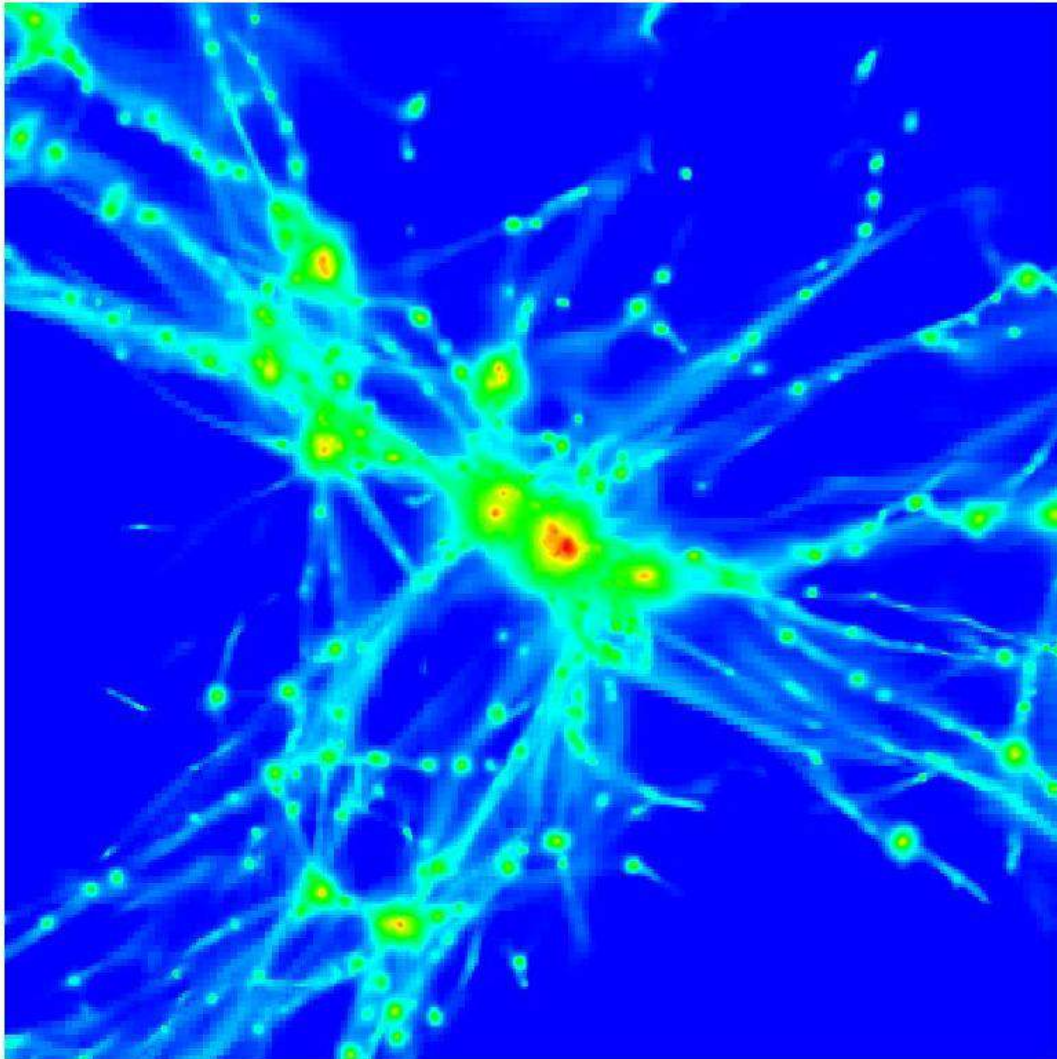


Figure 2.1.: *Projected density map of a filamentary structure in a 25.6^3 Mpc^3 co-moving volume. It shows how the clusters are embedded in a weblike filamentary structure. Mass is first channeled through those filaments and all the structures and sub-structures are dragged along the filaments and finally the nearest clumps are merged to form a bigger cluster. (Image source: S. Paul Galaxy merger project(2008))*

mirror the evolution of the dark matter. The density profile and distribution of them should thus closely resemble.

However, a notable exception occurs for major merging events. The baryonic matter does

not follow the dark matter profile as long as the cluster remains out of equilibrium due to violent merging event. The relaxation comes much later than the dark matter core of the cluster comes to a relaxed state. Thus, one can say that a delayed and independent initial evolution of baryonic gas is relevant in such cases, and must be considered when trying to set up a constrained simulation of colliding clusters of galaxies. A detailed description on this subject will be presented in section 2.3.3.1.

2.2.2. Pattern of structure and cluster formation

The hierarchical build-up of dark matter halos from small scales to successively larger scales forms the filamentary structure in the Universe. Big structures withstand the Hubble expansion and get gravitationally bound since the density perturbations have larger amplitude on smaller mass scales. In the course of evolution, the matter from low density ICM becomes accreted towards the high density dark-matter filaments and is channeled towards the denser regions or the nodes of the filaments. Since the structures grown in such process don't have definite geometric shapes, such an accretion process in realistic clusters is not symmetric. A time varying collective potential is thus produced by the infalling matters depending on the existing density profile and surroundings. The most probable state of such a particle velocity distribution is thus governed by Maxwellian velocity distribution. Phase mixing occurs in such system as the energy and angular momentum of individual particles are not conserved and is resulted in damping of bulk motion. The process is known as violent relaxation (Lynden-Bell 1967) and virial equilibrium is attained. In this state the equation of state eventually resembles continuity equation and momentum flux of particles that exits the boundary is balanced to that entering. Kinetic energy T_{kin} is thus related to the total gravitational potential energy T_{grav} through the equation

$$T_{\text{grav}} + 2T_{\text{kin}} = 4\pi P_{\text{inf}} r_{\text{inf}}^3, \quad (2.1)$$

where P_{inf} is the effective pressure due to infalling matter at the boundary r_{inf} of a collapsed system.

Once the process of collapse of cluster matter completes, the violent relaxation becomes ineffective and further relaxation can be viewed as a two-body interaction Chandrasekhar (1942). This process is mainly significant for large halos near the cluster core and the incident can be termed as 'major merger' in galaxy-cluster physics. In the actual physical picture, the previously mentioned small structures embedded in the web-like filamentary structures in the early epoch gradually grows due to accretion of matter. Those substructures then merge and coalesce with other nodes to form progressively larger structures. Although the basic concept of merger can be studied in analytical spherical collapse model (Gunn & Gott 1972; Fillmore & Goldreich 1984; Bertschinger 1985), as we earlier said, a better understanding of a real structure formation and merging event can only be studied through numerical simulations.

2.3. Theory of cluster merger and shock evolution

As I already discussed, the structure of the Universe is formed by clustering hierarchically from small to large scales. Much of this evolution occurs very slowly but at a few special times more rapid, violent activity may occur as major sub-units collide at high velocities. In this process, dark matter filaments are the principal agent. Filaments are usually connected to each other and form a web-like structure and each of the connection or node gathers a huge amount of matter to create a deep potential well (Bond et al. 1996, Einasto et al. 1997, Doroshkevich et al. 1996). Those heavy cores, when approaching each other, merge to form bigger cores or the cluster cores, respectively. Baryonic matter being much less compared to the dark matter actually follows the potential well created by dark matter web structures. The node when sufficiently grown, forms a cluster. Thus, in the history of formation of clusters, it experiences several mergers, some of them are very violent and are the most energetic process after Big Bang. (quantitatively, an idealized merger of two $10^{15} M_{\odot}$ clusters colliding at about 1000 km s^{-1} yields an energy as high as 10^{64} ergs, (Ricker & Sarazin 2001).

2.3.1. Cluster Merger Rates

Matter is always accreted towards the cluster center as the depth of potential is maximum at that point. The rate at which matter is accreted or matter clumps are merged depends mainly on the gravitational interaction of the darkmatter potential and the environment from which matter will be accreted. As a simple and effective model, the rates of cluster mergers as a function of the cluster masses and redshift is estimated by Press & Schechter (1974)[P&S here after] using a simple formalism. Basis of their model is the initial small amplitude Gaussian density fluctuation which leads to gravitational instability. As the fluctuation has larger amplitude on the smaller mass scales the galaxies and the clusters form hierarchically i.e. smaller structures like galaxies are formed much before the clusters came in to the picture. P&S formalism then studied and modified by several researchers like Bond et al. (1991) and Lacey & Cole (1993). In the modified model they assumed that the density fluctuations in the Universe are smoothed on a variety of mass scales. A spherical collapse model is considered to calculate the mass concentration and it is assumed that the collapse of structures takes place when density exceeds a certain critical value. The assumption of the extended P&S formalism is that larger structures are the attractors and smaller mass scales have thus merged in the larger objects. Estimation of abundance of clusters is thus calculated as a function of their mass. Let $n(m, z)dm$ be the comoving number density of clusters with masses in the range m to $m + dm$ in the Universe at a redshift of z . According to P&S, the differential number density is thus given by

$$n(m, z) dm = \sqrt{\frac{2}{\pi}} \frac{\bar{\rho}}{m^2} \frac{\delta_c(z)}{\sigma(m)} \left| \frac{d \ln \sigma(m)}{d \ln m} \right| \exp \left[-\frac{\delta_c^2(z)}{2 \sigma^2(m)} \right] dm \quad (2.2)$$

where $\bar{\rho}$ is the current mean density of the Universe, $\sigma(m)$ is the current rms density

2.3.2 Energy release in mergers

fluctuation within a sphere of mean mass m , and $\delta_c^2(z)$ is the critical linear overdensity for a region to collapse at a redshift z .

2.3.1.1. Accretion, merger and major merger classification

On the basis of equation 2.3.1 a modified and extended model for ‘dark halo’ evolution has been proposed by [Salvador-Sole et al. \(1998\)](#). In this model they assumed that when a halo of mass M experiences a merger and gets a final mass M' with, $\delta M/M \equiv (M' - M)/M$, if the ratio crosses a certain threshold value of Δ_m , the existing core of the cluster gets destroyed. This merger is regarded as the formation of a new cluster core and halo. If the ratio $\Delta M/M < \Delta_m$, the event represents simply the continuous accretion, the existing core and halo keep their identity and structure intact.

The mass accretion rate, $R_{\text{mass}}(M, t) \equiv dM/dt$ of halos with mass M in this model thus defined by

$$R_{\text{mass}}(M, t) = \int_M^{M(1+\Delta_m)} \Delta M r_{\text{LC}}^m(M \rightarrow M', t) dM' \quad (2.3)$$

Where, r_{LC}^m is the rate of merging for a cluster formation process where $M' > M$ according to [Lacey & Cole \(1993\)](#).

From above relation [Salvador-Sole et al. \(1998\)](#) in their work showed that the best fit for new cluster formation gives $\Delta_m = 0.6$ in a number of different cosmological models. So, cluster cores structures get destroyed when $\Delta_m \gtrsim 0.6$ and a new core and halo structure forms. However, accretion and merger can not be so sharply distinguished in the range $0.5 \lesssim \Delta_m \lesssim 0.7$. From the above relation an incident when $\Delta_m > 0.5$ can be called accretion, the incident where $0.5 \lesssim \Delta_m \lesssim 0.7$ can be called merger. Lastly if in a merger Δ_m is ≥ 0.7 it can be called a major merger.

2.3.2. Energy release in mergers

For an estimation of the energy released in a merger, a simplistic model can be imagined to have better control over the problem. If we assume a merging event between only two clusters of galaxies with masses M_1 and M_2 which had a head-on collision, the energy release amounts to

$$E_{\text{merge}} \sim \frac{GM_1M_2}{d}. \quad (2.4)$$

Where, d is the most probable distance where the dissipation through a collision-less shock occurs.

E_{merge} can even be equated to the total thermal energy of the ICM of a rich cluster which again nearly equals the total gravitational energy of an isothermal sphere of the same dimension ([Totani & Kitayama 2000](#)). Hence it follows that

$$E_{\text{merge}} \sim \frac{GM_1M_2}{d} \sim 3.5 \times 10^{63} \left(\frac{M}{10^{15} M_\odot} \right)^2 \times \left(\frac{d}{1.5 \text{ Mpc}} \right)^{-1} \sim E_G. \quad (2.5)$$

Where, M is the final mass of the cluster and $E_G \sim \frac{3}{4} \frac{GM^2}{r_{\text{vir}}}$

The typical mass of a cluster of galaxy is taken to be $\sim 10^{15} M_{\odot}$ and the shock wave is expected to occur around the merging circumference (i.e. r_{vir}) of each cluster, which is ~ 1.5 Mpc for such clusters. We thus scaled down the equation considering these factors.

The above model is the simplest approach to describe the basic features of a major cluster merger. More realistic models of such mergers involve the full nonlinear evolution, and hydrodynamical simulations (see section 7) must be employed to exploit their potential in describing detailed observations.

2.3.3. Effects of cluster mergers

The enormous energy produced in such cluster mergers needs some channel to be dissipated. Heating of the ICM is inevitable and a sudden rise in cluster temperature and the corresponding emission of X-rays can be observed (Ricker & Sarazin 2001). The gas dynamics are also affected significantly by major merger events. During a merger, the speed of the in-falling cluster is comparable to the escape velocity of the system and the square of the velocity is larger than the gravitational potential, hence the motions in the cluster merger are expected to be supersonic. This certainly ensures the generation of shocks in the ICM (Sarazin 2002b). Rottgering et al. (1997), Bagchi et al. (2006), van Weeren et al. (2009) & Bonafede et al. (2009) reported their observations of such phenomena in the radio and X-ray bands in various clusters. The shocks then inject a high level of turbulence into the ICM, amplify the seed magnetic fields present in the ICM, and convert thermal to non-thermal energy by accelerating particles at the shock and by stochastic re-acceleration by momentum diffusion in the turbulent medium.

Thus, the effects of mergers can be summarized as a

- Change in gas dynamics and kinematics
- Generation of megapersec-scale shocks
- Injection of turbulence in the ICM and amplification of magnetic fields
- Acceleration of particles (i.e. transfer of energy to non-thermal particles).

2.3.3.1. Change in gas dynamics and kinematics

Gas dynamics in a merged cluster The intracluster medium (ICM) is generally close to hydrostatic equilibrium in clusters which are not undergoing strong mergers. The dynamical behaviour of the baryonic gas in such clusters is thus very smooth and the gas density always follows the dark-matter density profile. On the contrary we see an initial, nearly independent evolution of the gas density profile even after the dark matter core has merged totally and dark matter density came to a rest. The panel of figures in Fig. 2.2 (produced by S. Paul

2.3.3 Effects of cluster mergers

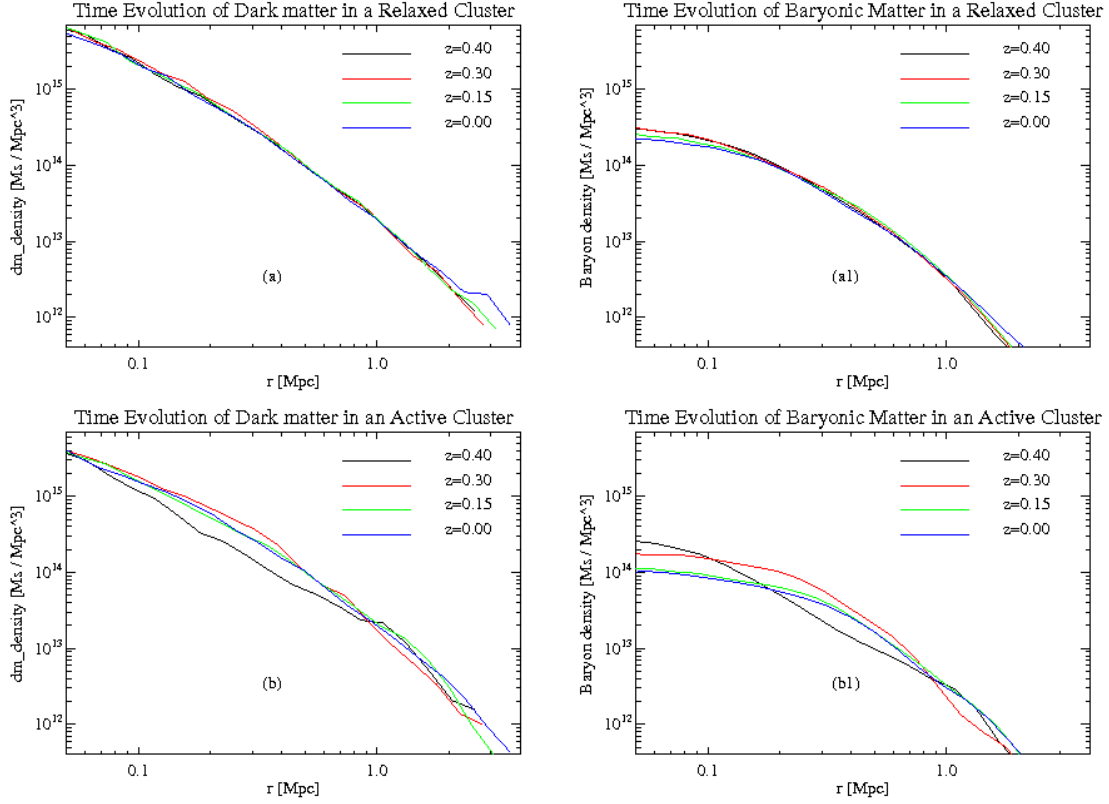


Figure 2.2.: Panel (a) and (a1): Radial dark matter and gas density variation in a relaxed cluster at different redshifts. The gas density clearly follows the dark matter profile; **Panel (b) and (b1):** Radial variation of dark matter and gas density profile respectively in an active cluster of galaxies. Disturbed dark matter profile at different redshifts can be seen, the gas profile becomes flattened.

Galaxy merger project(2008) in a collaborative effort during this thesis work) shows the evolution of dark matter and gas in case of a relaxed and a merged cluster.

For a better understanding of the merging cluster case, a comparison of several parameters of a relaxed cluster and a merging cluster grown in nearly the same astrophysical environment with the same initial parameters of the simulation is plotted. Both have almost equal final masses of $4.73 \times 10^{14} M_{\odot}$ and $4.80 \times 10^{14} M_{\odot}$, respectively. I plotted the radial variation of dark matter and baryonic matter density of the relaxed and active cluster by spherically averaging the values (see Fig. 2.2). The first and second panel, i.e. plot (a) and (a1), show the dark matter and baryon density of the relaxed cluster and the values are computed for different redshifts. It is seen that all the curves are fairly smooth and show very little variation in baryonic matter for the case of a relaxed cluster. There is nearly no change with time.

On the contrary the curves plotted for the active cluster show strong variation, especially for the baryonic matter density profile. The baryon density profile becomes flattened as it evolved through the merging phase. After the shock evolved, the central baryonic density decreased by a noticeable amount and inflated towards the outskirts of the cluster. Even after the core oscillation of the active cluster stopped, the ripped-off baryonic matter from the central part due to shock evolution didn't return to its initial stage and a flat central distribution of baryonic mass can be observed.

Thermal heating of Gas in a merged cluster The energy that is released from a merging cluster is mainly the converted kinetic energy of the dark matter components. Most of the studies regarding the physics of merging clusters suggest that the main channel of dissipation of energy released in the merging of clusters is the adiabatic heating of the cluster medium (Blasi 2001). Due to the supersonic flow of the bayonic matter from two different clusters, a strong shock is formed at the interaction surface and propagates through the ICM. The released energy is thus transferred from dark matter to baryons (and electrons). This process is also thought to produce the heating of the intra-cluster gas after the cluster mergers (Blasi 2000). Although the cluster medium is heated up by the shocks, as the shock passes by, a cold front is generated just behind the shock due to the sudden expansion of the medium which adiabatically cools it. There is a second process of heating, this is the re-collapse of the dark matter cores to the new cluster centre followed by the baryonic matter. In most of the cluster mergers, the cluster cores do not really come to rest immediately after the merger, but rather enter an oscillatory phase of the core collapse, as first noticed by (Tittley & Henriksen 2003). Thus, when the cluster core re-collapses, the heating of the cluster centre reaches its maximum. In summary, a series of heating and cooling epochs can be identified in the history of a colliding cluster. Due to the massive heating in the merged cluster, its usual temperature reaches high values around 10^7 K to 10^8 K. In chapter 7, I will discuss the situation elaborately in the light of the results obtained from the numerical simulations.

X-ray emission from merging clusters X-ray emission from the core of the cluster of galaxies is mainly due to radiation from thermal and non-thermal Bremsstrahlung. X-ray emission from a merging cluster core shows not much significant differences in X-ray brightness from an evolved cluster (Perrenod 1978), morphological difference are very prominent. Due to the ongoing motion at the core of the merging cluster, the X-ray emission from the hot gas, following adiabatic compression and relaxation, develops several peaks and crest. In addition, a significant amount of non-thermal hard X-ray components are found in merging clusters (see Durret et al. 2005; Nakazawa et al. 2009 and Nakazawa et al. 2007). The energetic particles that emit radio waves by synchrotron radiation in the periphery of the merging cluster also up-scatter photons from the cosmic microwave background radiation (CMBR) by inverse Compton scattering to produce the excess of hard X-rays found in merging clusters. The ratio of hard X-ray IC emission to radio synchrotron emission allows

2.3.3 Effects of cluster mergers

one to determine the magnetic field in clusters (e.g., [Rephaeli 1979](#); [Fusco-Femiano et al. 1999](#)). Since these higher energy electrons have short lifetimes, they should only be present in clusters with evidence for a recent or ongoing merger.

2.3.3.2. Generation of megaparsec-scale shocks

When two or more clusters of galaxies or sub-cluster of galaxies approach each other, the dark matter cores merge followed by the baryonic gas. The deep potential well formed by the dark matter in the centre of the newly formed cluster severely attracts and thus baryonic mass is rapidly driven to the centre by the intense gravitational potential created there. Normally, in relaxed clusters where hydrostatic equilibrium is expected and according to the virial theorem, the square of thermal velocity is equal to the gravitational potential. However, the scenario is very different in the case of a cluster that is going through a major merging phase. During a major merger, the infall velocities of the subclusters are comparable to the escape velocity of the cluster, which implies that the square of the infall velocity is larger than the gravitational potential. Thus, the motions in cluster mergers are expected to be supersonic. The baryonic matter of the merging clump is forced to move supersonically and thus takes away the energy released in the merger. An abrupt change, almost a discontinuity, in the cluster medium properties occur and eventually shock waves emerge at the merging surface of the two different gas clouds of the two clusters or subclusters. The huge energy released from the merged dark matter halos and the interacting baryonic gas thus open a channel to dissipate through powerful shocks in the ICM.

Effects of the major shocks on the ICM These shocks are considered responsible for the thermalization and virialization of the entire cluster. Merging immediately heats up the central halo of the cluster through adiabatic compression, but the shocks carry away the heating process all the way to the outskirts of the cluster. Simulation of [Mathis et al. \(2005\)](#) and [Skillman et al. \(2008\)](#) show that after the emergence of shocks in the cluster centre, the outwards propagating shocks heat up the ICM to several times the pre-existing temperature. In their interaction with filamentary large scale structures surrounding the clusters, the shock creates a warm-hot ICM. The evolution of the gas in the cluster is also effected by shocks ([Pfrommer et al. 2008](#)).

The most well-known effect of the shock is its power of efficient acceleration of particles. These cluster shocks are collisionless features whose interaction in the hot plasma are mediated by magnetic fields and wave-particle interaction. It is thus possible for the shocks to transform some fraction of the thermal distribution of particles into nonthermal cosmic rays by diffusive shock acceleration (DSA) ([Drury 1983](#); [Blandford & Eichler 1987](#)). They are also responsible for injecting turbulence in the ICM, and so stochastic acceleration of particles (i.e. the re-acceleration of particles through the Fermi-II process or momentum diffusion) is also expected to occur in the vicinity of the shocks. Details of the discussion will dealt with in a separate section.

2.3.3.3. Injection of turbulence into the ICM and amplification of magnetic field

Merging of clusters of galaxies induce large scale bulk motions with velocities of the order of about 1000 km s^{-1} . Bulk motion of the ICM gas and mixing of different medium of the merging clumps thus results in complex hydrodynamic flows, causing it to become convectively unstable. Large scale turbulent motions having eddy sizes upto 100s of kpc is generated via Kelvin-Helmholtz instabilities at the interface between the bulk flows and the primary cluster gas. This turbulence is then pumped by dark matter-driven oscillations in the central gravitational potential. Thus in general, although most of the kinetic energy of a merging system is considered to dissipate to thermal heating of the ICM through shocks and adiabatic compression, a noticeable part of the energy may also excite long lasting (Giga year long) turbulent gas motion in the medium (Dolag et al. 2005). Turbulence initiated in the post shock medium which propagates along with the shock through the ICM, is responsible for the whole region inside the virial radius to become filled up with eddies from kpc to Mpc scales. A detailed study of this done here, and will be presented in Chapter 7. Observationally, spatially resolved gas pressure maps of the Coma cluster obtained from a mosaic of XMM-Newton observations have indeed revealed the signature of mildly supersonic turbulence, at least in the central regions of the cluster (Schuecker et al. 2004).

Effect of turbulence on ICM Cluster mergers may produce a significant level of turbulence in the ICM and in principle can store an appreciable fraction (about 20%, Norman & Bryan 1999) of the thermal energy of the ICM in massive clusters, which would make it an important factor for understanding the structure of the ICM. Shear flows associated with cluster turbulence and the resulting dynamo processes could considerably amplify the magnetic field strength in the ICM (e.g. Dolag et al. 1999; Dolag et al. 2002). In addition, magnetohydrodynamic (MHD) waves can be efficiently injected into the ICM directly by shocks, by KH or Rayleigh-Taylor instabilities, or by the decay of turbulent eddies at larger scales. These waves, as well as shocks, can efficiently accelerate supra-thermal particles in the ICM to higher energies. Turbulent re-acceleration has also been suggested as a possible mechanism to explain radio halos in clusters (Brunetti et al. 2001; Eilek & Weatherall 1999).

Although there is still some debate concerning the detailed mechanism responsible for the origin of relativistic particles and magnetic fields in the ICM (e.g. Brunetti 2003), the presence of relativistic electrons and of $\sim \mu\text{G}$ strength magnetic fields in the ICM is proven by non-thermal emission studied with radio observations and possibly observations of hard X-ray emission (see Fusco-Femiano et al. 2003, for a review). Radio halos have only been found in merging clusters. However, their smooth distributions and central locations suggest that they are not confined to the region currently passing through a merger shock. Turbulent acceleration following the passage of merger shocks might explain these properties. In addition, the occurrence of non-thermal phenomena is found to be related to the dynamical state and mass of the parent cluster (Giovannini et al. 1999; Buote 2001; Bagchi et al. 2006), which suggests a connection between cluster mergers and non-thermal activity.

2.3.3.4. Acceleration of particles by shock and turbulence

Radio observations of large arcs or relics at the outskirts (Rottgering et al. 1997 & Bagchi et al. 2006) of clusters indicate that there is some mechanism that accelerates particles even far away from the cluster. Since the presence of magnetic fields in clusters has already been proved by observational evidence (e.g., Feretti et al. 1999; Giovannini et al. 1993), there is no doubt that the synchrotron emission of charged particles is the only plausible explanation for those structures. However, to obtain synchrotron emission we need a population of accelerated charged particles in the ICM. The most probable mechanism for particle acceleration is the diffusive shock wave acceleration at the shocks generated in the ICM due to the merger and accretion activity. Merger shocks convert at least a few percent of the shock energy into the acceleration of relativistic electrons (e.g., Blandford & Eichler 1987). The merger shocks have relatively small Mach numbers (2-3), and as a result exhibit smaller compression ratios. But the Alfvén Mach numbers ($M_A \equiv v_s/v_a$ where, $v_a = B^2/(4\pi\rho)$ is the Alfvén speed) for merger shocks can be quite high i.e. $M_A \gtrsim 30$. These shocks are subsonic in the electrons as the ICM that is entering in to the shock is relatively hot.

The theory of astrophysical particle acceleration has first been introduced by Fermi in Fermi (1949) and further the same concept was used to describe the particle acceleration at shocks by Skilling (1975), Webb (1983) etc. Fermi's concept was that the CRs gain energy when scattering off magnetized clouds of gas moving through the interstellar medium. Essentially the particles can gain energy as it elastically scattered off magnetic turbulence structures or magnetic irregularities which is tied to the partly ionized gas that moves with a characteristic velocity \mathbf{u} . Irregularities in magnetic field are ubiquitous in a plasma that gets stirred by ionization fronts, stellar winds, supernova explosions, or by high energetic particles moving through. The collisions between the cloud and the CRs are practically an elastic collision in the rest frame of the cloud as the cloud as a whole is a massive with respect to the each CRs. Since the direction of the CR is randomized by the scattering the energy change of a particle in co-moving scattering frame can be written as

$$\Delta\epsilon := \epsilon_2 - \epsilon_1 = 2\Gamma^2 (\epsilon_1 u^2/c^2 - \mathbf{p}_1 \cdot \mathbf{u}) \quad (2.6)$$

where, $\Gamma = (1 - u^2/c^2)^{-1/2}$ is the Lorentz factor, $\mathbf{p} = \mathbf{E}\mathbf{v}/c^2$ the particle momentum and the indices 1 and 2 denote particle properties before and after scattering. A particle thus gains or loses energy depending on whether it suffers head-on/approaching ($\mathbf{p}_1 \cdot \mathbf{u} < 1$) or following/ overtaking ($\mathbf{p}_1 \cdot \mathbf{u} > 1$) collisions.

Diffusive shock acceleration (DSA) or Fermi I process Shocks that are produced in the structure formation process are the most strong and energetic shocks known and are the natural acceleration machines that can provide relativistic particles from the astrophysical sources (e.g., Harris et al. 1980; Sarazin 1999). Fermi's original theory was modified to describe the more efficient acceleration that take place in converging flows such as at the astrophysical shocks generated in accretion or mergers. A collisionless shock wave is able to

accelerate ions from the high-energy tail of the Maxwellian energy distribution of particles through a process called diffusive shock acceleration. Interaction of these high energetic particles (charged particles like electron and proton) with the magnetic irregularities through magnetic resonances between the gyro-motion and waves in the magnetized plasma able to gain energy. The particles actually moves back and forth at the shock front gaining energy in each steps. Energy is gained due to difference in up and down stream velocity in which the particle move like a shuttle.

In a strong (non-relativistic) shock the upstream velocity is much higher than the downstream velocity and transfer much energy to the particle that comes from downstream. The mathematical expression that determines the energy gain can be written as

$$\frac{\Delta\epsilon}{\epsilon} = \frac{u}{c} \quad (2.7)$$

Where, left hand side gives the fractional change in energy. In the upstream rest frame, the plasma from the downstream of the shock always approaches with velocity $u = \mathbf{u}_u \cdot \mathbf{u}_d$, so that in first order there will be only head-on collisions for particles crossing the shock front. This is a stochastic acceleration process and statistically thus always leads to a gain in energy, so that for magnetic turbulence structures virtually comoving with the plasma flow, the energy gain [eq. (2.6)] becomes first order in u/c .

Fermi acceleration produce a power law particle acceleration spectra $N(\gamma) \propto \gamma^{-\sigma}$ if the particles pass a non-relativistic shock. In the reduced form of the acceleration equation it is seen that the acceleration of particles mainly dependent on the shock compression ratio $r = u_u/u_d$ (where $1 < r < 4$). The compression ratio is again related to the shock strength i.e. Mach number with the relation $r = \frac{\gamma+1}{\gamma-1+2/M^2}$, where, $M = u/c_s$, c_s is the sound speed of the medium. The power law spectrum that one can expect from a DSA particle is related to compression ratio with a simple relation in the non-relativistic regime as

$$\sigma = \frac{r+2}{r-1} \quad (2.8)$$

Second-order Fermi acceleration or stochastic acceleration The post shock region has non-negligible random velocity components due to the turbulence injected by the shocks in the ICM. In such a turbulent medium the particles will experience both head-on and overtaking collisions, i.e., lose and gain energy. However, as the rate of collisions is proportional to $|v_1 - u|/v_1 \simeq (1 - v_1 u/v_1^2)$, there is a higher probability for head-on compared to overtaking collisions, which gives an average energy gain (averaging over all the momentum directions) per collision that is second order in u/c , i.e.,

$$\frac{\langle \Delta\epsilon \rangle}{\epsilon_1} \propto \left(\frac{c}{u}\right)^2 \quad (2.9)$$

It thus represents a stochastic acceleration process due to many small, nonsystematic energy changes. The equation thus can be described by a diffusion equation in momentum

2.3.3 Effects of cluster mergers

space (Skilling 1975; Melrose 1980), which resembles the Fokker-Plank equation with drift and diffusion coefficients, and written as

$$\frac{\partial f(p)}{\partial t} = \frac{1}{p^2} \frac{\partial}{\partial p} \left(\partial p^2 D_p(p) \frac{\partial f(p)}{\partial p} \right) \quad (2.10)$$

with $D_p(p) \propto \langle (\Delta p)^2 \rangle$ the second order term that measures the diffusion coefficient in the momentum space. To solve the Fokker-Planck coefficients, a small anisotropy of the particle distribution in the laboratory frame is considered (Duffy & Blundell 2005). Statistically treating and considering the scattering off forward and reverse propagating Alfvén waves a similar expression is derived to express the FK coefficient (see Skilling 1975; Melrose 1980 and Webb 1983) as

$$D_p(p) \simeq \frac{p^2}{3\tau} \left(\frac{V_A}{c} \right)^2 \quad (2.11)$$

where, $V_A = B/\sqrt{4\pi\rho}$ is the Alfvén velocity. This implies a characteristic acceleration timescale

$$t_{acc} = \left[\frac{\partial}{\partial p} (p^2 D_p) \right]^{-1} = \frac{3}{(4-\sigma)} \left(\frac{c}{V_A} \right)^2 \tau \quad (2.12)$$

Where, $v \sim c$ gives $D_p = (u/c)^2 p^2 / (3\tau) \propto p^2 / \tau$, where, $\tau \simeq 1/(n\sigma c)$ is a mean scattering time and n is the number density of scatterers.

A much flatter particle spectra is expected from the second-order Fermi acceleration, which is $N(\gamma) \propto \gamma^{-\sigma}$, than the one produced by strong DSA, i.e., $\sigma < 2$ (cf. also Virtanen & Vainio 2005). A steady state solution of the equation 2.10 can verify the above mentioned result, which can be achieved by putting a mono-energetic source term $Q\delta(p-p_0)$ and particle loss term as $-f/T$. The solution gives a complicated spectral index.

$$\sigma = \frac{3}{2} \sqrt{1 + 16t_{acc}/(9T)} - \frac{1}{2} \quad (2.13)$$

Considering $t_{acc} \geq T$, i.e. particle loss time to be longer than particle acceleration time, a much flatter spectral index is obtained.

3. Current status of research and the objectives of the thesis project

3.1. Current status of the research in this field of shock evolution and its effects

The main purpose of this thesis project was to investigate in more detail how the merger shocks can accelerate particles and thus contribute to radiatively dissipating the collision energy. Here, I will describe the status of the research on the merger shock waves, a rather novel problem with only a few seminal results so far. The open questions about these rare structures are overwhelming.

3.1.1. Status of research on merger shock evolution

The first observational evidence of a huge shock front emerging in a major cluster merger has been reported by [Rottgering et al. \(1997\)](#) for Abell 3667. This is a massive cluster with mass greater than $10^{15}M_{\odot}$ that exhibits a variety of observational signatures of a recent cluster merger. Deep imaging at 20cm wavelengths revealed a pair of megaparsec-scale radio structures of diffuse emission that resemble huge bow-shocks. The observations were carried out with the Australian Telescope Compact Array (ATCA). The total extent of the radio features is 2.6 Mpc. They are located close to the periphery of the cluster. [Roettiger et al. \(1999\)](#) demonstrated employing a rather basic simulation setup that a major cluster merger would drive shock waves towards the outskirts of the cluster that produce radio-emitting particles which would become visible in large arcs like those found in Abell 3667.

Very recently, another prominent shock structure has been discovered by a team of observers, including the author of this thesis ([Bagchi et al. 2006](#)), viz. the radio structure found in Abell 3376. Observations were carried out with the Very Large Array (VLA) of NRAO, USA. A large-scale [$\sim 2h^{-1}$ Mpc] ring-like synchrotron structure shows up in the images at 1.4 GHz frequency, possibly tracing the intercluster merger shocks around the rich cluster of galaxies Abell 3376, at redshift $z = 0.046$. Confirmation of this interpretation still awaits observations at multiple wavelengths. In particular, gamma ray emission can be expected, as first noted by [Bagchi et al. \(2006\)](#). However, the expected flux is difficult to observe with current instruments.

Although the observational status is far from satisfactory, and only few cases of such merger shocks are known, a considerable effort has been spend on trying to improve the un-

derstanding of them aided by theoretical modeling. The pioneering theoretical work on cluster mergers, shock evolution and particle acceleration is due to Sarazin (1999) and Ricker & Sarazin (2001). From the numerical simulation of a merger between two predefined clusters Roettiger et al. (1999) came to the conclusion that the radio structures found in Abell 3667 are indeed due to the major cluster merger. On the other hand, (Miniati et al. 2001, Ensslin et al. 1998, Ryu et al. 2003, Pfrommer et al. 2006) worked on particle acceleration due to the evolution of shocks in the cluster medium. Hoeft et al. (2005) studied “radio relics” in cluster mergers. Mathis et al. (2005) presented rigorous results on the post shock conditions of the ICM. Their work deals mainly with the cold front generated when the shock waves passes through the ICM. In a recent paper, Ryu et al. (2008) explain the injection of turbulence by shocks in the ICM. A detailed simulation of the entire evolution of the shocks, from their appearance until the time when they reach the outskirts of the cluster, is still lacking. Correspondingly, the injection of turbulence could then be described quantitatively, allowing for studying particle acceleration by the Fermi-II process in the turbulent wake.

3.2. Objectives of the thesis work

The plan of this thesis is to observe the radio structures, presumably the merger shocks, found in Abell 3376 in more detail and to compare with state-of-the art numerical simulations. The anticipated result is to

- understand the origin of the observed radio structures in the framework of the cluster merger scenario,
- determine the role of the shock waves in generating turbulence and quantification of turbulence injection into the ICM,
- find out how merger energy is converted into non-thermal particle energy in the shocked regions.
- The energy reservoirs which can be tapped are the turbulent energy (Fermi-II) and the shock kinetic energy (Fermi-I). The acceleration mechanisms reveal themselves in the continuum spectra and their spatial gradients. The simulations will help to constrain better the Mach number of the shock and the turbulent region behind the shock, as it passes through the cluster merger. Cluster merger shocks hold the potential to accelerate particles to extremely high energies.

3.2.1. Milestones

- Multi-wavelength observation of the shock structures in the merging cluster Abell 3376.

- Constrained simulation of a major cluster merger to study the emergence and evolution of giant shocks within web like cosmic filamentary universe.
- Quantification of turbulence injection and its evolution during the cluster formation process.
- Prediction of nonthermal radiation from the shock and turbulent downstream regions.
- Comparison of simulation and observation.

3.2.1 Milestones

.

4. Observation basics and details of data analysis

In the past decades a substantial amount of X-ray and optical observations have been interpreted as major merger of galaxy clusters, but only recently scientists have discovered such phenomena in radio waves. The radio structures found in galaxy clusters are either the central radio haloes and the peripheral relics (Enßlin & Gopal-Krishna 2001). Among the peripheral radio relics, a new class of “symmetrical radio structures” has been found in a few cases, which are as per observational evidences till date has no relation to the central radio halo. There is also no strong evidence or statistics to call them radio relics with high confidence level. These structures are mainly found in “active” cluster of galaxies, i.e. where an event of massive merger or accretion is going on. The structures seen in the radio band seem to be produced by shock propagation in the ICM, out to the virial radius, following a massive merger of two clusters of galaxies. Their actual shape can be described as a broken parts of a ring-like structure in 2D; or in 3D it is an ellipsoid with holes due to tunneling of a cold flow along the dark matter filaments towards the centre of the cosmological filamentary nodes, nearly symmetrically propagated out of the merging centre to the periphery of the cluster. First evidence of such kind was discovered in the cluster Abell 3667 and was reported by Rottgering et al. (1997). But another discovery of a similar structure in A3376 by Bagchi et al. (2006) made scientists curious about exploring the origin of such objects. Recently thus statistic is going up day by day. A filamentary merging cluster ZwCl 2341.1+0000 has a similar double arc with total cluster size of 2.2 Mpc van Weeren et al. (2009). Also the double radio arcs in clusters Abell 2345 and Abell 1240 is observed recently by Bonafede et al. (2009). These are probably the best cases of observational evidence for major mergers in radio waves.

4.1. Radio observations and data analysis

4.1.1. Radio astronomy basics

I will now introduce the basics of radio astronomy that are needed to describe the imaging of an object at radio wavelengths. Unlike optical telescopes, radio telescopes are different by their method of observation, collection of data and unlike direct imaging of optical sources with photography plates or CCD panels, it has to be processed in computers after analysing the observed raw data. Antenna or telescope beam aperture captures the radio

4.1.1 Radio astronomy basics

waves generated by a celestial source that increases the antenna temperature. This value is then electronically stored as a noise. This noise corresponds to a temperature by Nyquist's theorem. Since radio waves carry too little energy to directly excite photon-sensitive material, no photographic or charge coupled device could be mounted to produce the image. Source signal is extracted using some computational techniques.

The different parameters relevant for determining the actual signal are given below:

The conversion of noise to temperature What radio antenna detects is just the noise. The antenna noise or source brightness is thus converted to an equivalent quantity in temperature. The conversion of noise to temperature is done using Nyquist's Theorem.

$$\omega = kT \quad (4.1)$$

where, ω is the spectral power per unit bandwidth (Watt Hz⁻¹). Boltzmann's constant is denoted by k , and T is the absolute temperature, i.e. the equivalent source temperature.

Using the above relations, different essential parameters for radio imaging are calculated in terms of the absolute temperature.

Antenna noise temperature The antenna noise temperature is determined by summing up the contributions from the target source, the astrophysical background radiation, background radiation from environment and atmosphere. Other local source of noise comes from mechanical changes of the telescope in operation and intrinsic noise from the receiver electronics and cables.

The cosmic microwave background and galactic continuum emission from our milky-way galaxy are the main elements of astrophysical background radiation. Environmental noise comes from the "hot" environment, and atmospheric noise. Also due to radio communication signals and weather-related processes that enters mainly through the side lobes of the antenna beam generates much of local noise. Effect of local noise depends strongly on the antenna geometry and the telescope location. Most of the intrinsic noise usually removed by calibration.

System temperature and source brightness temperature The system temperature is the temperature equivalent of noise generated by the entire system that is used to collect and transfer data to a storage medium. So, it includes all the noise contributions of system parts like antenna, Low Noise Amplifiers (LNAs), cable etc.. So, in a general formulation the system temperature of a system with series of antennas, LNAs and cables can be mathematically written as

$$T_{\text{sys}} = T_{\text{ant}} + T_{\text{lna}} + T_{\text{coax}} \frac{\left(\frac{1}{\epsilon} - 1\right)}{G_{\text{lna}}} + \dots \quad (4.2)$$

Where T_{ant} is antenna noise temperature,
 T_{lna} is noise temperature of LNA,
 T_{coax} is noise temperature by co-axial cable used for data transfer,
 G_{lna} is the gain of the LNA,
and ϵ is the loss factor of the cable, it can vary within 0 and 1.

The total flux of electromagnetic radiation from a source can be related to an effective or noise equivalent temperature, called the brightness temperature using the Rayleigh-Jeans law,

$$T = \frac{\lambda^2 B_\nu}{2k} \quad (4.3)$$

where, λ^2 is the wavelength of the source radiation and B_ν is the intensity of the source at a given frequency.

Sensitivity of a radio receiver Sensitivity of a radio telescope is defined as the ratio of total system temperature to the noise bandwidth over total integration time. i.e.

$$\Delta T = \frac{T_{\text{sys}}}{(t\Delta n)^{1/2}} \quad (4.4)$$

where t denotes the integration time and Δn is the noise bandwidth.

Signal to noise ratio(SNR) The system noise will always be a combination of signal and source noise. Thus, the only way to extract the source value or the image data is to start with the position-dependent signal-to-noise ratio. Image is constructed after calibration during data analysis by allowing for an absolute flux determination.

Delectability of a source signal is dependent on the signal-to-noise ratio. If the ratio is well above unity, the source can be detected easily. However, if ratio is below one, then the system noise predominates over the source signal and makes detection impossible.

$$SNR = CS \frac{(t\Delta n)^{\frac{1}{2}}}{T_{\text{sys}}} \quad (4.5)$$

where, $C = \text{const.}$ depends upon the number of telescope or antennas used to observe the object.

Radio surface brightness If B is the spectral radiance of the source at a certain frequency ν the surface brightness is defined as $S = \iint_{\text{source}} B_\nu(\theta, \phi) d\Omega$. Spectral radiance is thus integrated over the solid angle made by the object at observing point to obtain the total flux.

4.1.2. Radio interferometry

In the previous section, the basic idea of radio data collection and analysis has been presented. Preparing the actual image from the collected data is a rather complex process. Large wavelength of radio waves makes it difficult to resolve the total image using a single telescope or antenna, because the telescope aperture with respect to the wavelength is generally small. To overcome this shortcomings usually a synthetic aperture is obtained from combining the data of several telescopes together. The total base line (antenna to antenna distance) then acts as the effective diameter of a single antenna and a huge synthetic aperture is created. The method thus increases the angular resolution much above the one for a single dish.

Minimum requirement to construct a radio interferometer is a pair of directional antenna that are tuned to receive radio emission in a desired Radio Frequency (RF) band from any source. The signals received from the two antennas are then cross-correlated (multiplied and accumulated) to produce an interference or cross-correlation “fringe pattern”. Fringe pattern is then analyzed using computational techniques to get image of the source observed.

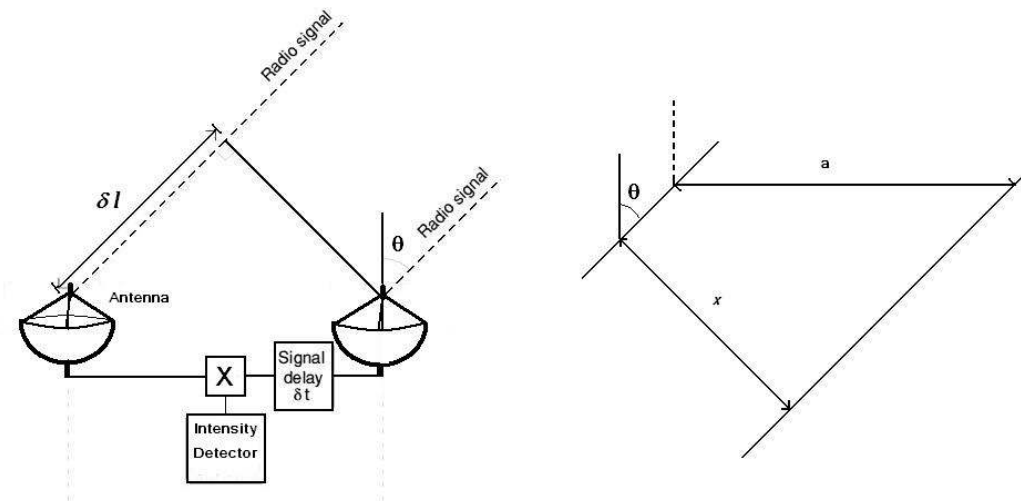


Figure 4.1.: Line diagram of a radio interferometry system.

Radio waves from a source that makes an angle θ to the vertical to the plane of antenna base need to travel further in order to reach till the left hand antenna (see 4.1). Signals at left hand antenna are thus delayed relative to the signals received at the right hand antenna by a time $c\delta l = ca \sin[\theta]$ where c is the speed of the radio waves and “ a ” is the antenna baseline separation. Compensation of the signal time delay at left hand antenna to that of right hand antenna is required in order to achieve a constructive interference. The signal from right hand antenna thus must be delayed artificially. Interference fringes will be produced by sources that comes within a very small range of angle either side of θ . Altering the delay

time δt varies the angle θ at which a source will produce interference fringes. The effective baseline of this interferometer will be given by the projection of the telescope positions onto a plane perpendicular to the source direction. With a telescope separation of “a”, the length of the effective baseline, shown at the bottom of Figure 4.1, will be $x = a \cos \theta$.

Dimension of separation variable actually determines the dimension of the sky map that can be constructed from any interferometer system. Interferometer consisting of only two antennas with separation variable in a single direction can only provide information about the sky brightness distribution in one dimension. However, when the separation vector is varied in two dimension, a 2D map of the sky can be produced. In Figure 4.2 (a,b) denotes the separation between two radio antennas in cartesian co-ordinates. The source makes an angle θ and ϕ with respect to the axis ‘a’ and ‘b’ axis respectively. As it is shown in the Figure 4.1, the effective baseline (x,y) will be the projection of the separation vector onto a plane perpendicular to the source direction: $(x,y)=(a \cos[\theta],b \cos[\phi])$.

Now, we measure the complex visibility in the Fourier transform plane of the sky brightness distribution using the dimensionless variable u conjugate to angle θ and v conjugate to angle ϕ . These can be calculated as $u = kx$ and $v = ky$, where k is the wave-number of the radio source defined as $\frac{2\pi}{\text{Mean wavelength}}$. Measurement of complex visibility for an antenna separation (a,b) can thus be calculated using the complex visibility function at two points in the u-v plane as given in the equation 4.6.

$$(u, v) = (kx, ky) = (ak\cos[\theta], bk\cos[\phi]) \quad (4.6)$$

$$(u, v) = (-kx, -ky) = (-ak\cos[\theta], -bk\cos[\phi]) \quad (4.7)$$

We can produce a perfect map of the sky brightness distribution if we have the complex visibility data for all points in the u-v plane i.e. in the Fourier transform plane. In order to produce a map with resolution equivalent to $n \times m$ pixels, the complex visibility must be known at all points in a $n \times m$ rectangular array in the u-v plane. The radio source brightness distribution $B(\theta, \phi)$ is reconstructed by Fourier transforming the array of complex visibility measurements. For an example I put an image which shows a typical cosmic radio source with brightness distribution $B(\theta, \phi)$ (see the left panel of the Fig. 5.1).

4.1.3. Technical details and specification of the Very Large Array (VLA)

In this section we will describe the VLA telescope system as a whole ¹. The VLA is a telescope that operates and observes astronomical objects at radio frequencies. Radio interferometry technique is used to image sources using VLA telescope which consists an array of 27 antennas. This means that it operates by correlating the data from each pair of telescopes together to form interference patterns. The structures of those interference patterns

¹Source for the description, data tables, figures of this section: VLA observational status summary 2008

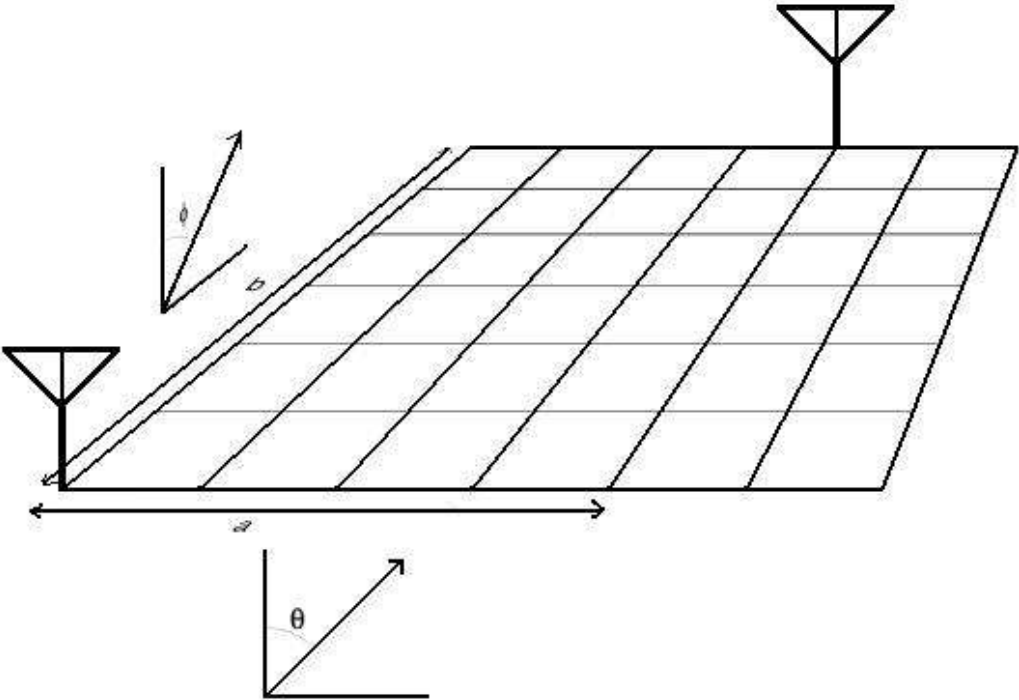


Figure 4.2.: Antennas on $u-v$ plane.

and the earth's motion reflect the structure of radio sources on the sky. We then use the Fourier transformation techniques to produce radio images or maps.

4.1.3.1. Information about VLA

Location:

- Plains of San Agustin, west of Socorro, New Mexico
- latitude = $34^{\circ} 04' 43.497''$ north
- longitude = $107^{\circ} 37' 03.819''$ west
- elevation = 2124 m (6970 ft)

Size:

- Each antenna: is 25 m (82 ft) in diameter, 230 tons in weight
- The array: its an Y shaped array with 27 elements. they are arranged in four configurations, A array, with a maximum antenna separation of 36 km; B array - 10 km; C array - 3.6 km; and D array - 1 km. The telescopes are switched between these configurations every four months or so.

Resolution: Size of the array determines the resolution of the VLA antenna system. When it has the largest baseline i.e. in A configuration with separation up to 36 km (22 miles), at the highest frequency (43 GHz), this gives a resolution of 0.04 arcseconds. At this resolution it can resolve a radio emitter of the size of a golf ball from 150 km (100 miles) distance.

Antenna information:

- Slew rates: 40° per minute in azimuth, 20° per minute in elevation
- Minimum elevation angle: 8° above the horizon
- Frequency coverage: 74 to 50,000 MHz (400 to 0.7 cm)

4.1.3 Technical details and specification of the Very Large Array (VLA)

4.1.3.2. Technical details of VLA

The VLA consists of 27 elements or antennae which form an interferometric array. The array is arranged along the arms of an upside-down “Y”. The antennas are located at an elevation of 2100 meters on the Plains of San Agustin in Southwestern New Mexico, and is managed from the Pete V. Domenici Science Operations Center (DSOC) in Socorro, New Mexico. The VLA produces images of the radio sky at a wide range of frequencies (wavelengths) and resolutions. All VLA antennas are permanently equipped with receivers for seven wavelength bands centered near $\lambda\lambda$ 90, 20, 6, 3.6, 2.0, 1.3, and 0.7 cm. Commonly these wave bands are referred to as P, L, C, X, U, K and Q bands, respectively. Details about wavelength and the maximum possible resolution is given in the table 4.1.

	4 Band	P Band	L Band	C Band	X Band	U Band	K Band	Q Band
Wavelength (cm)	400	90	20	6	3.6	2	1.3	0.7
Highest Resolution (arcsec)	24.0	6.0	1.4	0.4	0.24	0.14	0.08	0.05

Table 4.1.: Resolution of VLA receivers

The correlation of signals from different elements of the VLA array’s form the spatial coherence function or the visibilities. This is the basic data that is produced from VLA system. VLA data thus produced are suitably calibrated and images of the radio sky are prepared as a function of sky position and frequency.

VLA antennas are so made that they can be moved along a railway track and can be placed at a different distance over an array. Resolution can be varied over a range exceeding a factor of ~ 50 through movement. The whole array system is thus arranged in 4 basic configuration depending on the length of the arms of the ‘Y’ shaped array. The configurations scales in the ratio of 1: 3.2 : 10 : 32 from closest to the farthest in separation. Configurations are named as D, C, B, and A respectively. In addition to this, there a more three hybrid configurations called as DnC, CnB and BnA. In such hybrid configuration, northern arm antennas are kept in the next larger configuration than the South-East(SE) and South-West(SW) arms. Due to its elongated North arm it is very much effective for observation of Southern objects (where $\delta = -15^\circ$) or the objects that are at far North (i.e. beyond $\delta = +75^\circ$).

Data from each antenna are saved after passing through correlators which compensate the time delay referred in the section 4.1.2. VLA correlators are equipped with two basic modes, namely ‘continuum’ and ‘spectral’ line mode. Correlator in ‘continuum’ mode provides the four correlations (RR, RL, LR, LL) needed for full polarimetric imaging at both frequencies. This mode is particularly well suited to high sensitivity, narrow field-of-view objects. Spectral lines are observed in Spectral mode. A multichannel continuum mode is also enabled in some projects, mainly for projects with extremely hi dynamic range or a large field of view. This helps us to overcome the problem with Radio Frequency Interference (RFI) in the band pass which generally spoils a continuum observation.

Configuration	A	B	C	D
$B_{\max}(\text{km}^{(1)})$	36.4	11.4	3.4	1.03
$B_{\min}(\text{km}^{(1)})$	0.68	0.21	0.035	0.035

Table 4.2.: Configuration Properties

Configuration	A	B	C	D
20 cm	1.4	3.9	12.5	44.0
6 cm	0.4	1.2	3.9	14.0

Table 4.3.: Synthesized Beamwidth
 $\theta_{\text{HPBW}}(\text{arcsec})^{(1,2,3)}$

90 cm ⁽⁶⁾
20 cm	38.0	120.0	900.0	900.0
6 cm	10.0	36.0	300.0	300.0

Table 4.4.: Largest Angular Scale θ_{LAS} (arcsec)^(1,4)

Resolution The resolution of the synthetic antenna aperture of VLA, like a single normal radio antenna, is generally diffraction limited. This limit is set by the frequency of observation and the array configuration. Actually VLA synthetic antenna acts like a single antenna and thus structure smaller than the diffraction limit $\theta \sim \lambda/D$, broadened to the antenna resolution. Synthesis array has another important limitation i.e. it cannot see a structure whose angular size is larger or smaller than the range of fringe spacing set by antenna distribution. This shortcomings can be overcome by using shorter or smaller array configuration or using a large single antenna. Mosaicing several observations also can remove this problem to some extent.

A summary of some relevant information is given in the table 4.2, table 4.3 and table 4.4. Tables show the maximum and minimum antenna separations, the approximate synthesized beam size (full width at half-power), and the scale at which severe attenuation of large scale structure occurs.

Estimates of the synthesized beamwidth presented in the table 4.2,4.3 and 4.4 are for a uniformly weighted, untapered map produced from a full 12 hour synthesis observation of a source that passes near the zenith.

- 1. B_{\max} and B_{\min} denote the maximum and the minimum antenna separation. Synthesized beam width at FWHM is θ_{HPBW} , θ_{LAS} is the largest scale structure ‘visible’ to the array.
- 2. Above listed resolutions are appropriate for sources within the VLA normal range i.e. declinations between -15 and 75 degrees. Extended north arm hybrid configurations (BnA, CnB, DnC) should be used for observing objects beyond the normal range but within the declinations south of -30.
- 3. The approximate resolution is about 1.5 times the value listed for θ_{HPBW} in the specified table for a naturally weighted map. The values for snapshots are about 1.3 times the listed numbers.

4.1.3 Technical details and specification of the Very Large Array (VLA)

Frequency (GHz)	Approx λ	Band Name Letter Code	System Temperature ⁽¹⁾ K	Antenna Efficiency ⁽²⁾ in %	Number Antennas VLA+EVLA	RMS (10 min) Sensitivity in mJy	
0.3 - 0.34	90 cm	P	150-180	40	≤ 10	$> 4^{(3)}$	
1.24 - 1.70	20 cm	L	35	55	5+20	0.061	
4.5 - 5.0	6 cm	C	45	69	5+20	0.058	
Frequency	λ	RMS Source Sensitivity 12 hours	Point	Beam averaged Brightness Sensitivity ⁽⁶⁾ D-config	Antenna Primary Beam Size FWHP	Peak/Total Confusing Source in Beam	RMS Confusion Level D-config
in GHz		in mJy		in mKelvins	θ_{PB}	in Jy	$\mu\text{Jy}/\text{beam}$
0.3 - 0.34	90 cm	0.18 ⁽³⁾		21.3	150'	1.8/15	4400
1.24 - 1.70	20 cm	0.0071		0.8	30'	0.11/0.35	86
4.5 - 5.0	6 cm	0.0069		0.8	9'	0.002	3.6

Table 4.5.: VLA Sensitivity table

Sensitivity Expected VLA antenna sensitivity for natural weighted visibility data is shown in the table 4.5. Values given in the table are the expected rms fluctuations due to thermal noise on an image which is calculated using the standard formulae. Assuming that on an average 25 antennas work continuously the calculations were done with maximum 25 antennas (except for U band). Except for low frequencies, confusing side lobes from objects out side the image and ‘closure errors’, the tabulated values are experienced in reality. The rms limit due to confusing sources for the VLA in D configuration is estimated in table 4.5.

All sensitivity calculations assume 43 MHz bandwidth per IF, (except for P-band and 4-band, where 3.125 MHz and 0.78 MHz are used), two IF pairs (four IFs), natural weighting, and an elevation of 45 degrees.

- 1. At P, K, and Q bands, temperature ranges listed in the table include sky temperature variations due to the galactic plane (P-band) or Earth’s atmosphere (K band). System temperatures at the elevations below 45° for VLA antennas at L band are increased substantially due to ground pickup; EVLA antennas are nearly free of this problem.
- 2. Due to gravitational distortions of the antenna figure, efficiencies at U, K, and Q bands at low elevations (< 30 degrees) are decreased by considerable amount.
- 3. Sensitivity listed in the table is for Elevation = 45° and in a very dry atmosphere at 22 GHz. Wet weather actually increases zenith opacity from 5 to 15 percent, and increases the sky temperature from 10 to 40 K.
- 4. Sensitivity listed in the table is for Elevation = 45° and in a dry atmosphere at 43 GHz. Wet weather actually increases zenith opacity from 6 to 8 percent, and increase the zenith sky temperature from 15 to 24 K. Atmospheric attenuation and temperature increase is strongly dependent on frequency; sky temperatures thus exceeding even 55 K and zenith opacity goes to 25 percent at 49 GHz.

- 5. Values listed assume a uniform source that fills the synthesized beam in D configuration. Since natural weighting is assumed, the beam sizes are $\sim 50\%$ larger in each dimension than the values given in Table 4.

Elevation effect Elevation effects the performance of VLA antennas prominently. Changes are much significant at L, U, K, and Q bands, and must be corrected properly for high-precision imaging.

The loss of performance is due to two different effects:

- As the elevation decreases, the sky and ground temperature contribution to the total system temperature increase. As shown in the Figure 4.3, the effect is very strong at L, K, and Q bands. At K and Q bands, the extra noise comes directly from atmospheric emission, mainly from water vapor at K-band, and from water vapor and the broad wings of the strong 60 GHz O_2 transitions at Q-band. ‘spillover’ from the ground is the main source of excess noise in L band.
- At low elevation, forward gain at the shorter wavelengths gets diminished as the antenna figure degrades.

Field of view Mainly four different effects will limit the field of view. These are: primary beam; chromatic aberration; time-averaging; and non-coplanar baselines.

Primary Beam: The field of view of the full antenna system is limited by the diffraction-limit of the individual antennas. An approximately the angular field of view is formulated as the full width at half power in arcminutes i.e. $\theta_{PB} = 45/\nu_{GHz}$.

Chromatic Aberration (Bandwidth Smearing): Synthesis imaging is established on the fact that the synthetic beam is strictly valid only for monochromatic radiation. If a bandwidth of radiation frequency is observed, it is actually gridded as if monochromatic. This resulted in aberrations in the image. These effects is parameterized by the product of the fractional bandwidth ($\Delta\nu/\nu_0$) with the source offset in synthesized beamwidths (θ/θ_{HPBW}).

Time-Averaging Loss: The objects that are not located at the phase-tracking center the sampled coherence function or visibility becomes slowly time-variable due to the changing array geometry. Thus averaging of the samples in time will cause a loss of amplitude. Parameterizations of the losses due to time averaging is rather difficult. Observations at $\delta = 90^\circ$ is the only simple case, where the effects are identical to the bandwidth effect except, they operate in the azimuthal, rather than the radial direction. If the averaging interval is taken as Δt_{int} the functional dependence is the same in this case with $\Delta\nu/\nu_0$ replaced by $\omega_e \Delta t_{int}$, where ω_e is the Earth’s angular rotation rate.

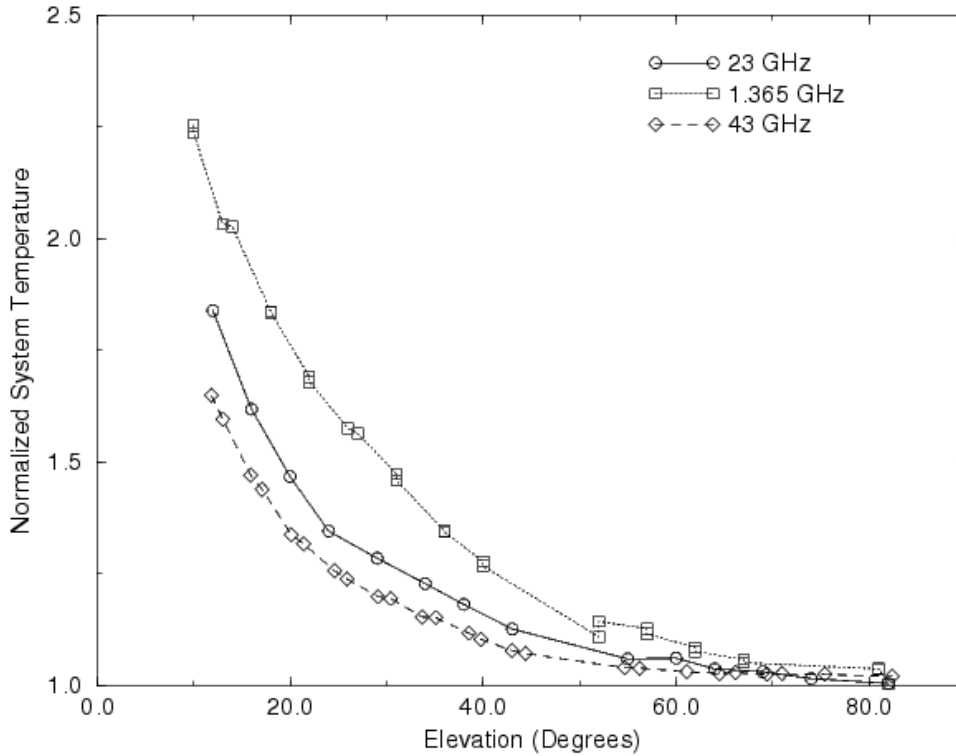


Figure 4.3.: *System Temperature Variations with Elevation at L, K, and Q Bands. The data have been normalized by the system temperature at the zenith - approximately 80K at 43 GHz, 170K at 23 GHz, and 35K at 1365 MHz. The observations were taken in good weather conditions.*

Non-Coplanar Baselines: The basic assumption for producing image with Fourier synthesis imaging method is that the coherence measurements are made in a plane. But all antennas of VLA are not placed over a single array on a plane, exception is only for snapshots. An analysis is done for this problem and it shows that the errors related to the assumption of a planar array increase quadratically with angle from the phase-tracking center. This errors create a serious problem if the product of the angular offset in radians times the angular offset in synthesized beams exceeds unity. The most effected wavelength band is 90 cm and 400 cm. So, only in short baseline arrangements can be used for imaging in these wavelengths. So, only D array of VLA is suitable for such observations. 20 cm observations may also be showing noticeable effect in some instances but shorter wavelengths can used safely.

4.1.4. VLA data analysis

Astronomical Image Processing System (AIPS) is a software package for analyzing the VLA observed data. It is an interactive (and, optionally, batch) software that is used for calibration and editing of radio interferometric data. Fourier synthesis methods are used in this software for the calibration, construction, display and analysis of data and astronomical images. Design and development of the package was started in Charlottesville, Virginia in 1978. It contains over 350 distinct applications i.e. "TASK," and the most of the programme is written in FORTRAN and C languages. AIPS can produce 2D and 3D maps in both

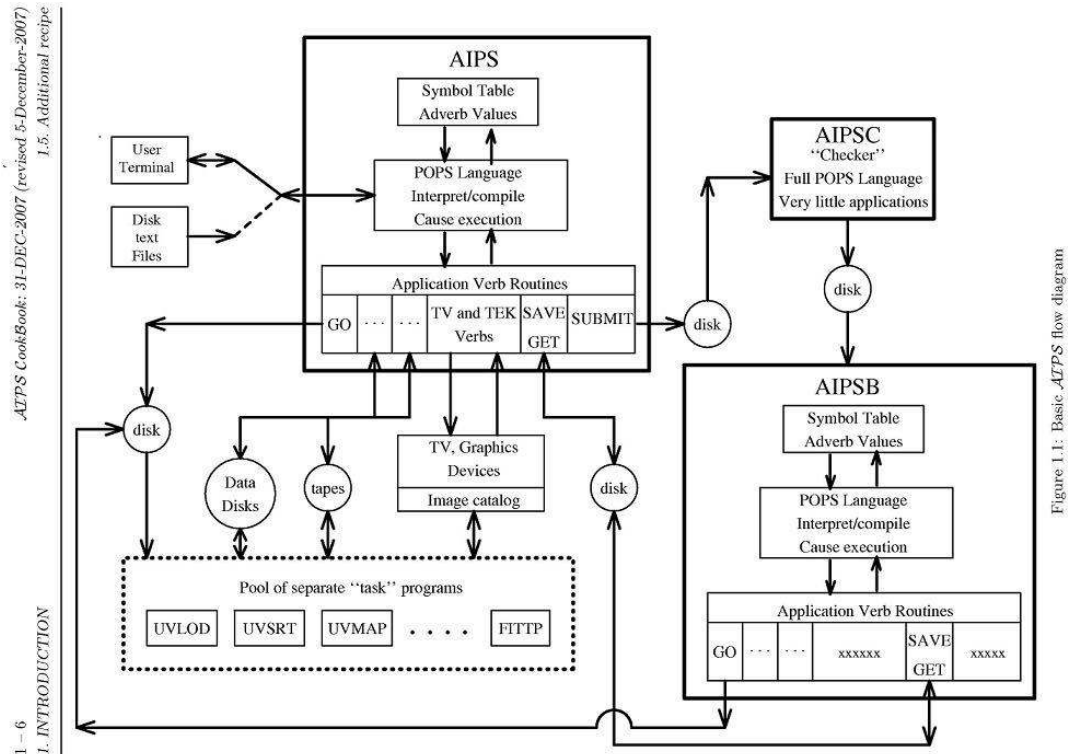


Figure 4.4.: Working method of AIPS in a diagram

the continuum and spectral line observation of VLA. The major steps are: **data loading:** observed data is loaded to the AIPS area as FITS file using the task FITLD or FILLM depending on the stored data format. **Flagging of bad data:** bad data points are removed using the AIPS task UVFLG or WIPER etc. **Calibration of data:** Using the flagged calibrator data, the object amplitude and the phase is calibrated. AIPS task SETJY, CALIB, CLCAL, GETJY are used. **Data are then imaged:** data are then imaged using IMAGR. This was the major steps that has to be performed to get an image from the raw data. Several sub steps are there in between. Image can be self calibrated several times to produce better and better

image. It contains facilities for display and editing of data in the aperture. A basic operation method of AIPS is depicted in a diagram shown in Figure 4.4.

4.2. X-ray astronomy basics and data analysis

4.2.1. Space-borne observations in X-ray astronomy

As total X-ray band is absorbed by Earth's atmosphere, it has no window for Earth-based direct observations. Although the more energetic or hard X-rays having energies more than 30 keV can penetrate a few meter of air, unluckily, the energy range at which the most of the celestial bodies radiate bulk of their energies is far bellow this energy (i.e. 0.5 - 5 keV). Experiments shows that 90% of the photons having energy of 3 keV are absorbed after traveling through just 10cm of air. So, to observe X-rays from the sky, the X-ray detectors must be orbiting above most of the Earth's atmosphere. There are at present three methods of doing so:

- Placing detectors on rocket flights.
- Placing detectors on balloons.
- Satellite based X-ray observation.

For this thesis, satellite-based observations were carried out, and I will describe that only a little bit.

4.2.1.1. Satellite-borne X-ray observatories:

On a satellite that is launched to a certain orbit above the earth atmosphere, the x-ray detectors are placed. This can detect X-rays from all directions and nearly for all the days. The duration of operation in this case is mainly depends on the life time of the satellite. In comparison to the other two methods it has thus better time and sky coverage.

X-ray telescopes: High absorption cross-section of X-rays with matter makes it difficult to image X-rays. Due to its high energy it may also pass through normally used reflectors. So, to the technique of X-ray telescope is radically different from that used in optical telescope. It is seen that if X-ray incident is made at a very low angle only than it bounced of the surface. So, the technique referred as 'grazing incidence' is generally used to collimate the X-rays in to the detector. Data is then recorded electronically which later on reduced and analyzed to convert it to an image. Gold is used as the reflecting material in most of the X-ray telescopes which has a critical reflecting angle of 3.72 degree at 1 keV. Iridium also can be used as X-ray reflecting material for X-ray telescopes. Telescope like Suzaku, XMM and swift used gold, whereas Chandra uses Iridium.

X-ray detectors: There are several types of X-ray detectors, but we will only discuss about the detectors used in our experiments.

- Position-Sensitive Proportional Counter (PSPC) [ROSAT]

X-rays are incident on to the gas filled in the proportional counter. Photo-ionization of the gas then produce the signal that measured to calculate the energy of the incident wave. Energy sensitivity of the counter depends on the absorption cross-section of the gas. Position encoding is done with the anode which is treated as a RC line.

- CCD camera [XMM]

Several types of CCD cameras are used for X-ray observations. Here a brief description is presented for those which are used in XMM-newton telescope. Normally two types of CCD cameras are used, (i) MOS-CCD (ii) pn-CCD. (i) **MOS-CCD:** A three phase frame transfer device MOS EEV CCD22 is used in XMM. It has a high resistivity epitaxial silicon with open-electrode structure. Quantum efficiency of the CCD is very high in the range 0.2 to 10 keV. (ii) **pn-CCD:** Number of generation of electron-hole pairs depends on the energy of the incident X-ray photon. The average energy needed to form an electron-hole pair is 3.7 eV at -90 deg C. The electrons that are formed and kept separated by the applied high bias voltage of the pn-diode used in the pn-CCD are then drifted towards the minimum potential and stored under the transfer register. Which then taken to the readout nodes to count the strength of the incident energy.

4.2.2. Technical details and other specifications of ROSAT

Details of ROSAT telescope²:

4.2.2.1. Overview

ROentgen SATellite or the ROSAT was an X-ray telescope that was developed through a cooperative program between the Germany, United States, and the United Kingdom and then launched by the United states in 1990. It operated for 10 years and was turned off in 1999.

3 solar panels was installed to provide 1 kW of power during Sun-lit parts of the orbit. A rechargeable battery system was installed to provide power during the shadow phase which is about 40 minutes per orbit.

4.2.2.2. Instrumentation

The scientific payload in the satellite consists of two co-aligned scientific experiment setup,

²source:<http://heasarc.gsfc.nasa.gov/docs/rosat/rosdocs.html>

4.2.3 Technical details and other specifications of XMM

- The X-Ray Telescope

Two specific component of the device was operated. They are namely,

- The Position Sensitive Proportional Counter (PSPC)
- The High Resolution Imager (HRI)

and

- The Wide Field Camera

It has a field of view of ~ 2 deg diameter when PSPC is placed at the focal plane. Field of view is reduced to ~ 40 arcmin diameter with HRI in the focal plane.

4.2.2.3. DATA analysis

A pipeline data processing system is designed to handle the scientific data outputs that are produced by the ROSAT. The system is known as the ROSAT standard analysis software system or SASS. The system is able to process automatically the all sky servery data as well as the pointing observations. The processed data can be obtained as the hard copies or as data files which can be further analyzed using the off-line software packages like PROS, EXSAS ASTERIX etc. The data from PSPC and HRI are separately processed with dedicated packages made for them. A third major component of SASS is the one which is used for steering the data processing.

Data from ROSAT is released as the ROSAT Observation Dataset in FITs format. Which is then processed using the EXSAS. The brief description of the process is given bellow.

- Data preparation: Photon events are first selected and binned depending on many criteria e.g. pulse height, time selection etc.
- Instrument correction: Mainly the position dependent instrument response, dead time etc.
- Spectral manipulation is done to remove the background offset, particle background etc.
- Images are then displayed using data presentation software.

4.2.3. Technical details and other specifications of XMM

Details of XMM-newton telescope³:

³source: <http://xmm.vilspa.esa.es/>

4.2.3.1. Overview

X-ray Multi-Mirror Mission (XMM-Newton) was a venture of The European Space Agency's (ESA). The satellite was launched in 1999. The satellite consists of 3 high throughput X-ray telescopes with an unprecedented effective area. Its sensitivity is very high due to its large collecting area and ability to make long uninterrupted exposures.

Scientific proposals are observed and delivered as calibrated data. Data is then reduced and analyzed by the Scientific Analysis System (SAS).

4.2.3.2. Instrumentation

XMM-newton X-ray telescope is mounted on the XMM-newton satellite. Satellite has 4 main component.

- The Focal Plane Assembly (FPA):

The elements of the FPA are: Two reflection grating spectrometry read out cameras are installed; there are PN and Metal Oxide Semiconductor (MOS) imaging detectors which are main part of European Photon Imaging Camera (EPIC).

- The Telescope Tube:

This a long carbon tube which maintains the relative position between the FPA and MSP.

- The Mirror Support Platform (MSP):

This is the section of the satellite which holds mainly the mirror modules and the grating boxes.

- The Service Module (SVM):

SVM consists mainly the subsystems of the satellite which supplies the necessary resources. Solar panel, Sun shield are also a part of it.

Parts of the telescope:

1. Focussing mirrors: XMM-newton consists of three X-ray telescopes. Each of which consists of 58 Wolter I grazing-incidence mirrors and are nested in a coaxial and co-focal configuration. **2. European Photon Imaging Camera (EPIC):**

EPIC consists of two cameras made up of MOS (Metal Oxide Semi-conductor) CCD arrays. The third one is a pn camera which is a pn CCD. MOS cameras are placed behind the gating system to do the spectrometric observation. The other is placed before the unobstructed beam to image directly.

4.2.3.3. **Data analysis**

The Science Analysis System (SAS) is mainly used and designed to reduce the data collected by the XMM-Newton observatory which includes several tasks, scripts and libraries.

XMM-newton data are mainly obtained from two different schemes.

- **Observation Data Files (ODF):** It is re-formatted to FITS format. It gives the un-calibrated chip by chip data.
- **Pipeline Processing System (PPS):** As an output it gives multi wavelength images, cross-correlation products etc.

If the data analysis of an XMM-Newton datasets is started with the PPS products, the SAS is necessary to extract standard (spectra, light curves) and/or customized science products.

5. Observations of the evolution of shocks in a major cluster merger

5.1. Significance of the observations of Abell 3376

Preparing this thesis work, giant ($\sim 2 \text{ Mpc} \times 1.6 \text{ Mpc}$) ring-like non-thermal radio emitting structure were discovered in the outskirts of the southern rich cluster of galaxies Abell 3376 (redshift $z = 0.046$, decl. $\delta \equiv -40^\circ$). These extraordinary structures were originally spotted serendipitously in the NVSS database (see the left panel of Fig. 5.1) and thereafter re-observed with the VLA at 1.4 GHz (20 cm λ) in DnC and CnB arrays and at 4.8 GHz (6 cm λ) in DnC arrays. The observed bow-shock like structure of these giant radio ‘arcs’ and evidence for an ongoing merger mark Abell 3376 as an important site for particle acceleration and for observing the associated non-thermal radiation in radio, X-ray and gamma-rays. We thus also analysed the cluster in X-rays using the archive data from ROSAT and XMM. Optical data are taken from SLOAN digital survey archive. Gamma ray observation could not be done due to the insufficient sensitivity of current Cherenkov telescope arrays, but could be done in the future with the planned Cherenkov Telescope Array.

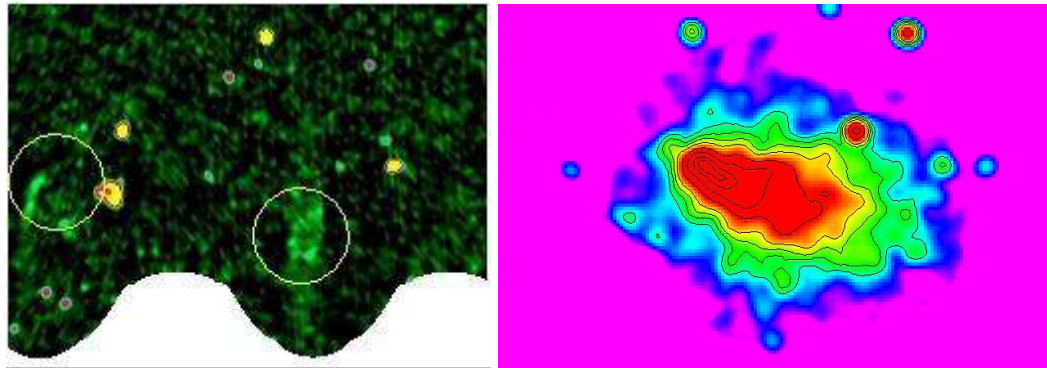


Figure 5.1.: **Panel 1:** NVSS radio image of Abell 3376; **Panel 2:** ROSAT X-ray image of Abell 3376

Abell 3376 is only the second case of clear evidence for an ongoing major cluster merger. Another similar cluster Abell 3667 has been reported in [Rottgering et al. \(1997\)](#)). The cluster is an extraordinary model system to study the effects of energy transfer and structure

5.1 Significance of the observations of Abell 3376

formation during virialization, and this motivated this thesis work and the simulation effort. The following observational details are most relevant for the cluster's unique properties:

- The most interesting feature is a radio emitting, ring-like elliptical structure, containing a pair of giant crescent-like features of ≈ 1 Mpc size, each located at ~ 1 Mpc from the cluster centre. The major axis of these ellipse is aligned with the wake-like extension observed in X-rays. Very likely, these giant radio structures trace the elusive shock waves of cosmological large scale matter flows, which are energetic and large enough to power their radiative output on the Mpc scale (Keshet et al. 2004; Keshet et al. 2003). Moreover, these 'bow shock' like radio sources could be the accelerator sites where MHD shocks are possibly boosting cosmic-ray particles (proton and ions) with energies upto 10^{18} to 10^{20} eV (Kang & Jones 2005)
- We are probably witnessing a unique observational evidence for a merger or accretion (or a mixture of both) shocks near the sparsely studied virial infall region of a massive galaxy cluster. Therefore, these shock fronts are extremely important probes of the gas dynamics at the transition zone between the hot ICM and cold WHIM gas.
- The large scale shocks in the intercluster medium, in association with MHD turbulence are capable of both magnetic field amplification and acceleration of particles to extreme relativistic energies. Gamma rays are also produced due to energy loss of synchrotron, Inverse-Compton and pair production. In view of these high energy processes, Abell 3376 could be an excellent test-bed and an important target for further precise observations with VLA, the gamma-ray mission Fermi-GLAST (after very long integration times) or future ground-based gamma-ray observatories like CTA.
- Abell 3376 shows clear signs of merger activity. The optical galaxies are distributed in a few groups along an embedded filamentary structure. The two brightest clusters of galaxies are located at the centers of two major clumps of galaxies near the ends of this filament (Flin & Krywult 2006), which is aligned with the elongation axis of thermal X-ray emission. X-ray image (see Fig. 5.7) shows disturbed non-symmetric X-ray emission in 0.1-2.4keV band. In the central region, the hot intra cluster medium is highly disturbed and extended like a comet or a bullet head.
- These giant radio structures probe several important components of the cosmic environment: intergalactic gas, magnetic fields and cosmic-rays. They indicate that magnetic fields of appreciable strength are present not only in the ICM but also in the diffuse intergalactic medium, i.e., in the gas that will be shocked as it accretes onto collapsing structures - the precursors of virialized galaxy clusters.
- Finally, Abell 3376 is almost unique in its kind. Abell 3667 is the only object that can be clubbed with Abell 3376 known so far.

5.2. Results

5.2.1. Radio observations and data analysis

The galaxy cluster Abell 3376 is a southern (dec -40 degree) object and was observed with the Very Large Array (VLA) facility of National Radio Astronomy Observatory (NRAO). Its an Y-shaped interferometric array of 30, 25 m diameter radio telescopes located on the plains of San Agustin Socorro, New Mexico, USA. The object was nearly at the critical observing limit of VLA and so the observation was much difficult. Observations at VLA L-band (i.e. $\lambda = 20$ cm) were done on two separate days: on 20th September 2002, in “CnB” configuration for 6 hours in total and on 25th January 2003 in “DnC” configuration observation is done for another 6 hours . As the our source is at far south for the VLA antennas. At this low elevation, beam shape of southern objects in normal configuration (A,B,C or D) takes very bad elliptical shapes. So, using longer arms in North makes the effective beam circular. In hybrid configuration like “CnB” and “DnC” the antennas on the east and west arms are moved in for the shorter configuration (C or D), but those on the north arm remain in extended configuration (B or C)(see VLA observational status summary). So, we used this configurations for mapping our extreme southern object Abell 3376.

Another Radio observation is recently done with VLA in dynamic schedule from 31st May, 2008 to 22nd June 2008 in “CnD” configuration. The observation done in VLA C-band (i.e. $\lambda = 6$ cm) and the total object has been observed with 5 different pointings for about 16 hours to cover the entire two radio arcs found at 20 cm.

20cm data reduction Classic AIPS package is used to reduce the observed VLA data in 20 cm. Producing a radio image of a very faint and extended source is always a challenging job due to the large primary beam area of the antennae which eventually detects many strong sources. Sky curvature for such large beam area never comes very negligible and thus effects the mapping and cleaning of large size fields. In order to reduce this effect we used the task 'IMAGR' to image and for decoloration. IMAGR is used particularly for its ability to clean multi facets which actually permits to map a wide field. I used about 30 small fields (facets) which are centered on strong sources that are located a priori within the field of view centered on each of the three pointings, and then simultaneously cleaned the entire set. Just after the cleaning from the strong sources are done, cleaned components from all the facets are restored back together on to a single field to produce a large wide field image. Quality of the final clean image is quite good due to the use of a separate tangent point for each field, 3-D imaging, and the subtraction of clean components from un-gridded data. In order to emphasize the large-scale features and suppress the oscillations in the side-lobes, During imaging, the visibility data were tapered by a Gaussian that had 30% weight at the $30 k\lambda$ length of the interferometric spacing and parameter ROBUST = 5 was used, corresponding to 'natural' weighting of interferometric visibilities. Circular Gaussian beams of 20" FWHM width is used for restoring the cleaned maps. Using the task DBCON, the calibrated data from two hybrid configurations were combined. This has resulted in

5.2.1 Radio observations and data analysis

better sensitivity and excellent mapping of diffuse large-scale features. It also enhanced the angular resolution needed to identify the superposed background point sources. Phase and amplitude self calibration is done for several times (Pearson & Readhead 1984) to correct for the closure phase and amplitude errors. After removing a few superposed background point sources, the background noise on the final radio images (Fig. 5.3) reaches down to $\sim 30 - 40 \mu\text{Jy/beam}$ of RMS and the S/N ratio for detection of diffuse radio features (shock fronts of the detected arcs) ranges from $\sim 3\sigma$ at the faintest contour to $\sim 25\sigma$ at the peaks. We used the AIPS task PBCOR to correct for the primary beam attenuation effect of individual telescopes and all flux density measurements were done on these corrected images. The corrected flux densities for the east and west radio arc regions are 166 mJy and 136 mJy respectively.

6cm data reduction Observing in 6cm was bit difficult due to its smaller field of view. Our object is $\sim 15'$ in each sides, but VLA field of view in 6 cm is $4.5'$ only. Therefore, we needed mosaicing with 5 pointings on east side and 3 on west, with each pointing separated by $4.5'$ (see Fig. 5.2).

Data from each pointing is reduced separately. Since we are using a hybrid configuration (DnC) in which many of the antennas are recently moved to its new position. We thus have to correct the antenna position using the AIPS task VLANT. Bad data are removed then. Both amplitude and phase calibrator are calibrated successively. Using the IMAGR task, we produced the initial raw image or map. A ROBUST parameter of value 5 was used to enhance the large scale features. Maps are further cleaned and self calibrated to remove the background noise as much as possible. Cleaned component were then restored with circular Gaussian beam of $20''$ FWHM. After doing the primary beam correction with the task PBCOR of each of the pointing, a mosaic image is prepared with the task FLATN. To prepare the spectral index map with VLA 20cm and 6cm data, coordinate, image size, beam size of both the image with tasks IMAGR, REGRD and CONV are used. Images are combined to get the spectral index with the task COMB using the adverb SPIX.

5.2.1.1. Shock structure mapped in the 20cm and 6cm radio bands using the VLA

Using the Very Large Array (VLA) telescope at 1.4-GHz [20cm wavelength] and 4.8 GHz [6cm wavelength] frequency, a large-scale [$\sim 2h^{-1}$ Mpc] ringlike synchrotron radio-emission structure, which traces the intergalactic shocks around the rich cluster of galaxies Abell 3376, at redshift $z = 0.046$ (Smith et al. 2004) has been discovered.

20cm VLA image details Figure 5.3 shows the most important discovery from our 20cm VLA observation. At the outskirts of both sides of a symmetric axis through the cluster a pair of giant, ‘arc’ or ‘bow’ shaped diffuse radio-emitting sources are observed at a projected distance of $\sim 1h^{-1}$ Mpc. Each one has a linear dimension of $\sim \text{Mpc } 1h^{-1}$ and an extension of $\sim 200 \text{ kpc } h^{-1}$. Radio data from two pointings and configurations (VLA CnB and DnC

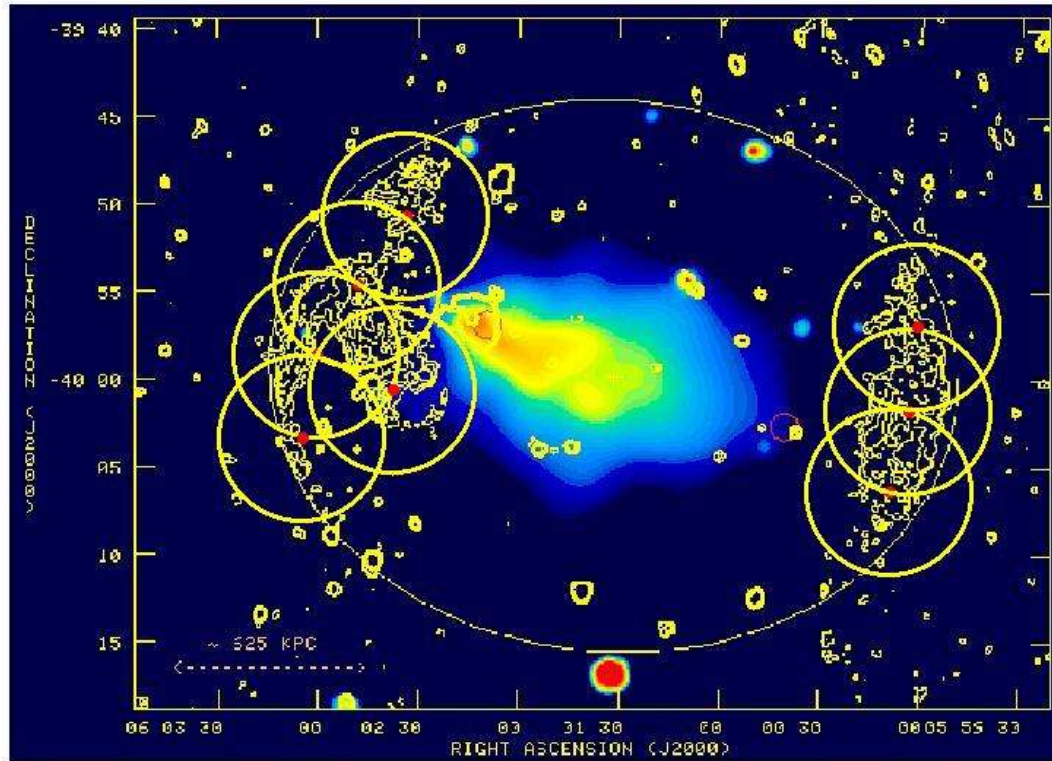


Figure 5.2.: Several pointings of VLA observation. Original image is taken from [Bagchi et al. \(2006\)](#). Reprinted with permission from AAAS.

hybrid configurations) are combined to produce the image of the whole cluster. By combining the map and cleaning it properly, sensitivity is enhanced to map the diffuse, large-scale emissions, as well as the angular resolution (~ 20 arc sec) is increased for identifying the superposed background point sources. The VLA radio image shown in the Fig 5.3 has ~ 40 micro Jansky (μJy) per beam of root mean square noise background. The estimated signal-to-noise ratio for detection of these structures ranges from $\sim 3\sigma$ at the faintest contour to $\sim 25\sigma$ at the peaks. Superimposed background point sources that are visible in Fig. 5.3 are first removed to do the actual calculations. Noticeably, both radio structures are positioned nearly symmetrically with their concave side facing towards the cluster center. They fit quite well on the surface of a large, projected elliptical ring-like formation of dimension ~ 2 Mpc by 1.6 Mpc as if a projection of an ellipsoidal surface, and is oriented in position angle of 85° (see Fig. 1.1; [Bagchi et al. 2006](#)). The center of this ellipse falls at the position right ascension. 06h 01m 32s, and declination of $-39^\circ 59' 50''$, which is taken as the center of symmetry of this cluster. No central "radio halo" type of diffuse, large-scale emission was found at the surface brightness limit mentioned above.

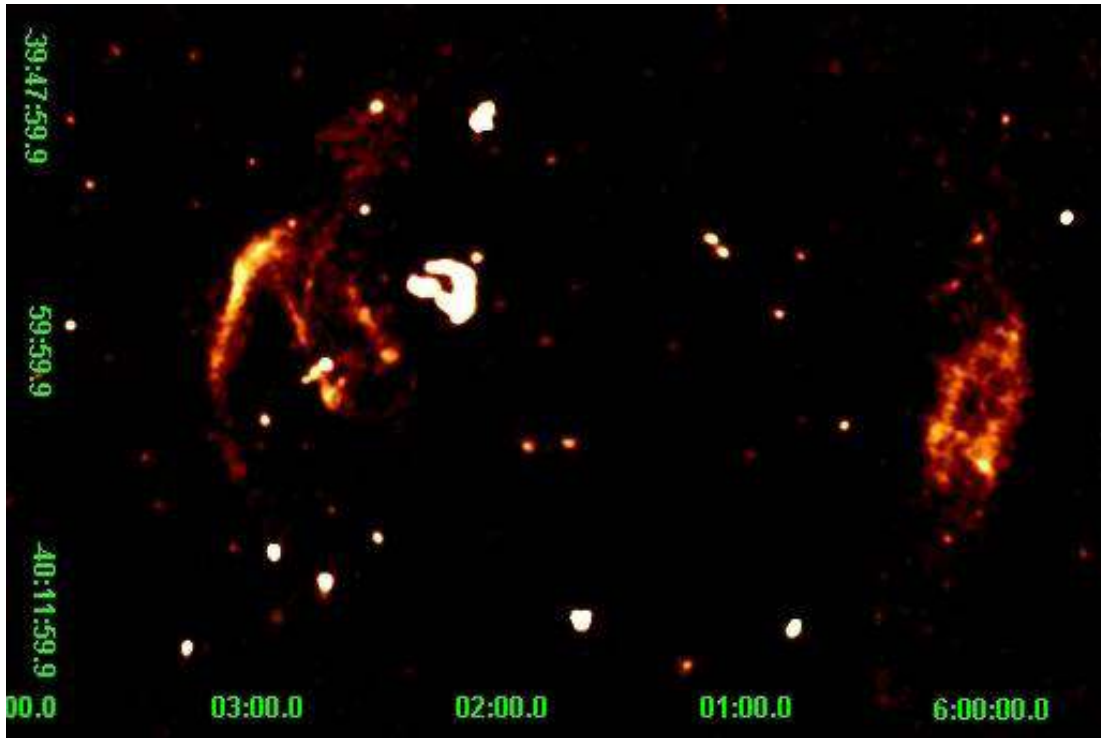


Figure 5.3.: *Mosaic VLA image of Abell 3376 at 20cm*

6cm VLA image details Fig. 5.4 i.e. the 6cm VLA image of Abell 3376 nearly reproduces the 20cm image (Fig. 5.3) morphologically, though, due to insufficient observation time from VLA dynamic scheduling, some faint parts of the radio arcs couldn't be imaged. Though both of the arcs are traced nicely, in 6 cm observation the west arc is seen as a double arc instead of a torus shaped radio source of 20 cm observation. Insufficient time of observation made it impossible to observe the faint radiation of the upper part (above the notch as at 20 cm) of the east arc. Fig. 5.4 has root mean square noise background of ~ 25 (μJy) per beam, and the estimated signal-to-noise ratio for detection of these giant radio arcs ranges from $\sim 1.5\sigma$ at the faintest contour to $\sim 15\sigma$ at the peaks.

5.2.1.2. Spectral index of the radio structures

merger/accretion problem The observation and analysis of Abell 3376 was done in the optical (data taken directly from SLOAN digital survey), X-ray (archival ROSAT and XMM data) and 20cm Radio waves (VLA) in the first phase. Though a clear sign of an energetic event is found in the cluster in X-rays, it is quite difficult to interpret the origin of the bow shock like structure. The reason is simple because such shocks may arise both from

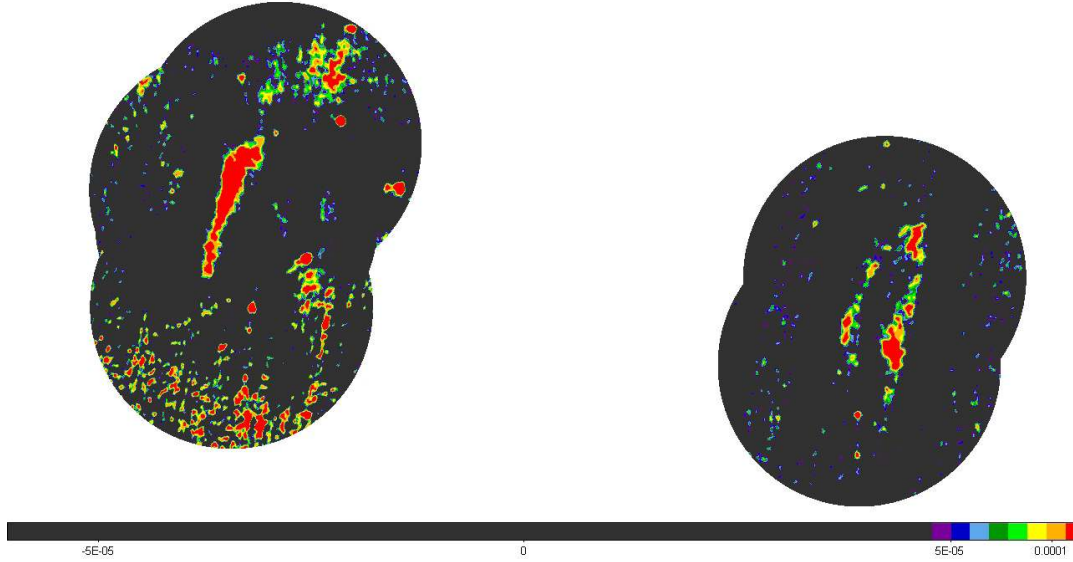


Figure 5.4.: Mosaic VLA image of Abell 3376 in 6 cm

a merging cluster or at the periphery of a big cluster as an accretion shock. Determination of Mach number of the shock or the spectral index of the radio structure can lead us to the solution. Spectral index mapping is the most important to confirm the physical process involved behind the creation of such large structure and will help us to predict the possible high energy gamma ray emission from the site. According to [Miniati et al. \(2000b\)](#) Mach number of < 5 is definitely a merger shock and Mach number > 10 is a accretion shock. So, from the calculations of DSA, a clear constraint on accretion and merger process can be drawn from the relation of Mach number and Radio Spectral Index of shock fronts can be calculated for such radio structures. Our calculation from diffusive shock acceleration thus clearly indicates that spectral index of $0.58 < \alpha < 0.52$ corresponds directly to merger or accretion shock respectively (see the Plot 5.5).

We combined our earlier 20cm VLA data of Abell 3376 with recent VLA data of 6cm. A detailed radio spectral index map is prepared which clearly indicates a major merger event in the studied cluster. An average range in spectral index of 0.95 to 1.05 is noted. A region of about $200 \text{ kpc } h^{-1}$ is noticed behind the shock front where nearly no sign of change in spectral index is found (see Fig. 5.6).

5.2.1.3. Estimation of magnetic field

To obtain the minimum-energy magnetic field B_{\min} , I minimized the total nonthermal energy density (u_{\min}), which consists of the magnetic-field energy and the energy contained in all relativistic particles. Specifically, $B_{\min} \propto (1 + k)^{2/7} (\phi V)^{-2/7} L_{\text{syn}}^{2/7}$. In this expression, the model parameters are as follows: k , the ratio of energy in heavy particles to electrons; f , the

5.2.2 X-ray observation and data analysis

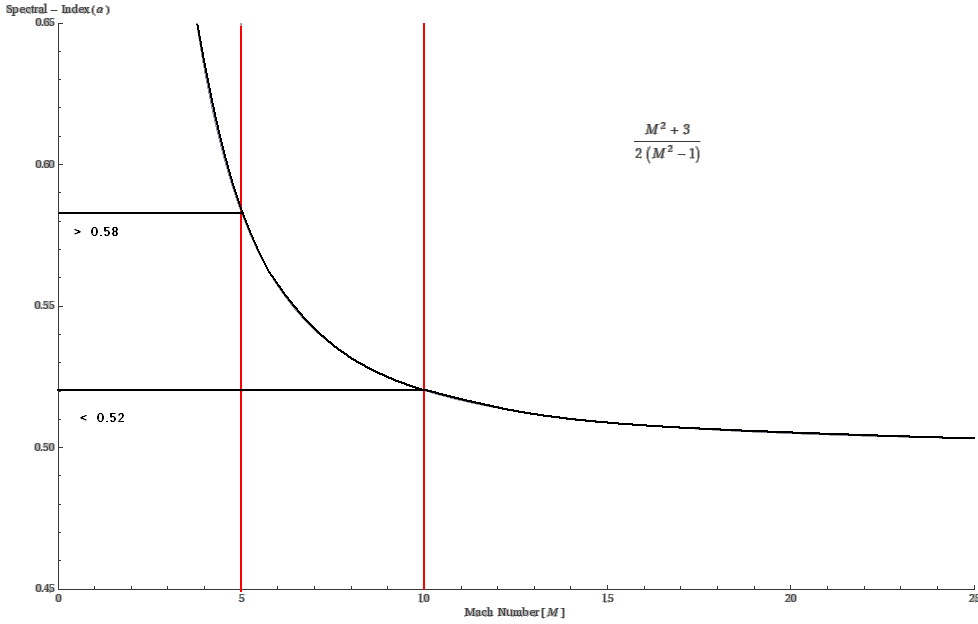


Figure 5.5.: Spectral index vs Mach number

fraction of the source volume filled by magnetic fields; and V , the total source volume. The total synchrotron radio luminosity, L_{syn} , can be obtained from observations by integrating the radio spectrum between lowest and highest frequencies (we used 10 MHz to 100 GHz). Parameters K , f , and V are usually unknown and need to be guessed reasonably. For my estimate of B_{min} , I used the values within range: $K = 1$ to 100, $f = 0.1$ to 1, line-of-sight depth = 270 kpc (for calculating V), and spectral index $a = 0.5$ (for obtaining L_{syn}). For further details, see (31). My estimation using the observed flux density and spectral index gives an estimated range for magnetic field of 0.6 to 2.2 μG in the radio arcs of cluster Abell 3376.

5.2.2. X-ray observation and data analysis

X-ray data of the ROSAT (Roentgen Satellite) PSPC-B (PSPC: Position Sensitive Proportional Counter detector) of Abell 3376 were taken from the High Energy Astrophysics Science Archive Research Center (HEASARC). The observation was done with a 11.7 ks exposure time on February 28, 1992. An image in the $[0.14\text{--}2.0]$ keV band with 16 arcsec pixels or a spatial resolution of 25 arcsec is made from the photon list file.

In addition, data were retrieved from the XMM-Newton archive a 47.2 ks observation performed on April 01, 2003 in standard Full Frame mode (Observation ID: 0151900101, Proposal no.: 15190). The pointing center of the telescope was on the position R.A. 06h

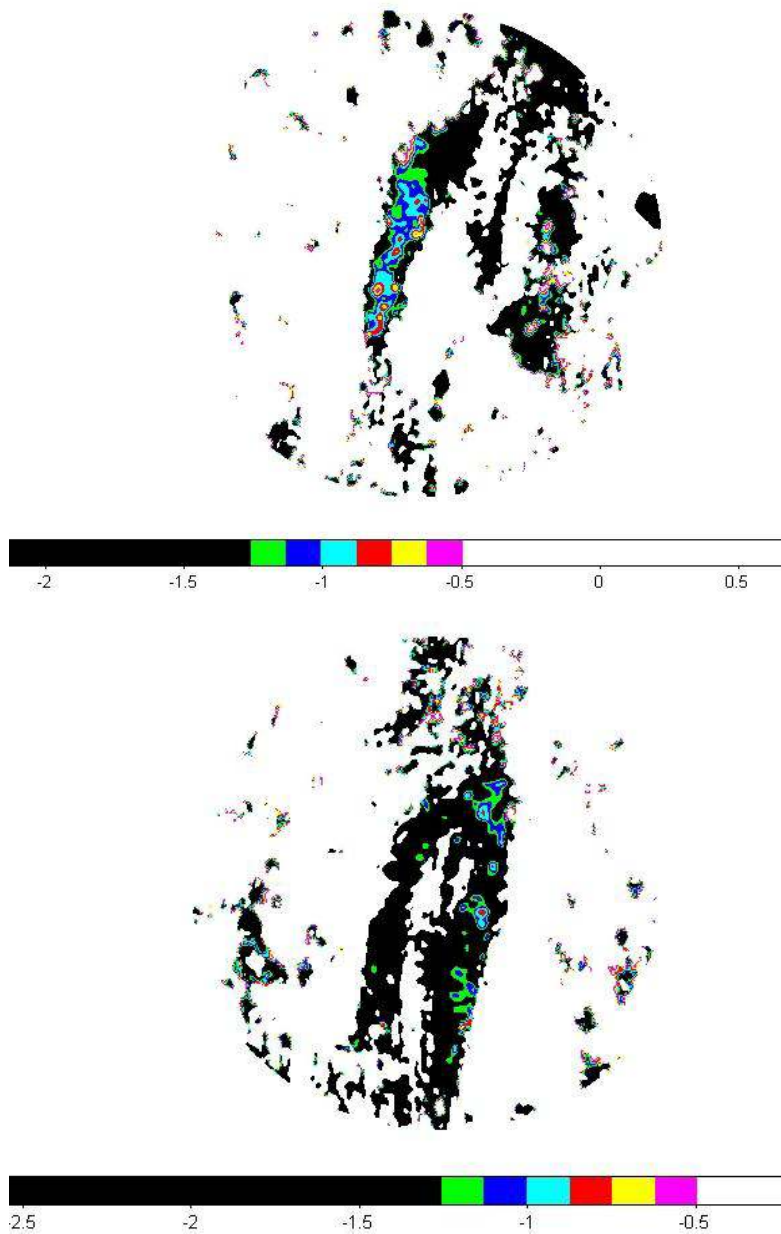


Figure 5.6.: *Spectral index of East and West radio arc of Abell 3376. 20cm and 6cm VLA data are combined to produce this spectral index map*

02m 8.6s, and Dec. $-39^{\circ}57'18.0''$ (J2000). With the XMM Science Analysis Software (SAS) V6.0 the basic data processing i.e. the "pipeline" removal of bad pixels, electronic noise and

correction for charge transfer losses etc. were done. For the spectral analysis, the observations made with the EPIC/MOS1, MOS2 and PN cameras were used. For the EPIC/MOS cameras, after applying the standard filtering, keeping only events with FLAG = 0 and PATTERN ≤ 12 , observation times with flares are removed using the light-curve in the [10-12 keV] band using a 3-sigma clipping technique. The cleaned MOS1 and MOS2 event files have remaining exposure times of 19.3 ks and 19.7 ks, respectively. Similar procedure for the PN is used, applying the standard filtering and keeping only events with FLAG = 0 and PATTERN . 4. The cleaned PN event file has a useful exposure time of 19.2 s. We created the redistribution and ancillary files (RMF and ARF) with the SAS tasks rmfgen and arfgen for each camera and each region that is analysed. We extracted the Xray spectrum in an ellipse centered on the X-ray peak with a semi-major axis of 440 arcsec and semi-minor axis of 390 arcsec to obtain the mean temperature and metallicity of the cluster. The spectral fits were done with data in the range [0.3-8.0 keV], simultaneously with MOS1, MOS2, and pn. Spectral fits were done on the background corrected data. Standard background obtained at the XMM science center, created by adding sky exposures of intermediate galactic latitude without bright sources is used for this analysis. Region that is selected for spectral fits, the mean emission-weighted temperature is $kT = 4.1 \pm 0.3$ keV.

5.2.2.1. ROSAT X-ray image of Abell 3376 in 0.14 to 2.0 keV X-ray band

The luminous thermal bremsstrahlung X-ray emission is mapped (see Fig. 5.7¹) using the data obtained from the Position Sensitive Proportional Counter (PSPC) detector onboard the Roentgen Satellite (ROSAT). The observed band is 0.14- to 2.0-keV. It reveals a highly disturbed, thermodynamical non equilibrium state of the ICM at the central region of the cluster. A ‘comet’ or ‘bullet-head’ like X-ray structure is seen along the major axis of the ellipsoidal radio structure. Radio structures are located at the outer periphery of the X-ray emission. A clear filamentary structure that consists at least three subclusters are found along the elongation of the X-ray emission mapped by ROSAT and XMM-Newton telescope (Escalera et al. 1994; Flin & Krywult 2006).

5.2.2.2. XMM X-ray image in 0.3 to 8.0 keV X-ray band

A strong evidence of merger activity in the cluster Abell 3376 along the filamentary axis (as perviously mentioned) is clearly seen in the XMM-Newton and ROSAT X-ray maps (see Fig. 5.8 and 5.7²). Both the ROSAT and the XMM maps are quite similar in morphology, but due to higher resolution of XMM it reveals more substructures. A clear ‘bullet-head’ and multiple X-ray peaks each of which are associated with a merging group are detected at the southwest of the bullet structure. X-ray temperature calculated from XMM observation

¹Data analysis is done by my collaborators F. Durret of Institut d’Astrophysique de Paris, France and G. B. Lima Nato of University of Sao Paulo, Brazil

²Data analysis is done by my collaborators F. Durret of Institut d’Astrophysique de Paris, France and G. B. Lima Nato of University of Sao Paulo, Brazil

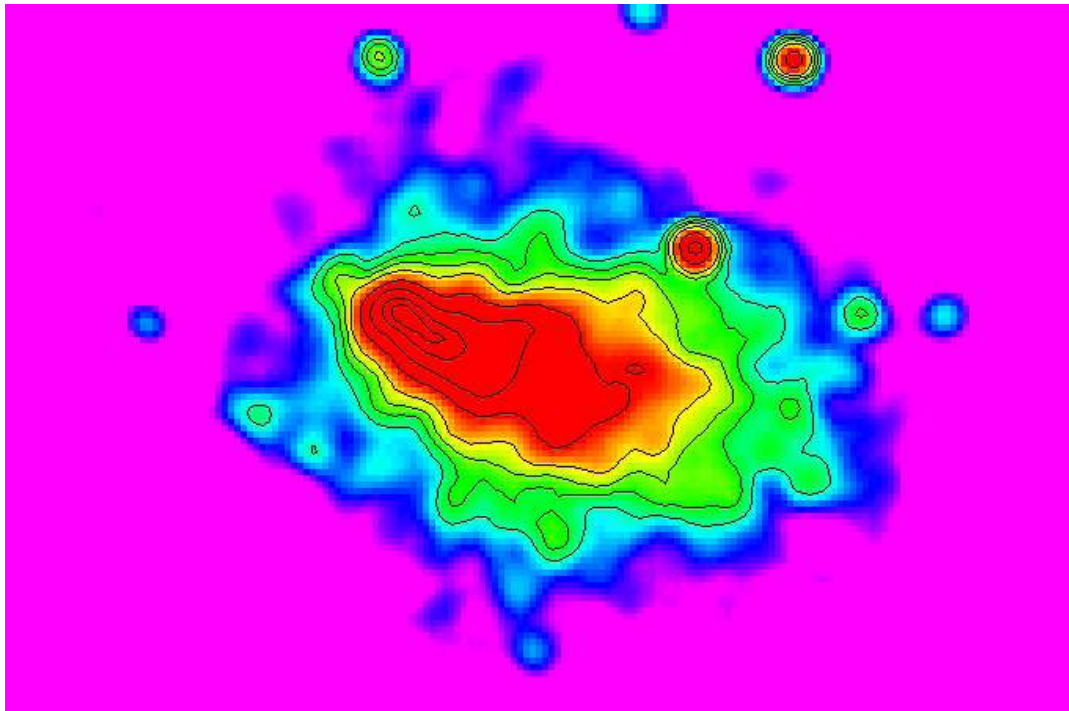


Figure 5.7.: *ROSAT X-ray image of Abell 3376*

shows an average cluster temperature about 5 keV (5.8×10^7 K), with several alternating hot and cold regions crossing the cluster, divided by a prominent “cold-arc” at about 3 keV, which originates at the north edge and curves southward toward the east. The error calculated for this temperature estimation is about 10%.

5.3. Interpretation of the results

There is not very certain models to explain the synchrotron emission from the radio structures at \sim Mpc distances from the cluster periphery. So, with some logical arguments we can find out some possible reasons. Radio emission from cluster periphery certainly requires some form of in situ acceleration mechanism for particles and the turbulent magnetic field to scattering them to have synchrotron radiation. Superposition of background radio point sources, which are very few (~ 0.02 sources per arc min² above 1-mJy flux density) cannot generate such a huge structure, and also most of the emission seen is truly diffuse. Lastly, these diffuse sources cannot be the radio lobes of a currently active giant radio galaxy (GRG) or from FR II radio galaxies, because up to ≈ 0.2 mJy/beam surface brightness limit ($\approx 5 \sigma$ signal) no radio jets or plumes connect the radio sources with any central optical galaxy. It is also very uncommon to have GRGs of such extreme size (~ 2 Mpc) (Schoenmakers et al.

5.3.1 Merger shock

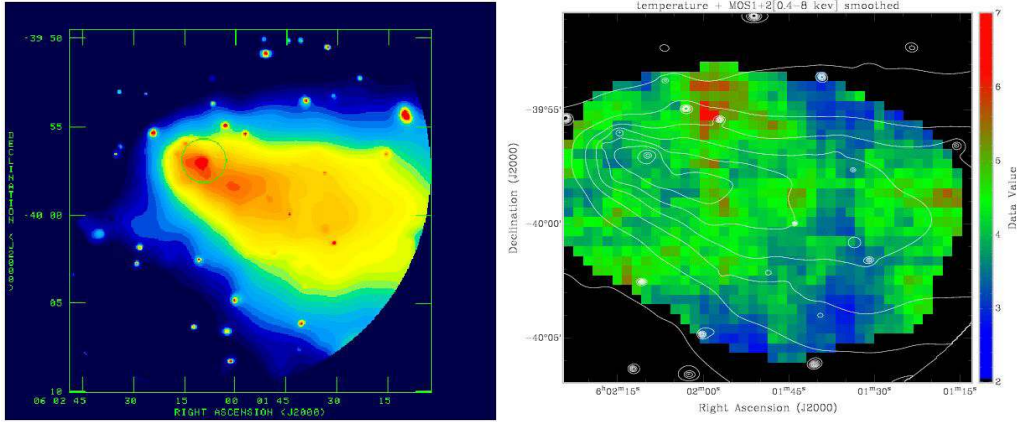


Figure 5.8.: **Panel1:**XMM X-ray image of Abell 3376; **Panel2:**Temperature map of Abell3376 derived from XMM X-ray data

2001). Possibility of Giant FR II galaxies is ruled out by our estimated equipartition magnetic field strength (see section 5.2.1.3). On the other hand, symmetric structure of the radio arc found, have concave bow-shock like shape, they are formed tangentially to both the chain of sub-clusters of galaxies and to the x-ray emission elongation axis (Fig. 1.1). So, they are definitely associated to the cluster and only a cosmological-scale energetic event (merger or accretion) can be the reason for generation of such a big structure.

Hydrodynamical simulations also support the above logic. They show that only shock waves induced in the structure-formation processes are sufficiently energetic, extended, long-lived to overcome the strong radiation losses of the relativistic electrons over a Mpc scale. Shocks can rapidly accelerating the particles to the relativistic energies (Miniati 2003;Keshet et al. 2003), which could emit synchrotron radio emission at the level observed (Keshet et al. 2004). A detailed discussion and explanation for such phenomena will be done in the discussion chapter of this thesis (see 8).

5.3.1. Merger shock

The extended steep-spectrum radio arcs and elongated x-ray structure found in a well-studied cluster Abell 3667 was adequately explained by the merger shock model (Roettiger et al. 1999). So, this could be a possible explanation for the structure observed in the cluster Abell 3376 too, as it resemble with the cluster Abell 3667. They have similar x-ray and radio morphologies (Rottgering et al. 1997) and spectral index analysis as explained above (see the image 5.6) shows nearly the same steep-spectrum as seen in Abell 3667 (Roettiger et al. 1999). These shocks takes $\sim 10^9$ years for shock fronts to cross the ~ 1 Mpc distance from the cluster center, if the shock speed is $V_s = 10^3$ km/s. The peripheral location of ring-like

radio arcs or ‘radio gischt’ and the absence of a central radio halo in Abell 3376 agree with simulations of merger shocks (Hoeft et al. 2004). So, its quite evident that the radio structure at the outskirts of these cluster are generated from the synchrotron radiation of the particles that the accelerated by the shocks and it is quite possible that the DSA is one of the main accelerating process working there as explained in the section 2.3.3.4.

The spectral index calculated by combining 20cm and 6cm data revealed another aspect of the observed radio structure. An extended region of 100’s of kilo parsecs behind the shock has nearly no change in spectral index. If the radio structures seen in the cluster Abell 3376 would have been generated by Fermi-I acceleration of charge particles at the shock alone, a sharp structure at the shock front would expected. The structures are found at a large distance from the centre of the cluster which indicates a giga year evolution time for the shocks. On the contrary, the synchrotron loss time of the radio-emitting electrons is much less than the shock evolution time ($\sim 10^8$ year). Thus, the observation of synchrotron radiation across the extended region without signs of a spectral index gradient, certainly gives an indication of possible re-acceleration of the particles behind the shock.

5.3.1 Merger shock

.

6. Hydrodynamical simulation

In my thesis work, I used the ENZO cosmology (hydrodynamic) code (O’Shea et al. 2005) for all the simulations that has been performed in this project. Enzo is a block-structured Adaptive Mesh Refinement (AMR) (Berger & Colella 1989) grid based code. Eulerian hydrodynamics method is coupled with an N-body particle mesh (PM) solver (Efstathiou et al. 1985; Hockney & Eastwood 1988) in this code to describe the gas dynamics, and to follow the dark matter component respectively. The Poisson equation that comes in the context of N-body dynamics is solved using a combination of fast fourier transform (on a periodic root grid) and multigrid techniques (on non-periodic subgrids). Euler’s equations of hydrodynamics are solved using a modified version of the piecewise parabolic method.

6.1. Dark matter and gas dynamics

As the dark matter accounts for atleast $\sim 83\%$ of the total matter in this universe, the dynamics of large-scale structures are dominated by “dark matter” only, but only way they can interact or influence baryons is the gravitational interaction. Baryon gas though evolves in the influence of dark matter gravitation, self interaction is rather complicated. Baryon self interaction is governed by thermodynamics, acceleration of particles, loss of energy through various process like cooling, radiation etc. etc. But gravitation is the only interaction that acts on both among the dark matter and baryons. There are many astrophysical situations where gravitational physics becomes most important. Such as, galaxy or galaxy cluster collisions, where the gas particles in the two galaxies or clusters of galaxies tend to interact in a collisionless manner. Thus, in such a case both dark matter N-body dynamics and gas dynamics should be incorporated properly.

6.1.1. N-body dynamics

Interaction of a N particle system is defined by a $6N + 1$ dimensional phase space, where, position and velocity of each particle is defined by 3+3 cartesian position and velocity vectors at each time t . The solution of the N-body problem defines a trajectory that lies in this phase space. A statistical description of the problem is possible if the number of particles is large enough, i.e. the situation where the two body relaxation time is long compared to the time-frame one is interested in. A mean field description of the dynamical system is deduced in terms of a single particle distribution function and is called the collisionless Boltzmann equation. This allows us to pass from a $6N + 1$ to a $6+1$ dimension phase space. The idea

is to construct a mean field description of the dynamical system in terms of a single particle distribution function $f(\mathbf{x}, \mathbf{v}, t)$, where $f(\mathbf{x}, \mathbf{v}, t)d^3x d^3v$ is proportional to the probability of finding a particle in a 6D element of volume $d^3x d^3v$ centered around position \mathbf{r} and velocity \mathbf{v} at time t . The distribution function uniquely defines all the properties of the total system. The Boltzman equation is thus derived as

$$\frac{\partial f}{\partial t} + \mathbf{v} \cdot \frac{\partial f}{\partial \mathbf{x}} - \nabla \Phi \cdot \frac{\partial f}{\partial \mathbf{v}} = 0 \quad (6.1)$$

Where, where $\Phi(r, t)$ is the gravitational potential. The above equation is also referred as Vlassov equation in many literature.

6.1.2. Gas dynamics or hydrodynamics

In most general manner fluid flow can be described by the Naiver-Stokes equations ([Landau & Lifshitz 1959](#), [HIRSCH 1988](#)). A full system of Naiver-Stokes equations is actually expressed by the conservation of the three basic flow quantities namely density ρ , momentum $\rho \mathbf{u}$ and energy E . i.e.

$$\frac{\partial \rho}{\partial t} + \nabla \cdot (\rho \mathbf{u}) = 0 \quad (6.2)$$

$$\frac{\partial \rho}{\partial t} \mathbf{u} + \nabla \cdot (\rho \mathbf{u} \otimes \mathbf{u}) + p \mathbf{I} - \tau = \rho f_e \quad (6.3)$$

$$\rho \frac{\partial E}{\partial t} + \nabla \cdot (\rho \mathbf{u} H - k \nabla T - \tau \cdot \mathbf{u}) = W_f + q_H \quad (6.4)$$

Where, \mathbf{I} expresses the isotropic pressure component, f_e gives the internal forces, H is representing the enthalpy of the system, heat conduction is given by $-k \nabla T$, $E = e^{1/2} \rho (u^2 + v^2 + w^2)$ is the total energy per unit volume, with e is the internal energy per unit mass for the fluid, p is the pressure, W_f and q_H are the work of external volume and heat sources (radiation, chemical reaction etc.) respectively.

In simplest case the dynamics of ideal fluid can be described by the basic equations of hydrodynamics. Which is nothing but the conservation equations of mass, momentum and energy. Such system is thus can be described by the Euler's equations of fluid dynamics. The Euler equations govern inviscid flow. They thus correspond to the Navier-Stokes equations with zero viscosity and heat conduction terms.

6.1.2.1. The Euler equations

As I already stated that the assumption here is to describe our problem in a simplistic manner, we ignore the dissipative effects like molecular diffusion, heat conduction or fluid viscosity. The dynamics of the fluid thus can be expressed by the Euler equations, which can be deduced from the above set of Naiver-Stokes equation ignoring all the dissipative terms.

$$\frac{\partial \rho}{\partial t} + \nabla \cdot (\rho \mathbf{u}) = 0 \quad (6.5)$$

$$\frac{\partial \rho}{\partial t} \mathbf{u} + \nabla \cdot (\mathbf{u} \otimes (\rho \mathbf{u})) + \nabla p = 0 \quad (6.6)$$

$$\rho \frac{\partial E}{\partial t} + \rho \nabla \cdot (\mathbf{u} H) = 0 \quad (6.7)$$

6.1.2.2. Turbulence in hydrodynamic equation

In some certain physical conditions the stability of a steady flow may be disrupted and a small perturbation can grow significantly over time to produce unstable, turbulent motion. Stability of any flow depends on the value of the dimensionless Reynolds number. Reynolds number corresponds to the ratio of the strength of the nonlinear effects and the strength of the linear viscous effects at the macroscopic level. So, for a characteristic velocity, U , and a characteristic length scale, L , of the flow one defines the Reynolds number as

$$Re = \frac{(UL)}{\nu} \quad (6.8)$$

where, $\nu = \mu/\rho$ is the kinematic viscosity. A critical value, Re_{crit} , can be found depending on the system above which (i.e. when $Re > Re_{crit}$) the flow turn in to a chaotic system.

Turbulent flow is induced at a larger scale and then transferred to the smaller scale eddies. At every length scale there an equilibrium of energy flow exists i.e. what is entering from the higher length scale is flowing out to the next lower length scale. The removal of energy from one length scale i.e. the apparent energy dissipation is comes due to the non-linear terms of the Navier-Stokes equations. So the energy dissipation rate is calculated as

$$\epsilon = \nu \kappa_0^3 |\nabla \mathbf{u}(\mathbf{x}, t)|^2 \quad (6.9)$$

Rate of transfer of turbulent energy ϵ at a length scale ℓ is thus calculated by some dimensional analysis. Considering a natural time scale τ and speed u we get, $\epsilon = \ell^2/\tau^3$ and $u = \ell/\tau$. i.e.

$$\epsilon = u^3/\ell \quad (6.10)$$

The distribution of kinetic energy over the different length scales is a fundamental characteristics of a turbulent flow. In such a system the energy density at a given length scale or wave-number κ is only depends on the energy dissipation rate ϵ and wave-number κ itself and the energy spectrum function is expressed by $E(\kappa)$. By dimensional analysis, the only possible form for the energy spectrum function according to the third Kolmogorov's hypothesis is

$$E(k) = C \epsilon^{2/3} k^{-5/3} \quad (6.11)$$

Kolmogorov energy spectrum can be studied in momentum space as it deals with the wave number. A turbulent velocity field in normal space is thus derived from the velocity increments. i.e.

$$\delta\mathbf{u}(\ell) = \mathbf{u}(\mathbf{x} + \ell) - \mathbf{u}(\mathbf{x})$$

Here the velocity increments scales with the spatial difference of the measuring points. Doing statistical averaging the velocity over several such points and there distances, a power law relation is found similar to that of the Kolmogorov power law. This relation is known as the structure function in turbulence. The relation reads as

$$\langle [\delta\mathbf{u}(\ell)]^n \rangle = C_n \varepsilon^{n/3} \ell^{n/3} \quad (6.12)$$

Where, C_n is a universal constant and n is the order of the structure function. A simple relation between the Kolmogorov spectra and the structure function is drawn. If p is considered as the slope of the Kolmogorov spectrum n is related as $n/3 = p - 1$.

6.1.2.3. Shock waves

Shock is a condition where discontinuities in equation occur in physical flow quantities like density, velocity, pressure, entropy etc. General solutions for the Euler equations which are nonlinear hyperbolic are the wave equations. Shock is operated at a point where the solution for the equations become multi-valued and the basic assumptions for the equation breaks down. To get the shock waves in Eulerian equations, weak solutions are formulated by introducing the Rankine-Hugoniot shock conditions in its integral form.

6.2. Numerical implementation of N-body and gas dynamics in ENZO

6.2.1. Solution for N-body dynamics

Though in some simulation codes direct solution of Boltzmann equation is used to calculate the N-body dynamics, due to the high dimensionality of this system a direct solution through numerical schemes becomes much costlier in respect to time and space. Essentially thus a cost effective simple method called N-body approach is used for ENZO-AMR simulations. In this method trajectory is calculated for a representative sample of individual particles. A simple set of coupled equation is thus constructed to calculate the trajectory of the representative sample (Equation 6.13 and 6.14). We assumed the representative particle position at certain time t as \mathbf{x} and the particle velocity as \mathbf{v} . The coupled equation is thus written as

$$\frac{d\mathbf{x}}{dt} = \mathbf{v} \quad (6.13)$$

$$\frac{d\mathbf{v}}{dt} = -\Delta\phi \quad (6.14)$$

$-\Delta\phi$ describes the gravitational force term in the equation 6.14. A solution to these equations can be found by solving the elliptic Poisson's equation.

$$\Delta^2\phi = 4\pi G \quad (6.15)$$

where ρ is taken to be the density of both the collisional fluid (baryon gas) and the collisionless fluid (particles representing dark matter).

The aforementioned equations are finite-differenced. Similar to hydrodynamical equations, it is solved with same time steps for simplification of the problem. Triangular shaped cloud interpolation technique is used to spatially discretized the density field of the dark matter particles on the grids. Using Fast Fourier Transformation (FFT) the elliptic Poisson equation is solved. The forces thus calculated on the mesh are first interpolated to the particle positions and the velocity of the respective particles then updated (O'Shea et al. 2005).

6.2.2. Solution for gas dynamics

ENZO is mainly a code written for handling the cosmological problems. Component that deals with only baryonic gas dynamics is mainly solved using Piecewise parabolic method (PPM) which was originally developed by Woodward & Colella (1984). This is thus the primary scheme for handling the hydrodynamics in ENZO. The method was significantly modified for making the code suitable for mainly cosmological problems (Bryan et al. 1995).

PPM is one of the most accurate among the shock capturing methods developed yet. Its a higher-order accurate version of Godunov's method. The scheme includes an accurate piecewise parabolic monotonic interpolation to third order in space. Shock is captured using a nonlinear Riemann solver. It is normally expected that the solution will show some oscillatory nature after a shock is passed. In PPM method a special selective filtering is introduced to fast damping of this oscillation in the solution. So, it does an excellent job capturing strong shocks and outflows. A scheme that is accurate upto second order in space and time is applied to build the directional splitting in multi-dimension. This method explicitly conserves the energy, mass and momentum which are written in coordinate for a Friedman-Robertson-Walker (FRW) space-time. Modification is done to include the gravity in both the Riemann solver and conservation laws that are described in the section 6.1.1. Thus PPM is especially superior for modeling cosmological flows (Bryan et al. 1995).

In many astrophysical problems, bulk hypersonic motion of gas can increase the kinetic energy of the fluid to such extent that it dominates the internal energy to extremely high orders. This may create significant inaccuracy in the calculation of pressure, temperatures of the baryon gas. This actually happens due to the limitations of the machine precision. This problem is handled by solving them separately in ENZO code (O'Shea et al. 2005).

6.3. Adaptive mesh refinement (AMR) in ENZO

Adaptively refined grids are stacked over the initial static grid in AMR. A sequence of coarser to finer rectangular meshes are nested on which the partial differential equation (pde) is discretized. Continuous domain of interest is actually discretized into grid of many individual elements. To insert an initial higher resolution in a subvolume of the simulation, ENZO allows one to put a static nested sub-grids at any user specified region. Refinement (AMR) can occur anywhere within the simulation volume or within the sub-volume specified by the user.

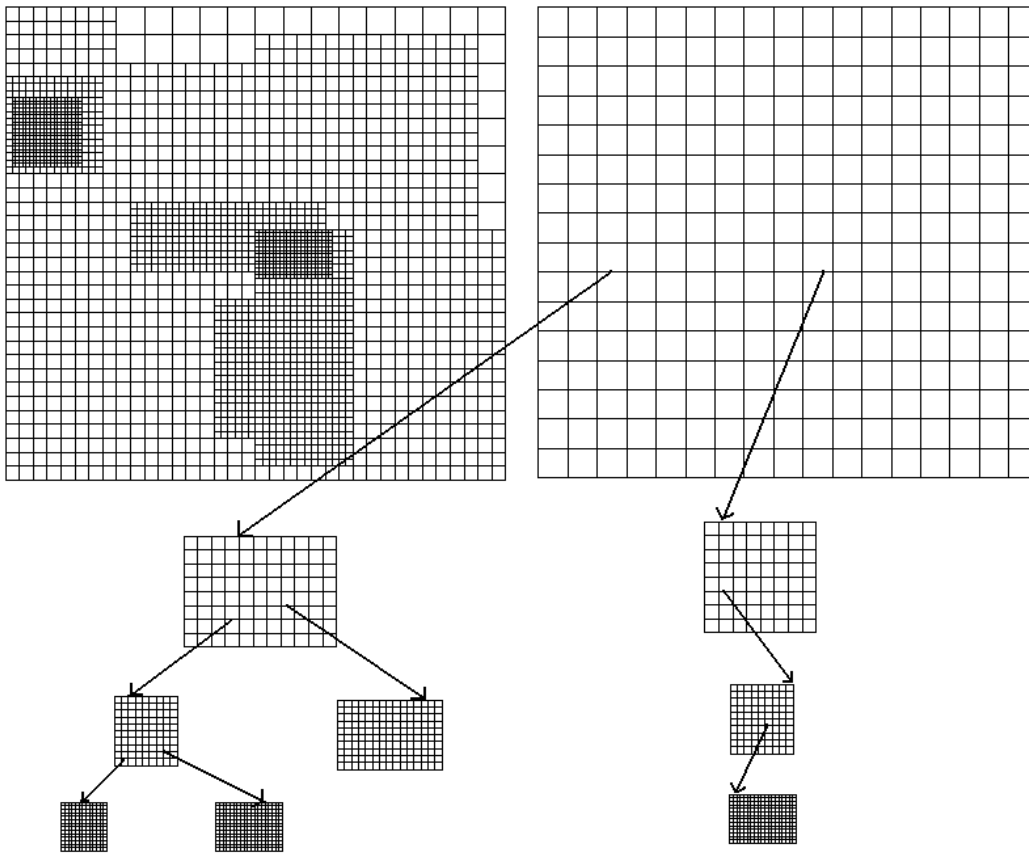


Figure 6.1.: Adaptive Mesh Refinement (AMR) schemes in ENZO N-body simulation

The criteria based on which a mesh or grid is refined, can be any of the parameters of the simulations, like, baryon and or dark-matter overdensity, shocks or jumps in various parameters, Jeans length, cell cooling time etc. This refinement can be done in all the three dimensions and for both the hydro and N-body simulations in ENZO. Grids can be refined

by any arbitrary integer ratios and there is no limit on the level of refinement in ENZO, though practically it is limited by computational resources.

An adaptive hierarchy of grid patches at various levels of resolution (see the first panel of Fig. 6.1) are utilized. Where ever higher resolution is needed several new grids are formed, each of which covers some space in its parent grid. Any or all of these child grid can become parent of a new set of higher resolution child grid. Hierarchy of grids can be explained by a tree data structure, where grids can be thought as leaves.

Initially the entire volume is filled with coarsely resolved base level grid over which the algorithm is applied. Grids are dealt as separate initial boundary value problem. When ever a new grid is employed due to refinement, boundary conditions are interpolated from its parent grid. An illustrating image i.e. Fig. 6.1 used to describe a 2D, 4-level grid hierarchy where grids at level ℓ are refined by an integer factor $R_\ell \geq 2$ relative to the grid at level $\ell - 1$.

7. Simulation of the evolution of shocks and turbulence in a major cluster merger

7.1. Objectives and setting up the simulation

In order to study the evolution of merger shocks in a theoretical framework, a constrained cosmological simulation has been planned. This chapter is devoted to the description of the simulation setup and reviews the adopted parameters, choices and approximations for fulfilling specific goals set for this project and obviously the results. In this work, from the motivation described in chapter 1, a series of events of the merger has been produced. The specific objectives of this study are:

- Simulating major mergers of clusters of galaxies in a realistic framework employing a hydrodynamic cosmological simulation.
- Following the creation and evolution of shock waves in the ICM and investigate their effects.
- Quantifying the turbulence injected into the ICM due to merger shocks and study the evolution of post shock turbulence.
- Discuss the expected effects on particle acceleration.

7.1.1. Initial conditions

Cosmological simulations of several cluster-merger events are done in this study using the Adaptive Mesh Refinement(AMR) and grid-based hybrid (N-Body plus hydrodynamical) code ENZO (O’Shea et al. 2005). The simulations are based on a flat Λ CDM background cosmology with matter density parameter $\Omega_m = 0.3$, density of baryon fraction $\Omega_b = 0.04$ with a Hubble parameter $h = 0.7$. Primordial spectrum normalization $\sigma_8 = 0.9$, and $n = 1$ is considered. The simulations were started with the same initial conditions at redshift $z_{in} = 60$ for a $128 \text{ Mpc } h^{-1}$ volume using the Eisenstein & Hu (1999) transfer function and evolved to present era i.e. $z_{final} = 0$. Cooling physics, feedback and transport processes are neglected. An ideal equation of state was used for the gas, with $\gamma = \frac{5}{3}$.

7.1.2. Simulation setup

A total of 128^3 cells and 128^3 N-Body and hydro particles in a box size of 128 Mpc were employed for initial testing. After choosing optimal values for different parameters, 64^3 cells and 64^3 N-Body particles in a simulation box of a comoving size of 128 Mpc h^{-1} were used for the final simulation. We kept in mind the simulation criteria, desired resolution and simulation cost when choosing the optimal values of different parameters required for the final work. Our final simulation is resolved with a root grid (AMR level $l = 0$) with having a comoving size of 128 Mpc h^{-1} and 64^3 cells and 64^3 N-Body particles. The mass of each of the particles in this grid is $8.3 \times 10^{11} M_{\odot} h^{-1}$. A static grid ($l = 1$) was nested inside the root grid. It has a size of 64 Mpc h^{-1} and was resolved in 64^3 cells and 64^3 particles (particle mass $1.03 \times 10^{11} M_{\odot}$). Inside this grid, in a volume of (38.4 Mpc h^{-1}), grid refinement from level $l = 2$ to $l = 6$ is enabled according to the criteria prescribed later in this paragraph. The linear refinement factor N is set to 2, allowing an effective resolution of 31.25 kpc h^{-1} at the maximum refinement level.

In the simulation, shocks seen to emerge after the clusters merged, are then followed during their evolution out of the centre to the outskirts of the cluster. As the density of the clusters at their periphery goes down to extremely low values, the detection of shocks and refinement based on the criteria of over-density cease to work well. For a better resolution at shocks throughout their evolution through the ICM, I used another refinement criterion depending on the rate of compression of the flow i.e. the negative time derivative of the divergence $d = \nabla \cdot v$ (Schmidt et al. 2008; Iapichino et al. 2008; Iapichino & Niemeyer 2008) in addition with the generally and widely used criterion based on ‘over density’. I thus succeed in refining the shocks at the outskirts of the cluster to the highest enabled level (Details in section 7.1.3).

The simulation begins at a redshift of $z_{\text{in}} = 60$. For the analysis of spatial and temporal evolution of the cluster formation, snapshots are taken at different times. Snapshots are taken more frequently during the phase when clusters are about to merge until the present era i.e. to $z_{\text{final}} = 0$. Our primary objective is to model the evolution of merger shocks and thus generated turbulence in the ICM within a realistic cosmological environment. We therefore try to find out naturally occurring major mergers i.e. I let our simulated cosmological structures to evolve within the 64^3 Mpc volume starting from a high redshift. In such a set up, mergers have occurred non-artificially and it has become possible to study the emergence of shocks thoroughly in a real cosmic web-like filamentary structured environment in 3D. As the effect of filamentary large scale structures plays an important role in shock evolution, this research made an important improvement in this area.

7.1.3. Selection of refinement criteria

ENZO is a powerful tool of cosmological simulation. Setting up the refinement is most crucial to get the desired result. My objective was to study the evolution of the shocks emerging out of a major merger which after creation at the centre evolve outwards to the

outskirts of the cluster. As the density of a cluster in reality decreases to negligibly small values at the periphery (observationally $\leq 10^{-4}$ particles per m^3), in the simulation and at the desired resolution (\sim few times 10 kpc i.e. sub galaxy order) the mass resolution goes near to the minimum particle mass i.e. $\sim 10^9$ solar masses. Thus, as at the maximum desired resolution in the simulation the neighbouring mesh particles are found rarely with nearly the same density gradient. This caused the problem of resolving the cluster periphery using the density flagging method (see panel 1 of Fig. 7.1). In addition, one had to keep in mind that the refinement criteria had to fulfill the objectives of the simulation. This prompted me to define a suitable criterion based on turbulence. Different refining cell flagging method were tested, each depending on some parameter related to turbulence. Also tested were two novel AMR criteria, developed for tracking the evolution of a turbulent flow (Schmidt et al. 2008) for the cluster merger simulation following the guidelines of Iapichino et al. (2008). The control variables for refinement in both type are given by some scalars that probe small-scale features of the flow. The first is depending on vorticity of the flow and is defined as the modulus of the vorticity $\omega = \nabla \times \mathbf{v}$ that is expected to become high in regions filled by turbulent eddies. These criteria use regional thresholds for flagging and triggering refinement. Which is much different from earlier method which normalizes the control variables in terms of characteristic quantities and compares to prescribed threshold values. The new criteria thus compare the cell value of the variable $q(x, t)$ with the average and the standard deviation of q , calculated on a local grid patch:

$$q(x, t) \geq \langle q \rangle_i(t) + \alpha \lambda_i(t) \quad (7.1)$$

where λ_i is the maximum between the average $\langle q \rangle_i$ and the standard deviation of q in the grid patch i , and α is a parameter that can be tuned to fit to a specific problem. Handling highly inhomogeneous problems becomes very easy using this technique of tuning parameters. It is found that after the transition to subsonic flow (as expected behind the shock), the simpler ω probability distribution function (pdf) found for nearly incompressible turbulence emerges i.e. eddies are formed. Strain caused by steep velocity gradients with respect to the eddy sizes becomes important in the velocity gradient contribution factor Ω . Where Ω is defined as

$$\Omega = \frac{|S|^2 - \omega^2}{|S|^2 + \omega^2} \quad (7.2)$$

Where, S is the velocity gradient of the flow.

Hence, ω^2 is the control variable that particularly resolves turbulent eddies which are associated with high vorticity but not flow features arising from pure compression such as shock fronts.

Other tested criteria were based on the rate of compression of the flow. They turned out to be best for achieving the desired resolution. The control variable in this case is given by the rate of compression, i.e., the negative time derivative of the divergence $d = -\nabla \cdot \mathbf{v}$. By choosing a somewhat lower parameter value, the entire post shock region of the structure

7.1.3 Selection of refinement criteria

can be resolved due to the expected high level of compression relaxation going on behind the shock which is just released from a high compressed region of shock front.

7.1.3.1. Comparison of the AMR criteria

A series of simulations are done to choose the best criteria(s) among the above mentioned three. All the simulation are done following the initial condition mentioned in section 7.1.1 and setup parameters as described in section 7.1.2, only instead of 2 static child grid we initially employed only 1 static grid. To get our desired final resolution of sub-galaxy scale i.e. \sim few times 10 kpc we choose a refinement level $l = 5$ i.e. the smallest resolved scale upto 38.4 kpc. Run A is made with only criteria based on ‘over-density’, Run B is made with both ‘over-density’ and criteria based on vorticity and the Run C is with criteria based on compression ratio in addition to the general criteria of ‘over-density’.

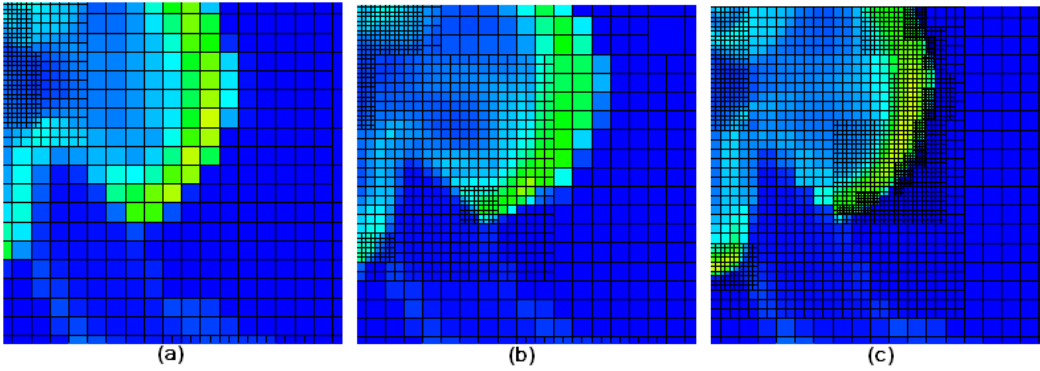


Figure 7.1: **Panel (a):** is simulated only with the ‘over-density’ criteria to refine the grids; **Panel (b):** is a simulation with the refinement criteria based on vorticity along with ‘over-density’; **Panel (c):** is a simulation with the refinement criteria based on compression ratio along with ‘over-density’

Fig. 7.1 shows that the refinement criteria based on compression ratio along with over-density could be the based choice for the simulation, where one seeks to resolve the simulation area at a far distance from centre of main cluster and where particle density goes even below 1 particle per grid cell. The analysis of the simulation discussed in section 7.12 shows that the turbulence fully develops at a large scale (~ 250 kpc), so, it clearly indicates that criteria based on vorticity (equivalent to turbulence) do not work very well. By contrast, at the shock, the gas compression is very high and for obvious reasons, the criteria based on compression ratio worked very nicely.

7.2. Resolution study

After setting a proper refinement criteria, which can resolve the shocks at the outskirts of the cluster to its highest level, I choose to work with the standard root grid resolution as 64^3 Grid with 6 levels of AMR with one static grid nested inside the root grid. It is the optimum choice that is computationally and volume (memory) wise feasible. Therefore, I tried to run simulations with 32^3 and 128^3 root grid resolution for the resolution study. It was found soon that 32^3 is such a low resolution that one could not even reproduce the merger and the subsequent shock. On the other hand, the 128^3 run failed, due to computational constraints. After several tests, three simulations with grid resolution of 48^3 , 64^3 and 96^3 were done, that were finally used for the resolution study. I will from now on call the over resolved simulation with 96^3 grids as Run 1, the reference simulation with 64^3 grid as Run 2 and the under resolved simulation with 48^3 grids as Run 3.

From the morphological point of view, a clear indication of significant time delay between the emergence of the merger and the merger shock was seen in the simulations for various resolutions. Since the onset and propagation of the merger shock are transient phenomena, they depend critically on the morphology of the merging substructures. Now, for a different setup, the initial conditions are higher or lesser resolved and thus the merging sub-clumps are displaced in space and this leads to a time-shifted shock evolution. In particular, the shock is launched at z about 0.3 in the Run 1, at $z = 0.25$ in Run 2 and at z of 0.05 for Run 3. So, in the last case, the evolution can be followed only for a very short time before $z = 0$.

In order to study the convergence from a morphological point of view, the evolution of the shock propagation in the different simulations was compensated for the above discussed time delay. The Fig. 7.2 shows a panel of 9 figures of temperature slices, with density contours superimposed. Three rows contains three panels each, corresponding to the Run 1, Run 2 and Run 3 respectively. Each panel has a side of $10 \text{ Mpc } h^{-1}$. The slice is performed on the y - z plane, cutting at the centre of mass of the cluster. Qualitatively there is a good match between Run 1 and Run 2, but as Run 3 is under resolved, it does not match at all.

The effectiveness of AMR is evaluated by a comparison of the projected refinement levels (Fig. 7.3 & Fig. 7.4). This is performed on the y - z plane over a volume of $7.7^3 \text{ Mpc } h^{-1}$ enclosing the merger. It shows a nice match for Run 1 and Run 2 at lower redshift, though Run 3 is not much resolved. Fig. 7.3 contains three panel corresponding to Run 1, Run 2 and Run 3 at $z = 0.25$, 0.2 and 0.0, respectively and fig. 7.4 has 6 panel of figures to compare Run 1 and Run 2 only, at very low redshift. The effective resolution at AMR level 6 corresponds to a spatial resolution of $20.83 \text{ kpc } h^{-1}$ in Run 1, $31.25 \text{ kpc } h^{-1}$ in Run 2 and $41.67 \text{ kpc } h^{-1}$ in Run 3.

A more quantitative comparison between the simulation with different root grid resolution is done by analysing the post-shock region. I calculated the rms velocity, measured applying the method which is explained elaborately in the section 7.3.8. The method is applied on every snapshots at different output time (i.e. at different redshifts) after the shock has emerged from the central region of the cluster for all the three setup. This quantitative analysis also shows (Fig. 7.5) a good convergence of the values of rms velocity for the Run 2 and Run 1,

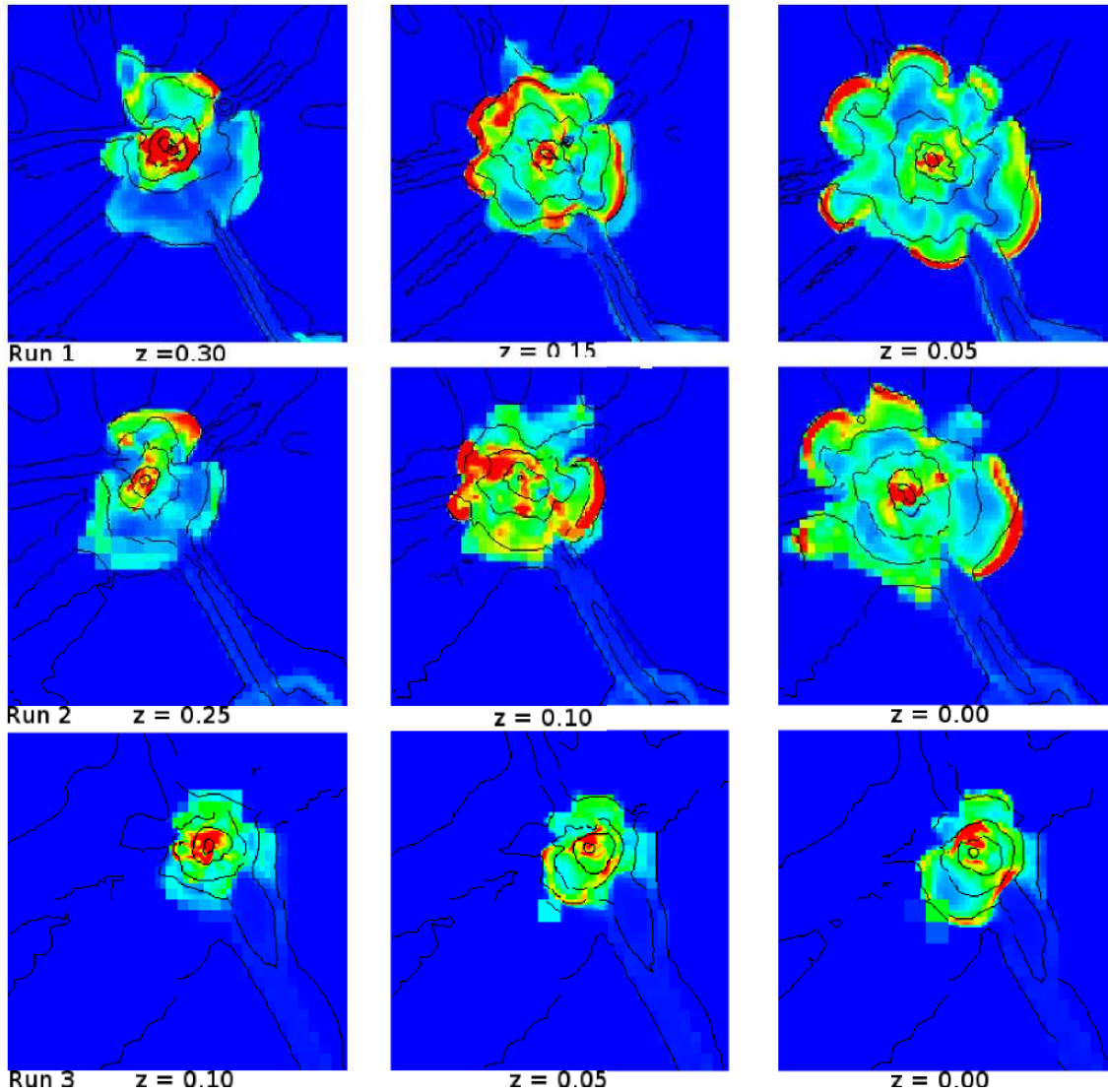


Figure 7.2.: Three rows in the figure are containing three panels; each represents the three time compensated slices of temperature map in Run 1, Run 2 and Run 3 with superimposed density contours respectively. The box size is about $10 \text{ Mpc } h^{-1}$ in each side

whereas the Run 3 clearly underestimates the velocity. The errors on the first output of each series is rather large, because it is difficult to perform the analysis when the shock has just been launched. As expected, the rms velocity is larger at earlier times and then decreases, following the adiabatic expansion of the shocked region.

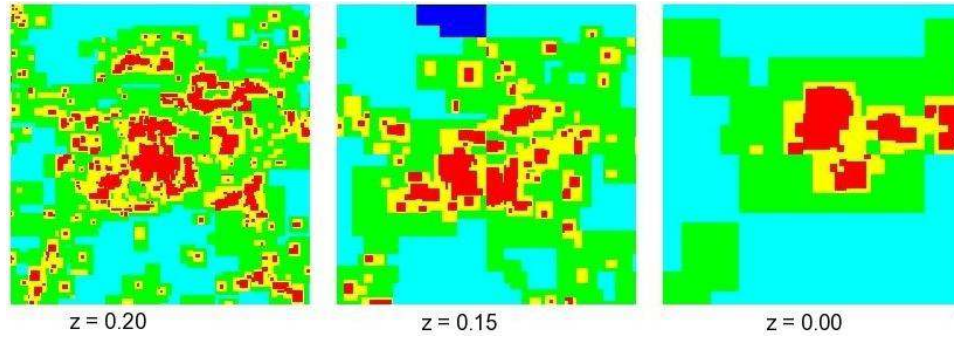


Figure 7.3.: Level of refinement (AMR) is plotted for 96 Grid 64 Grid and 48 Grid on consecutive panels. Delay of shock emergence has been compensated, 96 Grid is at $z=0.2$, 64 Grid is at $z=0.15$ and 48 Grid is at $z=0.00$. Though in every cases the level of highest possible AMR has reached but 48 Grid is clearly seen under resolved and the shock fronts thus cannot be separately seen or resolved. The morphology of 96 Grid and 64 Grid are quite similar. [colour coding: Blue = level (ℓ) 2, sky = ℓ 3, green = ℓ 4, yellow = ℓ 5 and red = ℓ 6]

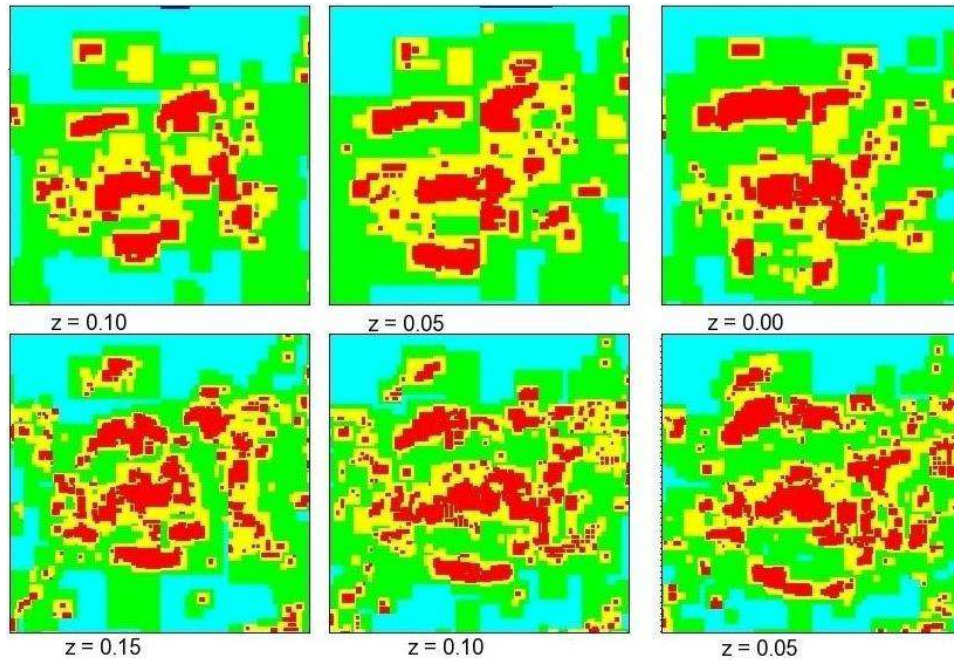


Figure 7.4.: Upper 3 panel shows level of refinement of 64 Grid and the lower three panels is of 96 Grid. Delay of shock emergence has been compensated. Structure seen in both the cases are much similar and level of resolution is at same order. [colour coding is same as Fig. 7.3]

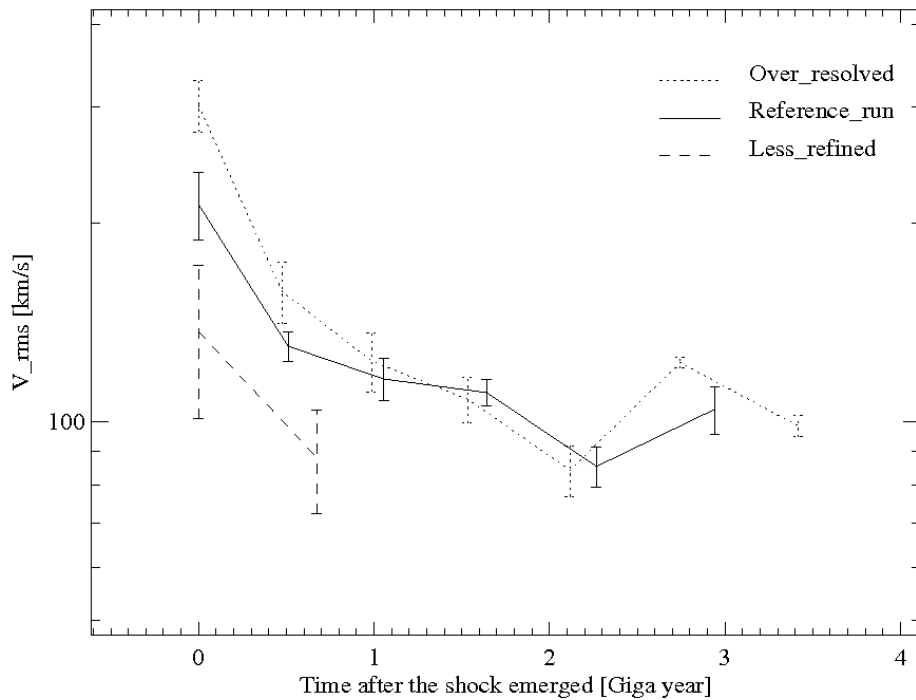


Figure 7.5.: Average RMS velocity of the post shock region is calculated using the method described in section 7.3.8 for each 96^3 , 64^3 and 48^3 , respectively, and plotted together in this plot. It shows convergence for 96^3 and 64^3 in the later stages, although 48^3 is an under resolved case.

7.3. Results

7.3.1. Different aspects of simulated clusters:

As already discussed, the structure of the Universe is formed by clustering hierarchically from small to large scales. Much of this evolution occurs very slowly but at a few special cases, more rapid, violent activity may occur as major sub-units collide at high velocities. In this process dark matter filaments are the principal agent. Filaments are usually connected to each other and form a web-like structure where each of the connection or node gathers huge amounts of matter to create a deep potential well. Those heavy cores, when coming near to each other, merge to form bigger cores or the cluster cores. Baryonic matter being very less compared to dark matter, actually follows the potential well created by dark matter web structures. The nodes when sufficiently grown form a cluster. So, in the history of formation of a cluster, it experiences several mergers, some of them are very violent and are the most energetic process known after the Big Bang.

On the basis of the cluster merging formulation of [Press & Schechter \(1974\)](#), a modified and extended model for ‘dark halo’ evolution has been proposed by [Salvador-Sole et al. \(1998\)](#). In this model they assumed that when a halo of mass M experiences a merger and achieves a final mass M' with, $\Delta M/M \equiv (M' - M)/M$, if the ratio crosses a certain threshold value of Δ_m , the existing core of the cluster gets destroyed. This merger is regarded as the formation of a new cluster core and halo. If the ratio $\Delta M/M < \Delta_m$, the event represents simply the continuous accretion, the existing core and halo keeps their identities and structure intact. [Salvador-Sole et al. \(1998\)](#) in their work showed that the best fit for new cluster formation gives $\Delta_m = 0.6$ in a number of different cosmological models. So, cluster cores structures get destroyed when $\Delta_m \geq 0.6$ and a new core and halo structure forms. However, accretion and merger can not be so sharply distinguished in the range $0.5 \leq \Delta_m \leq 0.7$. From the above relation an incident when $\Delta_m > 0.5$ can be called an accretion, the incident where $0.5 \leq \Delta_m \leq 0.7$ the phenomena can be termed as only merger. Lastly if in a merger Δ_m is ≥ 0.7 . it can be called a major merger.

Table 7.1.: Details of studied clusters:

Cluster	Merge z (approx.)	shock z (approx.)	C_m^1 $10^{13} M_\odot$	C_m^2 $10^{13} M_\odot$	$C_m^1 : C_m^2$	C_m $10^{13} M_\odot$	Δ_m	C_f Mass $10^{14} M_\odot$	R_{vir}^{final} in Mpc	T_{vir}^{final} in $10^7 K$
C-I	0.7	0.6	9.75	5.95	5:3	14.0	0.44	2.21	1.246	2.71
C-II	0.7	0.6	2.38	1.65	3:2	3.45	0.45	1.08	0.981	1.68
C-III	0.5	0.4	5.51	3.29	5:3	10.0	0.81	1.69	1.139	2.29
C-IV	0.5	0.4	2.98	2.84	1:1	5.13	0.72	0.88	0.917	1.469
C-V	0.4	0.35	9.86	5.63	5:3	27.5	1.79	4.73	1.607	4.51
C-VI	0.3	0.25	7.23	4.23	9:5	13.7	0.89	2.62	1.319	3.04
C-VII	0.25	0.2	2.11	1.045	2:1	3.21	0.52	0.59	0.803	1.13
C-VIII	-	-	-	-	-	-	-	4.80	1.614	4.55

The second column indicates the redshift at which the clusters are found to be merged. The redshift of emergence of the shocks as found in the temperature map are written in the column 3. The 4th, 5th and 6th column show the merging masses and their ratios for each case, respectively. Merged mass and the Δ_m (see the section 7.3.1) for all the merging clusters are given in column 7 and column 8.

The last three columns represent the final mass, virial radius and temperature of the respective clusters.

In the simulation, within a volume of $128^3 \text{ Mpc } h^{-1}$, about 1000 clusters were found with having a final mass of more than $10^{13} M_\odot$. Our simulation shows that mergers in the cluster formation history are a frequent phenomenon, and that it is rare to find a cluster with a mass of about $10^{14} M_\odot$ which in the course of formation never went through a merging phase. But among the numerous merger events, only a few of them experience major mergers. I paid attention to those events only and have chosen a few most-suitable clusters among them. The basis of selection of the events were thus the bigger final mass and bigger merging clusters with $\Delta_m > 0.7$ and merging masses greater than $10^{13} M_\odot h^{-1}$ to ensure the events to be among major mergers and merging clumps that can be called a cluster. Ultimately, I deeply analysed only 4 clusters (Cluster III to Cluster VI in Table 7.3.1) where a fully developed and nicely resolved shock structure is seen after mergers have taken place. Cluster I, II and Cluster VI are not fulfilling the major merger criteria and are analysed for other purpose of showing a late and early merging scenario and to increase data for statistical scaling relation. Another

cluster which on its evolutionary phase never went through a major merger (Cluster VIII in Table 7.3.1) is also simulated to provide a better comparison among the merging and non merging clusters. This cluster was termed as ‘relaxed cluster’ and those that went through major merger events are called as ‘active clusters’. Details about the examined clusters are given in Table 7.3.1.

In Table 7.3.1, mergers of different mass ratios ranging from 5:2 to 1:1 and with different merging time, starting from redshift 0.7 to redshift 0.25 are listed. I excluded the merger events which occurred at later time, since in those cases shocks didn’t clearly emerged till the redshift 0. Among the ‘active clusters’, minimum and maximum final masses are $5.9 \times 10^{13} M_{\odot}$ and $4.73 \times 10^{14} M_{\odot}$ respectively. The mass of relaxed cluster in our study is found to be $4.80 \times 10^{14} M_{\odot}$, which is as big as the biggest active cluster in our analysis. Here, the virial radius is determined by over density of a factor of 200. Δ_m values of C-I C-II and C-II shows they are barely a merging process, but I included it to have clusters with very early and late merging epoch. An apparent high Δ_m value is seen for the cluster V which could be a result of associated multiple minor mergers (as seen in the merger tree) along with the major merger indicated in the table 7.3.1.

7.3.2. Active and relaxed clusters

For better understanding of evolution of mass, energy structures in merging clusters I compared several parameters of a relaxed cluster and a merging cluster grown in nearly same astrophysical environment with the same initial parameters of simulation. Both have the nearly equal final masses (Cluster no. V and VIII in the Table 7.3.1) as $4.73 \times 10^{14} M_{\odot}$ and $4.80 \times 10^{14} M_{\odot}$. I plotted the radial variation of dark matter and baryonic matter density of the ‘relaxed’ and ‘active cluster’ by spherically averaging the values (see Fig. 7.6). The first and second panel i.e. plot (a) and (a1) shows the dark matter and baryon density of the relaxed cluster and the values are computed for different redshift. It is seen that all the curves fairly smooth and very little variation in baryonic matter for the case of a relaxed cluster. There is nearly no change with time is observed. On the contrary the curves plotted for the active cluster shows much variation especially for the baryonic matter density profile. The baryon density profile got flattened as it evolved through a merging phase. After the shock evolved, the central baryonic density went down by a noticeable amount and inflated towards the outskirts of the cluster. Even after the core oscillation of the active cluster stopped, the ripped off baryonic matter from the central part due to shock evolution did not return to its initial stage and a flat central distribution of baryonic mass can be observed.

A comparison of the evolution of different thermal and non-thermal related parameters in the above mentioned clusters are plotted in Fig. 7.7. Panel 1, i.e. the plot number (a), depicts the variation of mass and rms velocity at the cluster centres of the two clusters. I placed a spherical examining volume of diameter 512 kpc at the centre of the cluster and computed the rms velocity using the equation number 7.5. A gradual increase in mass can be noticed for the relaxed cluster, but the active cluster abruptly gains mass starting from a look-back

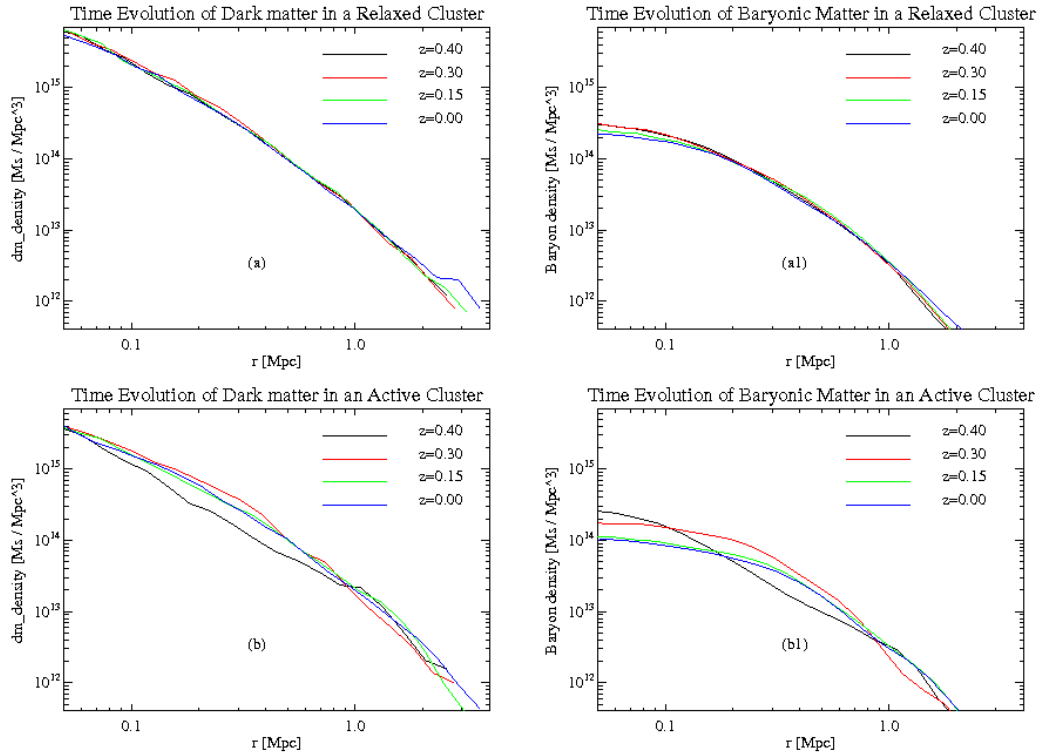


Figure 7.6.: Panel (a) and (a1): Radial dark matter and gas density variation in a relaxed cluster at different redshifts. The gas density clearly follows the dark matter profile; Panel (b) and (b1): Radial variation of dark matter and gas density profile, respectively, in an active cluster of galaxies.

time of 5 Gyr and got increased by 4 times within a short period of less than 1 Gyr. This actually shows a valid merger scenario of a cluster of galaxies.

Although the relaxed cluster is not very smooth in the central rms velocity, most probably due to central core rotation or even small mergers due to the presence of small clumps, the variation in rms velocity is still lower with respect to the active cluster which encountered nearly a 7 times increase in rms velocity. There is a delay in merging of masses and the rise in turbulent velocity which directly connects this to the emergence of shocks. The next panel shows the variation of temperature and rms velocity. Rms velocity and temperature show a correlation at the starting point, but v_{rms} (or turbulence) falls more slowly than temperature (see the plot (c)). Temperature variation incites a nice physics, due to merger activity, ICM largely gets heated up adiabatic in a short period of time to dissipate the energy released in merging process. However, the most notable observation is that, after the ICM becomes thermalized, an immediate dip in the temperature curve follows. The case can be readily explained by the emergence of shock waves. Shocks produced out of the merging super-

7.3.2 Active and relaxed clusters

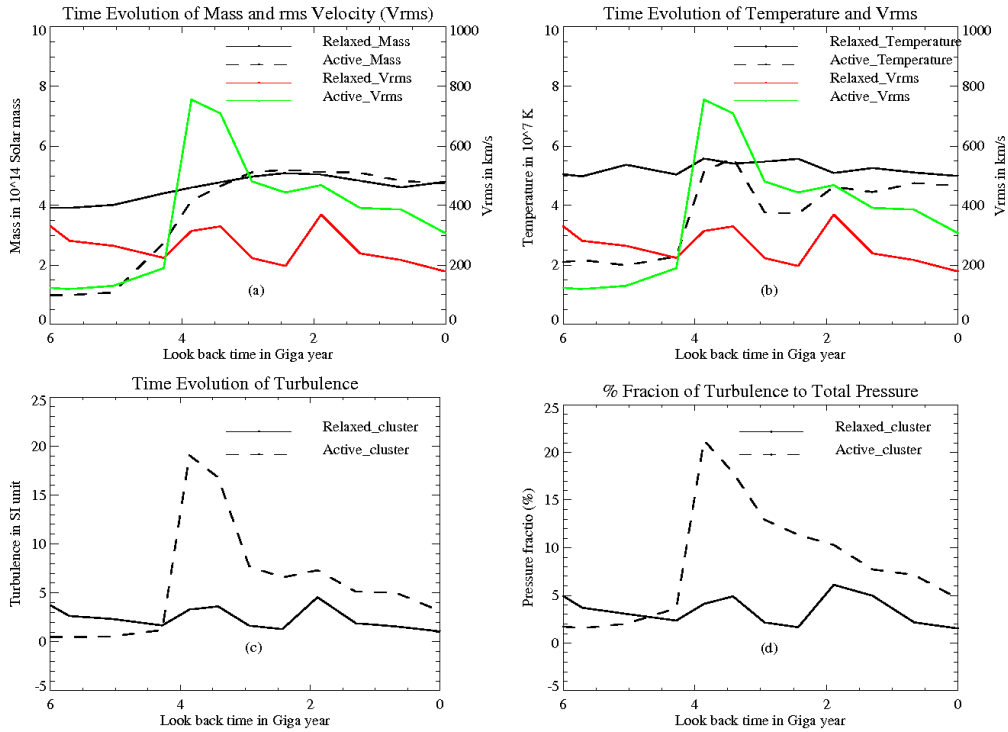


Figure 7.7.: **Panel (a):** Radial evolution of mass and rms velocity of both the relaxed (black lines) and active (coloured lines) clusters are plotted; **Panel (b):** Radial evolution of temperature and rms velocity are plotted with same colour code as earlier; **Panel (c):** Plot shows the time evolution of turbulence of relaxed (solid black line) and active clusters (dotted black line); **Panel (d):** The last panel shows the fractional turbulent pressure in the respective clusters with the same colour code as the above.

sonic flows of the gas present in the ICM expand rapidly outwards. This sudden adiabatic expansion cools down the internal medium. The shocks then drag the heat energy out of the center and spend it in spreading it to a larger volume of the cluster and accelerating the ICM non-thermal particles i.e. the thermal energy is thus converted to non-thermal energy subsequently. We have plotted the % fraction of the pressure of non-thermal i.e. turbulent to the thermal pressure in the ICM of those two clusters in the plot (d). It shows how the non-thermal pressure dominates as the shock formed in cluster due to major merger.

7.3.2.1. Long lasting central turbulence

A distinct feature is observed in our simulations. When a major merger event occurs in the newly formed cluster a substantial amount of turbulent energy is injected near the center. Turbulence pressure fraction in such a cluster found to be more than 10% till 2 Gyr after the major merger (the time scale for the shock propagation in the ICM). The turbulence remains significantly larger than that of a relaxed cluster until $z = 0$ i.e. about 4 Gyr. Turbulence at the cluster center is thus substantially longer than the typically assumed in the turbulent re-acceleration model invoked in explaining the statistics of observed radio halos (Brunetti et al. 2008). Considering the fact that the turbulence re-acceleration is responsible for the acceleration particles, the diffuse synchrotron radio emission should not disappear even after 2 Gyr. It should then just get fainter and fainter, with a chance for it to be detected in deep enough exposures. Indeed in a recently publication by Dallacasa et al. (2009) revealed a faint radio halo at 1.4 GHz with a deep VLA D-array observation. So, our simulations supported by the above observation hint at possible existence of central radio haloes associated to the peripheral radio structures in every cluster having undergone major mergers in their evolution.

7.3.3. Scaling relation

The data base of numerical examples for clusters showing the sign of a major merger is increasing according to the simulation effort. One could try to find out if a correlation between the turbulence and primary parameters of the clusters, i.e. their mass. Since it is difficult to produce an analytical theory for major mergers, an empirical approach was chosen. The scaling laws between the (i) mass (gas plus dark matter particles) of the merged clusters, M_{merge} , and the turbulent energy of the central part of the cluster, and (ii) the post shock region (extended shocked medium) of the clusters were thus investigated. The rms velocity of the cluster center was measured over a spherical volume of radius 256 kpc to include the total turbulent medium behind the shock. For the case of post shock scaling, the study was done over a sphere of radius 128 kpc to place the sphere just within the post shock extended region found in vorticity map.

The turbulent energy in a cluster was defined as the product of baryonic mass content of the studied sphere and the rms velocity within the volume

$$E_{\text{turb}} = \frac{1}{2} m_{\text{gas}} v_{\text{rms}}^2 \quad (7.3)$$

where v_{rms} is defined elaborately in section 7.3.8 as equation 7.5.

To check the scaling relation $\log[E_{\text{turb}}]$ to $\log[M']$ was plotted, where M' may be either the addition of the masses of two clusters that merged, i.e. $M' = M_{\text{merge}}$, or a product of the two, i.e. $M' = M_{\text{final}}$.

A scaling law of the form $\log[E_{\text{turb}}] \propto \log[M']^\alpha$ is thus expected. Where α is the scaling exponent. A value of 1.59 for central turbulence and 1.53 for shock structure has been

7.3.4 Merging cluster

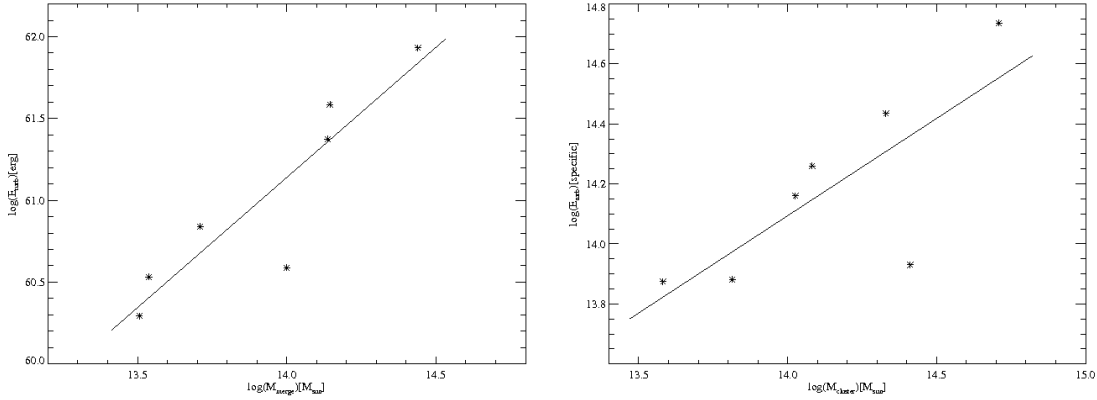


Figure 7.8: **panel 1:** Scaling relation between merged mass and turbulence energy at the centre of the cluster; **panel 2:** Scaling relation between final mass and the turbulence energy behind the shock

determined by this method. The result in this case is rather crude due to the lack of data statistics.

7.3.4. Merging cluster

Cluster VI has been chosen as the reference for doing further analysis, as this cluster has the best developed features of shock evolution and has Δ_m much greater than 0.6. This is the highest among the all binary mergers and eventually the most convenient one for the analysis of the different needed parameters.

The morphological evolution of the merging cluster (cluster VI) is shown in a panel of nine figures in coloured density slices in Fig. 7.9. We tracked the merger event in density maps of 7.7×7.7 Mpc slices cut on the y-z plane of the simulation volume along the centre of mass of the cluster. The panel of figures show the pre and post merger morphology in density of the cluster starting from redshift 0.5 to present day at redshift 0. Two filamentary nodes i.e. clusters with masses $7.23 \times 10^{13} M_{\odot}$ and $4.23 \times 10^{13} M_{\odot}$ got merged at redshift 0.3. The merging in this case is a binary merger, where clumps are moving with a relative velocity of 902 km s^{-1} along the merging axis as seen on y-z plane. Actually, the individual velocity was 661.4 km s^{-1} and 307.3 km s^{-1} . Their merging axis makes an angle of $\sim 124^\circ$ on y-z plane.

A sudden doubling of the cluster temperature can be observed as two sub-clump merge, which further rises gradually as the adiabatic heating is going on due to the motions induced in the merger. The cluster then gradually cooled down as it came to a relaxed state. Part of the energy produced in the merger is probably used up in boosting up of some non-thermal

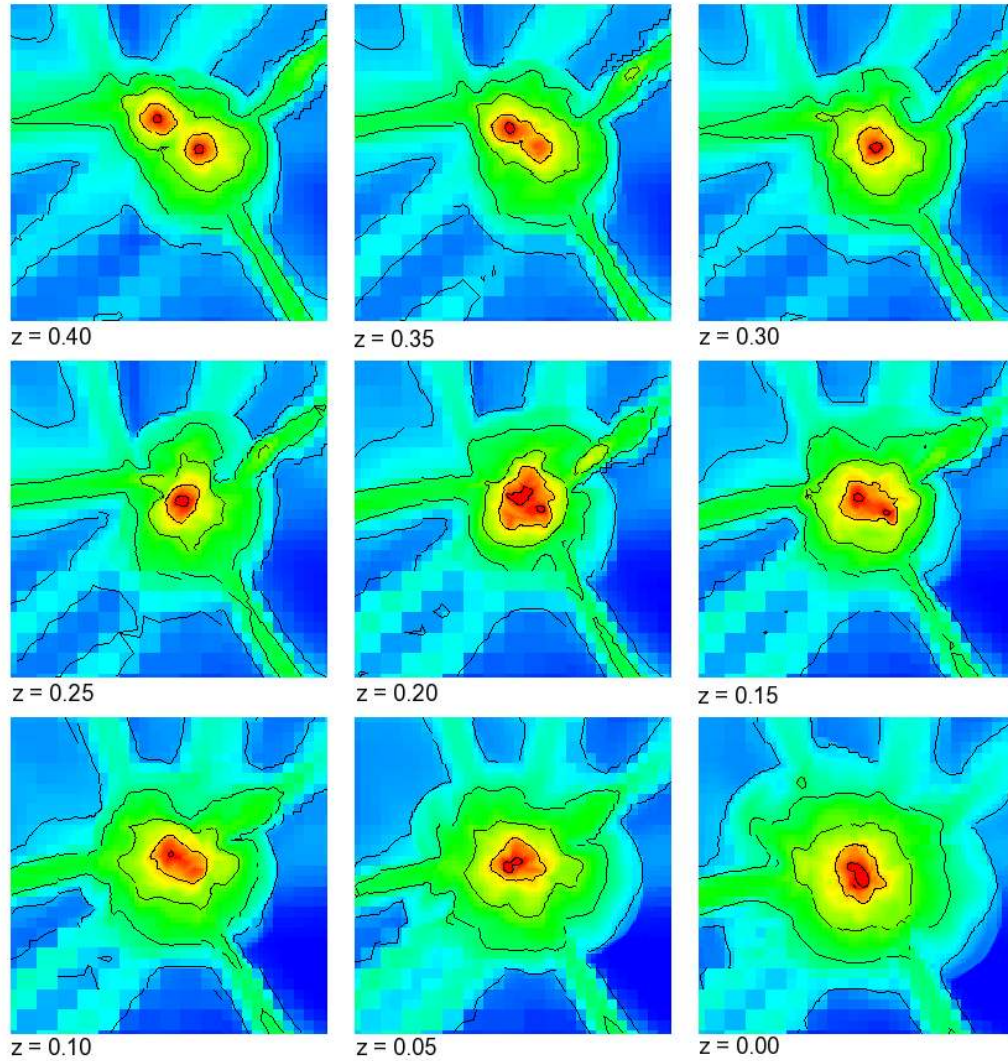


Figure 7.9.: shows the merger scenario in coloured density map of the event number VI (i.e. C-VI) in the table 7.3.1. We tracked the merger event in density maps of 7.7×7.7 Mpc slices cut on the y-z plane of the simulation volume along the centre of mass of the cluster. The panel of figures show the pre and post merger morphology in density of the cluster starting from redshift 0.4 to the present epoch i.e. to redshift 0. The redshift of the each panel is indicated below the panel as $z = \#$. The contoured density map is superimposed over the coloured map. The 5 density contours are 4.5×10^8 , 4.5×10^9 , 4.5×10^{10} , 4.5×10^{11} and 4.5×10^{12} respectively. Two filamentary nodes i.e. clusters with masses $7.23 \times 10^{13} M_{\odot} h^{-1}$ and $4.23 \times 10^{13} M_{\odot} h^{-1}$ got merged at redshift 0.3.

7.3.5 Emergence of shock waves and their evolution through the ICM:

related events such as the injection of turbulence, amplification of magnetic fields, or shock acceleration of particles in ICM.

7.3.5. Emergence of shock waves and their evolution through the ICM:

When two or more clusters of galaxies or sub-clusters of galaxies approach each other, the dark matter cores first merge and form a deep potential well in the centre of the newly formed cluster. The baryonic matter present in the ICM thus are severely attracted and driven to the centre by the intense gravitational potential created by dark matter components of the newly formed cluster. The baryonic matter thus forced to move supersonically and takes away the energy released in the merger. An abrupt change, i.e. nearly a discontinuity in cluster medium properties, occurs and eventually a shock wave emerges at the merging surface of the two different gas cloud of the two clusters. The huge energy released from merged dark matter halos and the interacting baryonic gas thus gets a channel to dissipate away through shocks in the ICM.

Fig. 7.10 shows a sequence of snapshots of the mass-weighted gas temperature in colour and density profile in contour at different epoch. It can be seen that how the two clusters of masses 7.23×10^{13} and 4.23×10^{13} , that are embedded in mega persec scale filaments got merged at redshift 0.3 which corresponds to a lookback time of 3.4 Gyr. As the peripheral matter of the two clusters start to interact, a weak shock forms (panels 2 and 3 of Fig. 7.10), and gas in between the core thus adiabatically compressed in the plane perpendicular to the collision axis. Gas velocity thus increases, as the cluster matters accelerate down the pressure gradient. The initial weak shocks then get strengthened, as the cluster cores approach each other and an adiabatic heating of the gas increases the gas temperature between the two cores (panel 4 of fig. 7.10). A strong arc-shaped shock is then driven in to the outer surface of the cluster core, just after the cores collide each other (panel 5). The shock starts emerging at redshift 0.25 (panel 5) and become clearly separated out of each other at redshift 0.2 (panel 6). Though the shocks generate only a small jump in density, I see a jump of an order of magnitude in temperature at the shocks (see the mass and temperature at shocks on panel 1-3).

Unlike to artificial binary mergers (see [Mathis et al. 2005](#) and [Ricker & Sarazin 2001](#) for reference), there are no signs of evolution of two discrete bow-shock like fronts after the shocks have separated from the central region of the cluster. Due to higher central speed of the shock along the merging axis and merging plane and the presence of a real filamentary cosmic-web structure, each of the initial binary arcs takes up a nearly hemispherical shape. They together looks like a ring-like in 2 dimensional (2D) view or like a spherical shell in 3 dimensional (3D) view (in actual sense an ellipsoidal), which start evolving through ICM symmetrically over time. The evolution of the shocks follows the paths where there is no cooling flow i.e. channeled cold matter flow through filaments uninterrupted. The shock fronts loose their energy by interacting with the cooling flows of filaments. Thereby, the

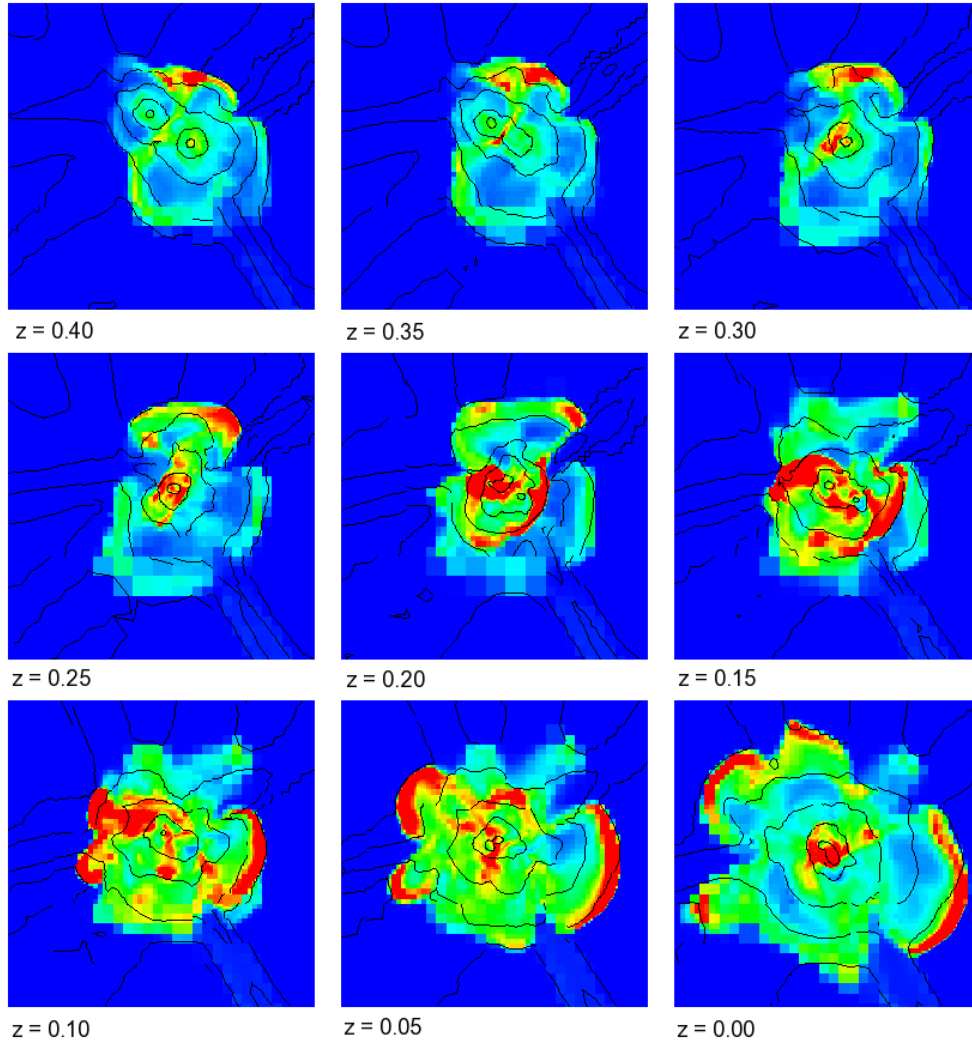


Figure 7.10.: shows the merger scenario in coloured temperature and contoured density map of the event number 6 in the Table 7.3.1. The panel of 9 figures show the temperature evolution of the cluster. The panels are cut in to slices of 7.7×7.7 Mpc on the y - z plane of the simulation volume along the centre of mass of the cluster. The figures show the pre and post merger temperature distribution in the ICM. Temperature is varying from 1 K (Blue) to $\geq 2.5 \times 10^7$ K (Red). The colour code in between are of values 6.25×10^6 K (sky blue), 1.25×10^7 K (green) and 1.875×10^7 K (yellow) respectively. There are 5 density contours with values 4.5×10^8 , 4.5×10^9 , 4.5×10^{10} , 4.5×10^{11} and 4.5×10^{12} respectively. The temperature evolution shows, after merging, how the two bow like shock fronts generate and takes up a hemispherical structure in its time of evolution through cosmic wave structures. Though the jump in density is considerable, a huge temperature jump can easily be seen (compare panel number 1,2,3 (before merging) and number 5 onwards (after emergence of shocks)).

7.3.6 Mach number of the shock

shock fronts disrupt and start losing temperature to the cooling flow. Thus, the total ring breaks into several bow-like structures in 2D and propagates only through the nearly void medium (panel 7-8-9). If a temperature-radio emission correlation is assumed (see Govoni et al. (2004)), the panel 7 and 8 is quite resembling the radio map as observed in Bagchi et al. (2006). The morphology of the emerged shock in the 3D temperature map is like a spherical shell with a small depression on the axis perpendicular to the merger axis due to shock velocity along the direction normal to the merging axis being smaller i.e. and ellipsoidal. The ‘shell’ has several holes on its surface due to filamentary cooling flows, which adiabatically cooled down the temperature produced due to shocks. In the last phase, the shock fronts then interact with the accretion shocks at the cluster periphery and finally enter the void ICM crossing the virial radius and cools down. Meanwhile, gas in the core of the merged cluster goes through a period of expansion i.e. oscillation driven by the dark matter (panel 5-6-7), then starts cooling adiabatically to slightly less than the pre-collision temperature. Finally, the dark matter cores collapse to form a nearly spherically symmetric bigger cluster core and thus gas also comes to a relaxed state to form a visible spherical cluster core (panel 9). Due to oscillation of the core, the baryonic mass, which is stronger affected, shows no correlation with the dark matter profile (see Fig. 7.6).

7.3.6. Mach number of the shock

The strength of the shock formed in such a major merger has a great importance in the calculation of different astrophysical aspects. It mainly determines the efficiency of acceleration of particles. When a shock passes over a medium it leaves its imprints as a jump of certain thermodynamical parameters. From those parameters it is easy to calculate the shock strength, i.e. the Mach number of the shock. In a simulation volume where a shock has passed, for a simple calculation if one assumes that the pre shocked medium was at rest and had thermal and pressure equilibrium, the pre and post shocked value of parameters like temperature, density and entropy uniquely determine the Mach number. The simplest relation for the Mach number using temperature is given by the Rankine-Hugoniot jump condition of temperature, i.e.

$$\frac{T_2}{T_1} = \frac{(5M^2 - 1)(M^2 + 3)}{16M^2} \quad (7.4)$$

I have examined the Mach number of the prominent shocks in our reference cluster using the above relation and an average Mach number of about 3 is calculated. The Mach number at the different shock fronts at different redshift are ranging from 2.5 to 7. The Mach number behind the shock is calculated to be varying from 2 to 3.

7.3.7. Structure function:

Large scale turbulence features have not been understood well yet. Also, there is not much observational evidence or a prediction from simulations. As I am interested in quantifying

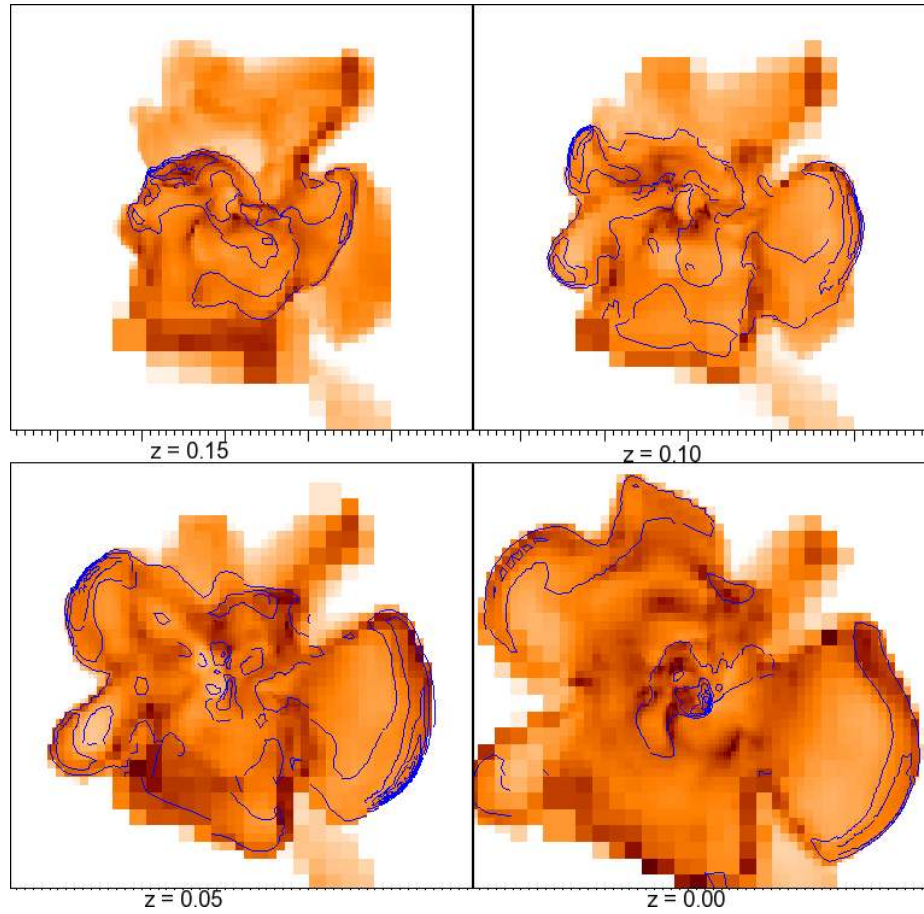


Figure 7.11.: Mach number distribution over the examined cluster is shown on the figure. Contours levels are 1,2,3,4 and 5 respectively. Average Mach number behind the shock is 2-3.

the turbulence in the studied case, I try to check the notion of self similarity in turbulent flows in the examined volume to see whether the turbulence in the shocked ICM has fully developed or not.

A Kolmogorov scaling law, i.e. a power law dependence of turbulent energy on wave number in momentum space as $\sim k^{-5/3}$ for a fully developed turbulence is proven by experiments and numerical simulations. A similar scaling law can be derived for velocity changes along a certain direction with the separation vector of any two points in the velocity space. If the velocities of two representing point is considered as $V(x+r)$ and $V(x)$ along the x axis with a separation of r and $\eta \ll r \ll L$, where, L being the integral scale of motion and η the dissipation scale, the velocity changes are calculated as $\Delta V(r) = V(x+r) - V(x)$. So, the probability density function (PDF) of velocity must be calculated as $\langle \Delta V(r)^n \rangle \approx r^{\zeta(n)}$ using Taylor's hypothesis and is a more general form of the Kolmogorov theory. Here n is

7.3.8 Generation and evolution of turbulence in the post shock ICM

the structure function order and in a fully developed regime $\zeta(n)$ is $n/3$. The second order structure function will thus have the exponent $\zeta(2) = 2/3$. It can be shown that the second order structure function is nothing but the Kolmogorov spectrum i.e. $E(k) \propto k^{-5/3}$. So, the calculated second order structure function of the merging cluster could give a hint of the level of turbulence present in the ICM.

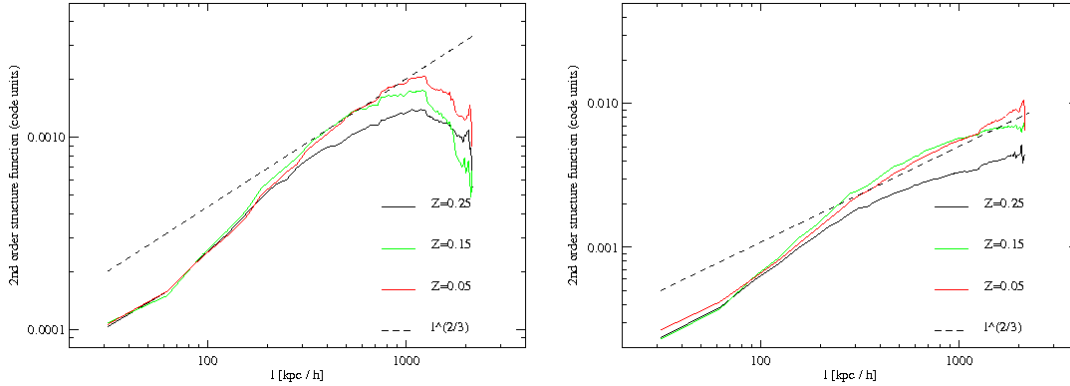


Figure 7.12.: Longitudinal and transverse structure function at different redshifts as mentioned in the figures. The dotted line shows the theoretical Kolmogorov type velocity structure.

Fig. 7.12 clearly indicates a large scale turbulence. Above ~ 250 kpc, the calculated structure function nearly matches the theoretical $\zeta(2) = 2/3$ line. There is also an indication that the ICM becomes nearly turbulent as the shock evolves through the medium.

7.3.8. Generation and evolution of turbulence in the post shock ICM

Merging of clusters of galaxies induce large scale bulk motions with velocities of the order of about 1000 km s^{-1} . Bulk motion of the ICM gas and mixing of different medium of the merging clumps thus results in complex hydrodynamic flows. Though the dissipation of most of the merging generated kinetic energy takes place through thermal heating of the ICM by shocks and adiabatic compression, a noticeable part of the energy may also excite long lasting turbulent gas motion in the medium (Dolag et al. 2005).

In the simulation one can see, just after the emergence of shocks from the cluster centre, turbulence is injected just behind the shocks and propagates along with it. The Fig. 7.13 shows how the turbulence detected in a vorticity i.e. $\nabla \times v$ map at different snapshots of the simulation at different redshifts (where v is the velocity of the gas flow) of the examined cluster. The vorticity map shows, before the merging took place a little noticeable level of turbulence prevailed at the site and also it is confined near to the cluster centres. The amount of turbulence jumped to a larger value just after the shock has emerged at the centre

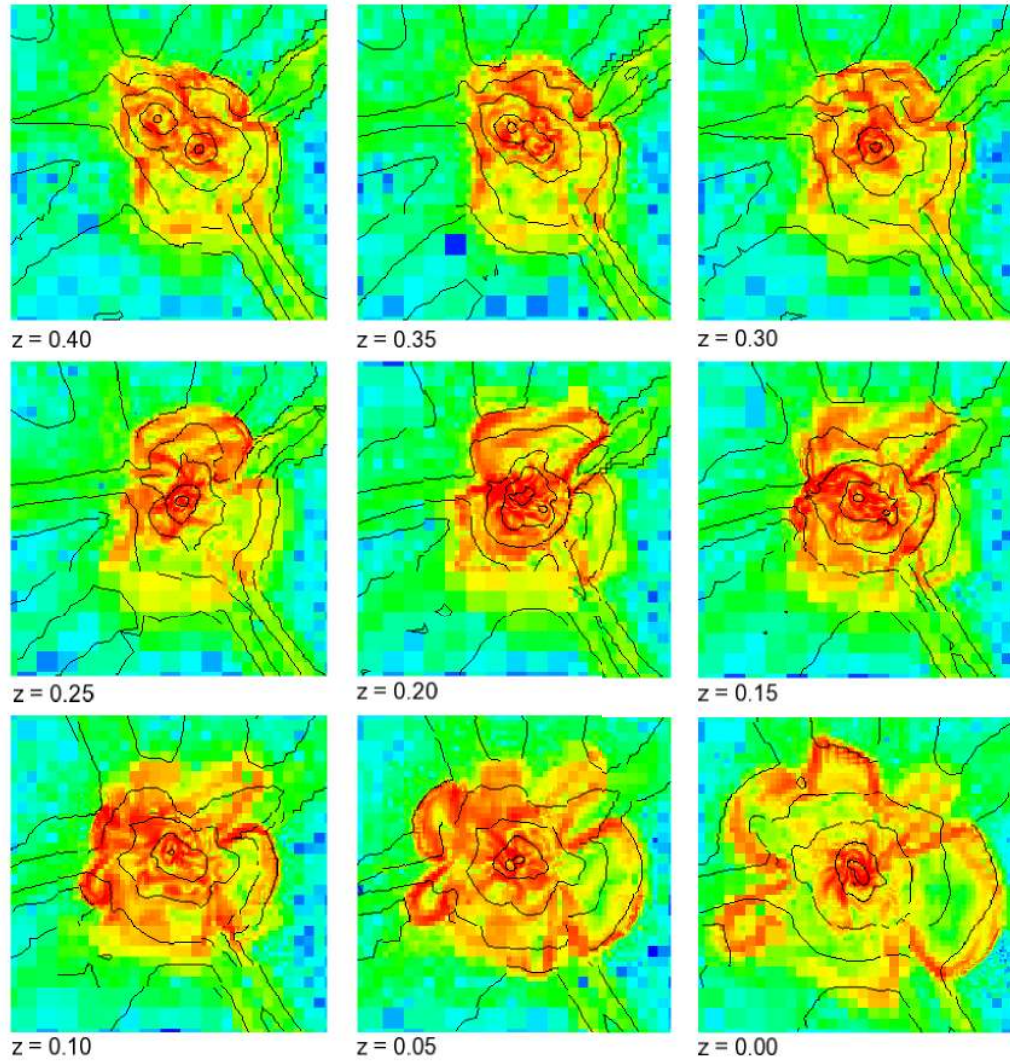


Figure 7.13.: shows the merger scenario in coloured normalized vorticity map of the event number 5 in the table 7.3.1. The contoured density map is superimposed over the coloured map. Five density contours are 4.5×10^8 , 4.5×10^9 , 4.5×10^{10} , 4.5×10^{11} and 4.5×10^{12} respectively. We tracked the merger event in vorticity maps of 7.7×7.7 Mpc slices cut on the y - z plane of the simulation volume along the centre of mass of the cluster. The panel of figures show the pre and post merger morphology in vorticity of the cluster starting from redshift 0.4 to present day at redshift 0. The redshift of the each panel is indicated below the panel as $z = \#$. We see how the level of turbulence (as astrophysical turbulence is defined as vorticity $\omega = \nabla \times v$)

7.3.8 Generation and evolution of turbulence in the post shock ICM

at redshift 0.20 and then started evolving through the ICM along with the propagated shock fronts (compare with the temperature map in fig. 7.10). After the injection of turbulence, it grows further in the medium until redshift 0.15 and is then slowly smeared out. The level of turbulence slowly decays, but the turbulent volume spreads until the virial radius of the newly formed cluster (see the panel no. 7-8-9) is reached. Thus, the turbulence injected at the centre is carried along with the shocks to the periphery of the cluster.

Table 7.2.: Maximum turbulent energy at the cluster centre:

Simulation	C-I $10^{13} M_{\odot}$	C-II $10^{13} M_{\odot}$	$V_{\text{rms(max.)}}$ km s^{-1}	$E_{\text{turb(max.)}}$ 10^{10} SI unit
Cluster I	2.38	1.65	314.70	4.95
Cluster II	5.51	3.29	284.98	4.06
Cluster III	2.98	2.84	387.03	7.49
Cluster IV	9.86	5.63	756.04	28.58
Cluster V	7.23	4.23	611.87	18.72
Cluster VI	2.11	1.045	271.30	3.68

The 2nd and 3rd column show the merging masses, respectively. The last two columns represent the maximum rms velocity and the maximum turbulent energy at the centre of each cluster.

For better analysis of only the post shock turbulence, I placed the analysis spherical volume just behind the shock. From an operational point of view, the calculation of a root mean square (henceforth rms) velocity implies the definition of an average reference velocity, in order to distinguish between the bulk velocity flow and the velocity fluctuations (cf. Dolag et al. 2005). The mass-weighted rms baryon velocity is then defined as

$$v_{\text{rms}} = \sqrt{\frac{\sum_i m_i (v_i - \langle v \rangle)^2}{\sum_i m_i}} \quad (7.5)$$

where, m_i is the mass contained in the cell i , and the summation is performed over the cells belonging to the spherical volume with radius r .

I choose analysis spheres of diameter of 256 kpc, which is nearly same as the spatial extension of the turbulent post shock volume (Fig. 7.15) and placed them in the downstream of the merger shock and inside the shocked region. A shock structure which was well visible in all the simulations was chosen for this test. I placed a small number of analysis spheres in order to avoid spurious fluctuations of the results. The resulting rms velocities are averaged, a standard error bar is plotted for every set of results to show its statistical reliability. The method is then applied at every epoch for which snapshots are taken (i.e. at different snapshots of the simulation i.e. at different redshifts) after the shock has well emerged from the central region of the cluster. In Fig. 7.14, the time after emergence of shocks is plotted

on the x-axis and on the y-axis the rms velocity i.e. v_{rms} . The time evolution of rms velocity shows how a huge level of turbulence that is injected at the centre of the cluster as the shock has emerged and then slowly decays over a time span of about 3 Giga years.

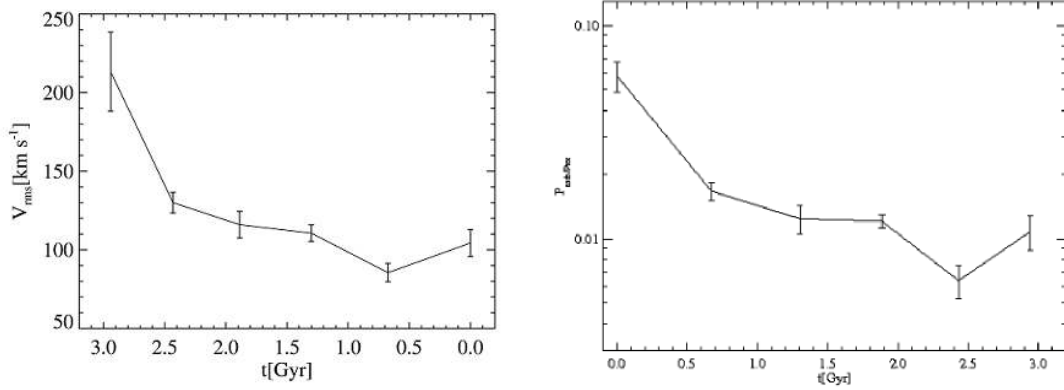


Figure 7.14: **Panel 1:** shows a plot of rms velocity of the downstream region (post shock ICM). On the x axis we plotted the lookback time in Giga years from the time when the shock started emerging. The y axis shows the average rms velocity evaluated for different analysis spheres placed behind the shock. Error bars are the standard error of the results from the analysis at each redshift. **Panel 2:** shows a plot of ratio of turbulent to total (total of thermal and turbulent) pressure of the downstream region (post shock ICM). On the x axis, the lookback time in Giga years is plotted from the time when the shock started emerging. The y axis shows the average of the above mentioned ratios evaluated for different analysis sphere placed behind the shock. Error bars are the standard error of the results from the analysis at each redshift.

A separate plot (panel 2 of Fig. 7.14) has been prepared to show the evolution of the fraction of turbulent pressure over the thermal pressure that has been introduced by the merger shock in the ICM

$$\frac{P_{\text{turb}}}{P_{\text{tot}}} = \frac{v_{\text{rms}}^2/3}{kT/(\mu m_p) + v_{\text{rms}}^2/3} \quad (7.6)$$

to compare the contribution of turbulent pressure at the shocks in a cluster that experienced a major merger in recent past.

In the plots of the Fig. 7.14 a noticeable and unexpected result has been obtained. One can see a bump in the curve at late times ($t \sim 65$), which corresponds to the time when the shocked region reaches the location of the accretion shock. At that time, an increase in v_{rms} by 25% can be observed, instead of the expected decay. Probably, the reason for this bump is the regeneration of the turbulence due to the interaction of the two shock fronts.

7.3.9. Extension of turbulent medium:

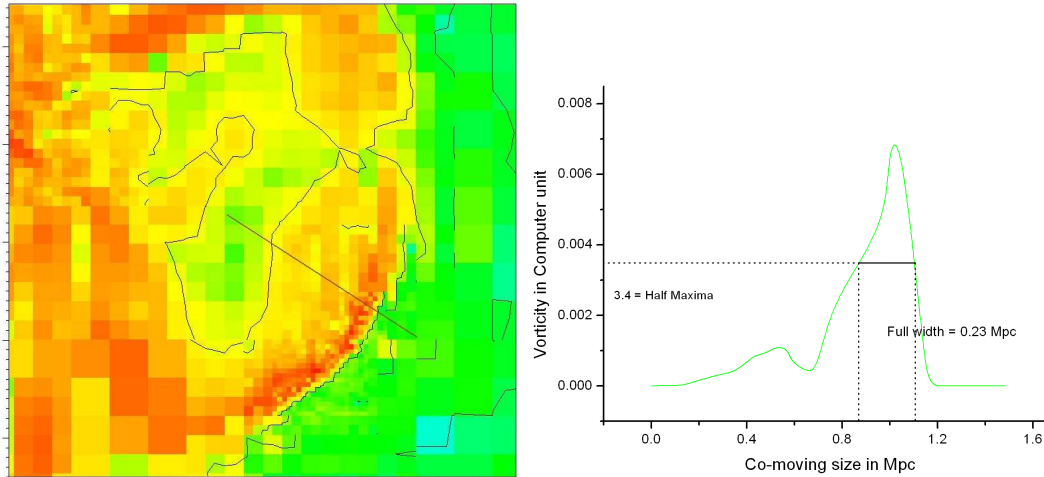


Figure 7.15.: Panel 1: Vorticity i.e. $\nabla \times v$ map of the shock front. It can be clearly noticed that the vorticity is extended to few hundred kpc behind the shock front. Data taken along the indicated line is plotted to measure its exact maximum extension in Fig. 7.15. **Panel 2:** Data from the panel 1 Fig. 7.15 along the line indicated is taken and a line plot is prepared to calculate its exact extension. The Full Width at Half Maximum could thus be measured to quantify the extended turbulent region behind the shock front. From the above figure the extension has a value of about $230 \text{ kpc } h^{-1}$

From both observed radio structures in Abell 3667 & Abell 3376 and the N-body + hydrodynamical simulations presented here, it is evident that the shock waves and strong bulk-flow motion exist in the ICM during major mergers. The high-energy electrons responsible for the radio synchrotron emission can be produced at the shock fronts by Fermi-I acceleration. The Fermi-II process could accelerate the particles in the extended down-stream region behind the shocks, and could thus explain the absence of a spectral index gradient that would otherwise be expected owing to synchrotron losses. I found a spatial extension i.e. the back stream extension, of more than a $100 \text{ kpc } h^{-1}$, where the turbulence evolved for more than a Giga year along the propagation of the shocks. From the Fig. 7.13 (panel 3-9) one can see, just before the merger took place, that only a small region around the cluster core had a high level of vorticity. However, as the shock emerges, the core becomes turbulent (high vorticity) and then grows in volume as the shock wave propagates out of the centre to the periphery of the cluster injecting turbulence in the ICM. The turbulence fills nearly the entire volume of the cluster, although a higher value of vorticity can be noticed near the shock, which we referred to as the spatial extension of the shock and has a value of about $200\text{-}250 \text{ kpc } h^{-1}$ (Fig. 7.15).

8. Summary & Discussion

Major merger events in clusters of galaxies provide a snapshot picture of large-scale structure formation in the Universe in which one can witness the transfer of energy from the largest to the smallest scales by the interplay of shock waves, turbulence, particle acceleration, and heating. It is generally not tractable, neither observationally, nor numerically, to follow the sequence of the involved processes on all scales, and this poses the problem of finding a proper pragmatic approach to making the next step towards a better understanding. In the preparatory phase for this project, radio and X-ray observations of the cluster Abell 3376 revealed a giant ring or a bow like structure (Bagchi et al. 2006). The structure was suspicious for Fermi-I acceleration at the merger or accretion shock to produce the relativistic particles observed through their radio synchrotron emission, and this radio emission occurred far away from the heated X-ray emitting core of the merging cluster. This cluster seemed to hold the key to better understand how particle acceleration and shock formation transfer energy to the ICM.

In this thesis, therefore, the chosen approach was to compare radio and X-ray observations of the merging cluster Abell 3376 with constrained numerical simulations to learn about the build-up of nonthermal particle populations in the ICM. Results of the study will be discussed in the subsequent sections.

8.1. Discussion of the main findings

8.1.1. Nature of shocks in Abell 3376

The cluster Abell 3376 has been observed both at 20cm and 6cm wavelengths using the VLA radio telescope array in New Mexico, USA. The observations revealed the images of two well-resolved shock fronts. The extreme elongated X-ray brightness at the centre of cluster indicates an ongoing merger or accretion activity. The theoretical expectation of a merger scenario is that a bow shock should emerge from the centre and travel to the periphery. On the other hand, a nearly static bow shock with similar morphology may appear due to accretion of matter on a cluster periphery. Miniati et al. (2000b) and Ryu et al. (2003) have distinguished them cleverly by terming them as ‘external’ and ‘internal’ shocks on the basis of their Mach number. From their findings, the related radio spectral index of the radio structures corresponding to the shocks can be estimated. For merger shocks, a radio spectral index of more than 0.58 is expected (see details in section 5.2.1.2). From our latest observation of Abell 3376 at 6cm and 20cm, a radio spectral index of ~ 0.95 to 1.05 has

8.1.2 Morphological similarity

been found. In case of Abell 3667, [Rottgering et al. \(1997\)](#) found an average spectral index of 1.1 which is remarkably similar, although in a few regions of both the clusters ([Roettiger et al. \(1999\)](#) and 5.6) a flatter spectral index has been observed. My conclusion from the observations of the radio structures thus is that they can definitely not be the product of an accretion or mixed accretion-merger shock. Instead, they seem to correspond to a pure merger shock. The Mach number computed from the DSA model ranges from 2.5 to 2.8, and these values have also been found in the numerical simulations (see section 7.11).

8.1.2. Morphological similarity

A striking similarity in morphology can be noticed between the observed Abell cluster (combined map of VLA radio and ROSAT X-ray) and the simulated merging cluster VI (temperature, vorticity or hydrodynamical turbulence and X-ray projection map) [Fig. 8.1]. As a first order approximation, we assumed coupling of the compressional modes resolved in the hydrodynamic turbulence to the Alfvénic turbulence that is needed for particle acceleration according to the Fermi mechanism.

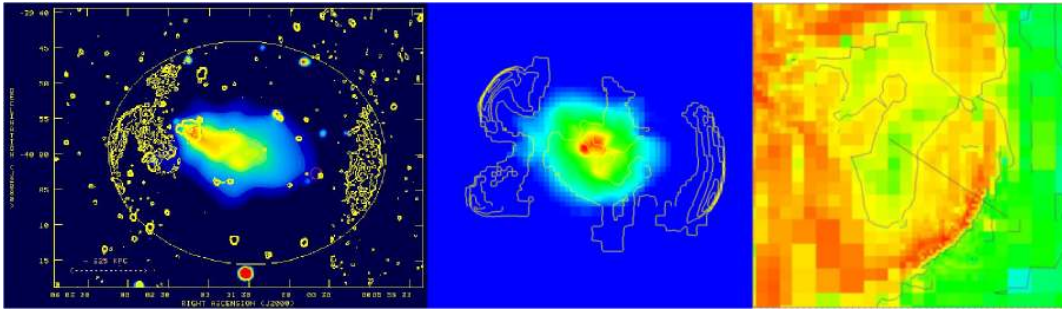


Figure 8.1: **Panel 1:** A superimposed image of VLA 20cm radio and ROSAT 0.14-2keV X-ray map; Image is taken from [Bagchi et al. \(2006\)](#). Reprinted with permission from AAAS. **Panel 2:** Simulated temperature map of the merging cluster is drawn as a contour, projected X-ray surface brightness (0.14-2.0 keV) is superimposed as a colour image; **Panel 3:** The inset shows an enlarged map in vorticity for the western shock front of the simulated cluster.

Both the observed and the simulated cluster have a comparable mass of $\sim 0.5 \times 10^{15} M_{\odot}$, major axis of elliptical structure of $\sim 1 \text{ Mpc } h^{-1}$, ICM temperature of $\sim 5 \times 10^7 \text{ K}$, length of the shock structures about $1 \text{ Mpc } h^{-1}$ and, most importantly, both have an extension behind the shock front of about $250 \text{ kpc } h^{-1}$. The radio morphology clearly matches the morphology of the simulated structure in temperature and vorticity tracing turbulence (see also Fig. 7.10 and 7.13). We predict existence of a faint central radio halo in this cluster which could be detected in deep low frequency observations (see section 7.3.2.1 for detail reasoning).

8.1.2.1. Extension of the shock and Fermi-II acceleration

The spectral index map of Abell 3376 (see Fig. 5.6) provides information about the post shock region or the region just behind the shock front. The marked absence of a spectral index gradient across the extended region argues against spectral ageing due to synchrotron losses and shows the importance of re-acceleration within the extended region. Electrons that are accelerated at the shock should have life times shorter than the total shock evolution time ($t_{elec} \sim 10^8$ yrs $\ll t_{shock} \sim 10^{10}$ yrs). For Fermi-I acceleration at the shock, the synchrotron emission from the accelerated electrons is expected only from a narrow region behind the shock with a steep spectral index (see section 2.3.3.4). A rather small spread of the emission zone (corresponding to about thousand diffusion lengths) is expected due to advection and diffusion. However, an extended zone of long-lasting synchrotron radiation can be expected if the particle can tap the energy stored in the MHD turbulence. When a shock is propagated through the ICM, powerful wake turbulence is generated. In the turbulent medium, the particles will experience momentum diffusion from stochastic wave-particle interactions, i.e. Fermi-II acceleration, and this counteracts spectral steepening with increasing distance from the shock.

8.1.2 Morphological similarity

.

Bibliography

- Albrecht, A. & Steinhardt, P. J. 1982, *Physical Review Letters*, 48, 1220
- Bagchi, J., Durret, F., Neto, G. B. L., & Paul, S. 2006, *Science*, 314, 791
- Berger, M. J. & Colella, P. 1989, *Journal of Computational Physics*, 82, 64
- Bertschinger, E. 1985, *ApJS*, 58, 39
- Blandford, R. & Eichler, D. 1987, *Physics Report*, 154, 1
- Blasi, P. 2000, *NASA STI/Recon Technical Report N*, 1, 114
- . 2001, *Astroparticle Physics*, 15, 223
- Bonafede, A., Feretti, L., Giovannini, G., et al. 2009, *A&A*, 503, 707
- Bond, J. R., Cole, S., Efstathiou, G., & Kaiser, N. 1991, *ApJ*, 379, 440
- Bond, J. R., Kofman, L., & Pogosyan, D. 1996, *Nature*, 380, 603
- Brunetti, G. 2003, in *Astronomical Society of the Pacific Conference Series*, Vol. 301, *Astronomical Society of the Pacific Conference Series*, ed. S. Bowyer & C.-Y. Hwang, 349–+
- Brunetti, G., Giacintucci, S., Cassano, R., et al. 2008, *Nature*, 455, 944
- Brunetti, G., Setti, G., Feretti, L., & Giovannini, G. 2001, *MNRAS*, 320, 365
- Bryan, G. L., Norman, M. L., Stone, J. M., Cen, R., & Ostriker, J. P. 1995, *Computer Physics Communications*, 89, 149
- Buote, D. A. 2001, *ApJL*, 553, L15
- Bykov, A. M., Dolag, K., & Durret, F. 2008, *SSRv.*, 134, 119
- Chandrasekhar, S. 1942, *Principles of stellar dynamics (Physical Sciences Data)*
- Dallacasa, D., Brunetti, G., Giacintucci, S., et al. 2009, *ApJ*, 699, 1288
- Dolag, K., Bartelmann, M., & Lesch, H. 1999, *A&A*, 348, 351
- . 2002, *A&A*, 387, 383

- Dolag, K., Vazza, F., Brunetti, G., & Tormen, G. 2005, *MNRAS*, 364, 753
- Doroshkevich, A. G., Tucker, D. L., Oemler, A. J., et al. 1996, *MNRAS*, 283, 1281
- Drury, L. O. 1983, *Reports on Progress in Physics*, 46, 973
- Duffy, P. & Blundell, K. M. 2005, *Plasma Physics and Controlled Fusion*, 47, B667
- Durret, F., Lima Neto, G. B., & Forman, W. 2005, *Advances in Space Research*, 36, 618
- Efstathiou, G., Davis, M., White, S. D. M., & Frenk, C. S. 1985, *ApJS*, 57, 241
- Eilek, J. & Weatherall, J. C. 1999, in *Diffuse Thermal and Relativistic Plasma in Galaxy Clusters*, ed. H. Boehringer, L. Feretti, & P. Schuecker, 249–+
- Einasto, M., Tago, E., Jaaniste, J., Einasto, J., & Andernach, H. 1997, *A&AS*, 123, 119
- Eisenstein, D. J. & Hu, W. 1999, *ApJ*, 511, 5
- Ensslin, T. A., Biermann, P. L., Klein, U., & Kohle, S. 1998, *A&A*, 332, 395
- Enßlin, T. A. & Gopal-Krishna. 2001, *A&A*, 366, 26
- Escalera, E., Biviano, A., Girardi, M., et al. 1994, *ApJ*, 423, 539
- Faber, S. M. & Gallagher, J. S. 1979, *ARA&A*, 17, 135
- Feretti, L., Dallacasa, D., Govoni, F., et al. 1999, *A&A*, 344, 472
- Fermi, E. 1949, *Physical Review*, 75, 1169
- Fillmore, J. A. & Goldreich, P. 1984, *ApJ*, 281, 1
- Flin, P. & Krywult, J. 2006, *A&A*, 450, 9
- Fujita, Y., Takizawa, M., & Sarazin, C. L. 2003, *ApJ*, 584, 190
- Fusco-Femiano, R., dal Fiume, D., Feretti, L., et al. 1999, *ApJL*, 513, L21
- Fusco-Femiano, R., Orlandini, M., De Grandi, S., et al. 2003, *A&A*, 398, 441
- Giovannini, G., Feretti, L., Venturi, T., Kim, K.-T., & Kronberg, P. P. 1993, *ApJ*, 406, 399
- Giovannini, G., Tordi, M., & Feretti, L. 1999, *New Astronomy*, 4, 141
- Govoni, F., Markevitch, M., Vikhlinin, A., et al. 2004, *ApJ*, 605, 695
- Gunn, J. E. & Gott, J. R. I. 1972, *ApJ*, 176, 1
- Guth, A. H. 1981, *Phys. Rev. D*, 23, 347

- Harris, D. E., Lari, C., Vallee, J. P., & Wilson, A. S. 1980, *A&AS*, 42, 319
- HIRSCH, C. 1988, *NUMERICAL COMPUTATION of INTERNAL and EXTERNAL FLOWS* (JOHN WILEY and SONS Ltd)
- Hockney, R. W. & Eastwood, J. W. 1988, *Computer simulation using particles* (Bristol: Hilger, 1988)
- Hoeft, M., Brüggem, M., & Yepes, G. 2004, *MNRAS*, 347, 389
- Hoeft, M., Brüggem, M., & Yepes, G. 2005, *Astronomische Nachrichten*, 326, 613
- Iapichino, L., Adamek, J., Schmidt, W., & Niemeyer, J. C. 2008, *ArXiv e-prints*, 801
- Iapichino, L. & Niemeyer, J. C. 2008, *ArXiv e-prints*, 801
- Kang, H. & Jones, T. W. 2005, *ApJ*, 620, 44
- Kang, H., Ryu, D., Cen, R., & Ostriker, J. P. 2007, *ApJ*, 669, 729
- Kempner, J. C., Blanton, E. L., Clarke, T. E., et al. 2004, in *The Riddle of Cooling Flows in Galaxies and Clusters of galaxies*, ed. T. Reiprich, J. Kempner, & N. Soker, 335–+
- Keshet, U., Waxman, E., & Loeb, A. 2004, *ApJ*, 617, 281
- Keshet, U., Waxman, E., Loeb, A., Springel, V., & Hernquist, L. 2003, *ApJ*, 585, 128
- Lacey, C. & Cole, S. 1993, *MNRAS*, 262, 627
- Landau, L. D. & Lifshitz, E. M. 1959, *Fluid mechanics* (Oxford: Pergamon Press)
- Lynden-Bell, D. 1967, *MNRAS*, 136, 101
- Mathis, H., Lavaux, G., Diego, J. M., & Silk, J. 2005, *MNRAS*, 357, 801
- Melrose, D. B. 1980, *Plasma astrophysics: Nonthermal processes in diffuse magnetized plasmas. Volume 2 - Astrophysical applications* (New York, Gordon and Breach Science Publishers, 1980. 430 p.)
- Miniati, F. 2003, *MNRAS*, 342, 1009
- Miniati, F., Jones, T. W., Kang, H., & Ryu, D. 2001, *ApJ*, 562, 233
- Miniati, F., Ryu, D., Kang, H., et al. 2000a, *ApJ*, 542, 608
- . 2000b, *ApJ*, 542, 608
- Nakazawa, K., Kawano, N., Fukazawa, Y., et al. 2007, *Progress of Theoretical Physics Supplement*, 169, 45

- Nakazawa, K., Sarazin, C. L., Kawaharada, M., et al. 2009, PASJ, 61, 339
- Norman, M. L. & Bryan, G. L. 1999, in *Lecture Notes in Physics*, Berlin Springer Verlag, Vol. 530, The Radio Galaxy Messier 87, ed. H.-J. Röser & K. Meisenheimer, 106–+
- O’Shea, B. W., Bryan, G., Bordner, J., et al. 2005, in Plewa T., Linde T., Weirs V.G, eds, *Lecture Notes in Computational Science and Engineering*, Vol. 41, Adaptive Mesh Refinement – Theory and Applications. Springer, Berlin, New York, 341
- Pearson, T. J. & Readhead, A. C. S. 1984, ARA&A, 22, 97
- Perrenod, S. C. 1978, ApJ, 224, 285
- Pfrommer, C., Enßlin, T. A., & Springel, V. 2008, MNRAS, 385, 1211
- Pfrommer, C., Springel, V., Enßlin, T. A., & Jubelgas, M. 2006, MNRAS, 367, 113
- Press, W. H. & Schechter, P. 1974, ApJ, 187, 425
- Rephaeli, Y. 1979, ApJ, 227, 364
- Ricker, P. M. & Sarazin, C. L. 2001, ApJ, 561, 621
- Ritchie, B. W. & Thomas, P. A. 2002, MNRAS, 329, 675
- Roettiger, K., Burns, J. O., & Stone, J. M. 1999, ApJ, 518, 603
- Rottgering, H. J. A., Wieringa, M. H., Hunstead, R. W., & Ekers, R. D. 1997, MNRAS, 290, 577
- Ryu, D., Kang, H., Cho, J., & Das, S. 2008, Science, 320, 909
- Ryu, D., Kang, H., Hallman, E., & Jones, T. W. 2003, ApJ, 593, 599
- Salvador-Sole, E., Solanes, J. M., & Manrique, A. 1998, ApJ, 499, 542
- Sarazin, C. L. 1988, X-ray emission from clusters of galaxies (Cambridge Astrophysics Series, Cambridge: Cambridge University Press, 1988)
- . 1999, ApJ, 520, 529
- Sarazin, C. L. 2002a, in ASSL, Vol. 272, Merging Processes in Galaxy Clusters, ed. L. Ferretti, I. M. Gioia, & G. Giovannini, 1–38
- Sarazin, C. L. 2002b, in Astrophysics and Space Science Library, Vol. 272, Merging Processes in Galaxy Clusters, ed. L. Ferretti, I. M. Gioia, & G. Giovannini, 1–38
- Schlickeiser, R. 1989, ApJ, 336, 243

- Schmidt, W., Federrath, C., Hupp, M., Kern, S., & Niemeyer, J. C. 2008, ArXiv e-prints
- Schoenmakers, A. P., de Bruyn, A. G., Röttgering, H. J. A., & van der Laan, H. 2001, *A&A*, 374, 861
- Schuecker, P., Finoguenov, A., Miniati, F., Böhringer, H., & Briel, U. G. 2004, *A&A*, 426, 387
- Skilling, J. 1975, *MNRAS*, 172, 557
- Skillman, S. W., O'Shea, B. W., Hallman, E. J., Burns, J. O., & Norman, M. L. 2008, *ApJ*, 689, 1063
- Smith, R. J., Hudson, M. J., Nelan, J. E., et al. 2004, *AJ*, 128, 1558
- Spergel, D. N., Bean, R., Doré, O., et al. 2007, *ApJS*, 170, 377
- Tittley, E. R. & Henriksen, M. 2003, in *Bulletin of the American Astronomical Society*, Vol. 35, *Bulletin of the American Astronomical Society*, 618–+
- Totani, T. & Kitayama, T. 2000, *ApJ*, 545, 572
- Turner, E. L. & Gott, III, J. R. 1976, *ApJS*, 32, 409
- van Weeren, R. J., Rottgering, H. J. A., Bruggen, M., & Cohen, A. 2009, ArXiv e-prints
- Vikhlinin, A., Markevitch, M., & Murray, S. S. 2001, *ApJ*, 549, L47
- Virtanen, J. J. P. & Vainio, R. 2005, in *American Institute of Physics Conference Series*, Vol. 801, *Astrophysical Sources of High Energy Particles and Radiation*, ed. T. Bulik, B. Rudak, & G. Madejski, 410–411
- Webb, G. M. 1983, *ApJ*, 270, 319
- Woodward, P. & Colella, P. 1984, *Journal of Computational Physics*, 54, 115

Bibliography

.

Acknowledgements

I would like to take this opportunity to express my sincere gratitude towards my advisor Prof. Dr. Karl Mannheim for his cooperative assistance, discussions and encouragement for this thesis work. Discussion with him always have been very fruitful and I gained more insight into astrophysics from them. I am very much thankful to him especially for giving me the opportunity to think and work independently and freely. He wanted to see me as leading a collaborative project which ultimately helped me in successful completion of the thesis and opened a lot of future prospects for my career.

I also wish to thank Dr. Luigi Iapichino for his help throughout the project. He was like my second guide and taught me all about hydrodynamic simulations. I always benefited much discussing with him. He always helped me to focus my view on essential questions. It became much easier to give a proper shape of the project with his active help.

I should now mention about Prof. Dr. Joydeep Bagchi. I am very much thankful to him for his kind help and cooperation for all the aspects of my work. He taught me radio astrophysics and most of the observational techniques. Without his help, my ambition of VLA, NRAO radio observation would not have succeeded. I also thankful to him for inspiring me in taking astrophysics as my scientific career.

I would like to thank Dr. Francesco Miniati for his advice on cosmological simulations and for collaborating with us in this project. I am also thankful to Dr. Torsten Ensslin for his valuable comments on VLA radio observations and on collaborating on that project. Thanks also to Prof. Dr. F. Durret and Dr. G. B. Lima Neto for their help in X-ray data analysis.

Lots of thank to the all other people of Wuerzburg University and mainly to Frau Heyder for their cooperation.

I am also thankful to the Deutschen Forschungsgemeinschaft (DFG) for providing adequate funding for the research and collaboration expenses. I am also thankful to University of Würzburg Graduate Schools (UWGS) for providing me the PhD finishing fellowship (STIBET Abschlußstipendiums). In my work with AIPS and radio data reduction I was benefited from Dr. Chiranjib Konar in Inter University Centre for Astronomy and astrophysics (IUCAA,India).

My special thanks goes to my loving wife Amrita for her continuous encouragement, love and mental support. Thanks to my brother Subhajit for his inspiration, guidance and support throughout my life in taking science as profession. Finally, I am very grateful to my parents for their unconditional support in academic and professional endeavour throughout my life.

Bibliography

.

Curriculum Vitae

Surajit Paul

IUCAA
Pune University Campus
Pune, India 411007

voice +91 (0)20 25604 208
Fax: +91 20 2560 4699
E-mail: surajit@iucaa.ernet.in
or

CONTACT INFORMATION

Lehrstuhl für Astronomie
Universität Würzburg
Am Hubland
D-97074 Würzburg, Germany

Fax:
E-mail: spaul@astro.uni-wuerzburg.de
<http://www.astro.uni-wuerzburg.de/~spaul>

RESEARCH INTERESTS

I am interested in phenomenological study of cosmological structure formation shocks.

Fellowships and Appointments

- Aug, 2009 - Post Doctoral Fellowship at Inter University Centre for Astronomy and Astrophysics(IUCAA), Pune, India.
- Dec, 2005 - July, 2009 Doctoral Fellowship, **Lehrstuhl für Astronomie, Universität Würzburg, Germany**
Jan, 2009 - June, 2009: STIBET AbschlusStipendiums (DAAD).
Dec, 2005 - Dec, 2008: Doctoral Fellowship (Deutschen Forschungsgemeinschaft, DFG),from December 2005 - December 2008.
Dissertation Topic: “Evolution of shocks and turbulence in major galaxy-cluster mergers”. Advisor: Prof. Dr. Karl Mannheim.
- Sep, 2005 - Oct, 2005 TAUVEX Project Fellow, Indian Institute of Astrophysics, IIA , Bangalore, India. Advisor: Prof. Dr. Jayant Murthy.
- July, 2004 - July, 2005 Worked as a Project Assistant, July 2004 - July 2005. Research topic: “Cluster merger shocks, a case study: Abell 3376”. Advisor: Prof. Dr. Joydeep Bagchi.
- May, 2003 - July, 2003 Summer Project Fellow, S.N. Bose National Centre for Basic Sciences , Kolkata, India Summer Project Fellow. Project Topic: “Bending of Light Near weak Gravitational Field”. Advisor: Dr. Biswajit Chakraborty.

EDUCATION

- | | |
|-------------|--|
| 2002 - 2004 | M.Sc., Physics, 2004; Department of Physics,
University of Pune, Pune, India. |
| 1999 - 2002 | B.Sc. (Honours) in physics. RKM college.
University of Calcutta. Calcutta, India. |

HONORS AND AWARDS

- Scholarship for Masters studies in Physics 2002-2003 from Indian Association of Physics Teachers (IAPT).
- Selected in the National Entrance Exam. for Master Degree in Physics, conducted by Pune University, June 2002.
- ‘Best Experimenter Prize’ in June 2002 in C.K.Majumder Memorial Workshop in Physics.
- **Gold Medal in NGPE 2002, conducted by IAPT in June 2002. NGPE: National Graduate Physics Examination (INIDIA).**
- National Scholarship for Higher Secondary Education Based on result of 10th standard (School Final, India).

OTHER ACHIEVEMENTS:

Successful observation with VLA (Very Large Array, NRAO, New Mexico, USA.) : Proposal of 6cm radio observation of Abell 3376 to VLA was accepted with excellent referee report. Observation was finished successfully during May, 2008. Title of the proposed observation: VLA mapping of giant ring like structure around galaxy cluster Abell 3376.

Simulation project using HLRB2 supercomputer, Munich, Germany: I am working as a co-investigator, with Dr. Luigi Iapichino (Principal Investigator) in an simulation project using ENZO hydrodynamical tool. We are using supercomputer HLRB2 of the Leibnitz Computer Center, Munich, Germany.

List of Publications

REFEREED PUBLICATIONS

Joydeep Bagchi, Florence Durret, Gastao B. Lima Neto, Surajit Paul : Giant Ringlike Radio Structures Around Galaxy Cluster Abell 3376. **2006, Science, Vol. 314, pp. 791 - 794.**

Iapichino, L., Niemeyer, J.C., Adamek, J., Paul, S., Scuderi, M.: Modeling of Turbulent Flows Applied to Numerical Simulations of Galaxy Clusters. 2007, Proceedings of the workshop "High Performance Computing in Science and Engineering", Springer-verlag. ISBN 978-3-540-69181-5 (Print) 978-3-540-69182-2 (Online).

Iapichino, L., Niemeyer, J., Paul, S., Schmidt, W. Turbulence Modeling and the Physics of the Intra-Cluster Medium. (Accepted for publication in Proceedings of the workshop "High Performance Computing in Science and Engineering", Springer-verlag.)

SUBMITTED PAPERS

S. Paul, L. Iapichino, F. Miniati, J. Bagchi and K. Mannheim : Evolution of shocks and turbulence in major cluster mergers. (Paper submitted to Astrophysical Journal (ApJ))

Tuhin Subhra Konar & Surajit Paul : Integration of e^{x^n} and e^{-x^n} in forms of series, their applications in the field of differential equation ; introducing generalized form of Skewness and Kurtosis; extension of starling's approximation.

<http://aps.arxiv.org/abs/0803.2736>

PAPERS IN PREPARATION

S. Paul, J. Bagchi, L. Iapichino, T. Ensslin, and K. Mannheim : Probing turbulence re-acceleration at the arcs of Abell 3376. (Paper in preparation)

CONFERENCE PROCEEDINGS

Joydeep Bagchi, Florence Durret, Gastao B. Lima Neto, Surajit Paul , Satyajit Chavan: High and ultra-high energy cosmic ray acceleration in structure-formation shocks in Abell 3376 galaxy cluster. 2005, ICRC (International Cosmic Ray Conference) proceedings.

<http://icrc2005.tifr.res.in/htm/Vol-Web/Vol-13/13241-ind-bagchi-J-abs1-og14-poster.pdf>

Joydeep Bagchi, Florence Durret, Gastao B. Lima Neto and Surajit Paul : The disturbed X-ray cluster Abell 3376 and its giant ring-like radio structures. (Accepted for the conference "The X-ray Universe 2008" May 2008, Granada, Spain)

http://xmm.esac.esa.int/external/xmm_science/workshops/2008symposium/xru2008-abstractbook_v1.4.pdf

Bibliography

UNPUBLISHED WORK

Masters Thesis: Setting up a 21 cm Hydrogen Line Radio Telescope and Receiver/Spectrometer.

http://www.astro.uni-wuerzburg.de/~spaul/MSc_thesis.pdf

Report of GK1147/1 workshop:“ Mini-Workshop on Lorentz Violation”.

http://www.astro.uni-wuerzburg.de/~spaul/RTG_LorentzViolation.pdf

